REPORT DOCUMENTATION PAGE

Form Approved OMB No. 0704-0188

1. REPORT DATE *(DD-MM-YYYY)*	2. REPORT TYPE	3. DATES COVERED *(From – To)*
27-01-2004	Final Report	01-Mar-01 - 01-Jul-03

4. TITLE AND SUBTITLE

Aerodynamic Applications of Boundary Layer Control Using Embedded Streamwise Vortices

5a. CONTRACT NUMBER
STCU Registration No: P-053

5b. GRANT NUMBER

5c. PROGRAM ELEMENT NUMBER

6. AUTHOR(S)

Dr. Nina F Yurchenko

5d. PROJECT NUMBER

5d. TASK NUMBER

5e. WORK UNIT NUMBER

7. PERFORMING ORGANIZATION NAME(S) AND ADDRESS(ES)
Institue of Hydromechanics, National Academy of Sciences
8/4 Zheliabov St.
Kiev 04057
Ukraine

8. PERFORMING ORGANIZATION REPORT NUMBER

N/A

9. SPONSORING/MONITORING AGENCY NAME(S) AND ADDRESS(ES)

EOARD
PSC 802 BOX 14
FPO 09499-0014

10. SPONSOR/MONITOR'S ACRONYM(S)

11. SPONSOR/MONITOR'S REPORT NUMBER(S)
STCU 01-8002

12. DISTRIBUTION/AVAILABILITY STATEMENT

Approved for public release; distribution is unlimited.

13. SUPPLEMENTARY NOTES

14. ABSTRACT

The objective of the proposed work is to show feasibility and effectiveness of inherent streamwise vortices to control characteristics of boundary layers through modification of their space-time scales as well as to develop an engineering approach to generation and maintenance of a favorable vortical structure near a wall. To account for flow conditions taking place in practice, the formulated flow control strategy will be extended to fully developed turbulent boundary layers. The investigations were carried out experimentally in wind tunnels and numerically and were focused on structural peculiarities of a near-wall flow and their connection with integral flow characteristics. Special attention was paid to modifications of the turbulence scale/spectra, dissipation rate of turbulence energy, influence on Reynolds shear stress and estimation/measurements of skin friction coefficients. Computational results were verified by measured values of integral boundary-layer characteristics for various cases of flow control.

15. SUBJECT TERMS
EOARD, Physics, Fluid Mechanics

16. SECURITY CLASSIFICATION OF:			17. LIMITATION OF ABSTRACT	18, NUMBER OF PAGES	19a. NAME OF RESPONSIBLE PERSON
a. REPORT	b. ABSTRACT	c. THIS PAGE			WAYNE A. DONALDSON
UNCLAS	UNCLAS	UNCLAS	UL		19b. TELEPHONE NUMBER *(Include area code)* +44 (0)20 7514 4299

Aerodynamic Applications of Boundary Layer Control Using Embedded Streamwise Vortices

***Project manager**:* Yurchenko Nina, Ph.D., Senior Research Associate

Phone: 38 044 459-6512, Fax: 38 044 455-6432,
E-mail: nina.yurchenko@mbox.com.ua

***Institution**:* Institute of Hydromechanics, NASU

***Financing party**:* U.S.A./EOARD

***Operative commencement date**:* 01.03.2001

***Project duration**:* 2 years

***Date of submission**:* 20.11.2002

1. PROJECT LOCATION AND FACILITIES

(1) Institute of Hydromechanics, National Academy of Sciences of Ukraine:
8/4 Zheliabov St., 03057 Kiev, Ukraine;
Phone: (380 44) 446-4313,
Fax: (380 44) 455-6432,
E-mail: vgr@ihm.kiev.ua
http://www.ukrsudo.kiev.ua/gb/hydromech.htm

IHM provides the laboratory and offices as the basic location for the work on the project. Department of Thermal and Fluid Mechanic Modeling and Department of Hydrobionics and Boundary-Layer Control are involved in the work. The laboratory has a wind tunnel (WT 1) which can operate both in an open and closed type regimes: 0.2 m x 0.5 m x 3.0 m test section, 0.02% free-stream turbulence level, free-stream velocity up to 18 m/s; the strain gauge can be used for aerodynamic force measurements.

(2) National Aviation University:
Department of Aircraft Aerodynamics and Flight Security
1, Cosmonaut Komarov Prosp.
Phone: (38 044) 484-9467, 488-4118
Fax: (38 044) 488-3027
E-mail: post@nau-edu.kiyv.ua
http://www.nau-edu.kyiv.ua

NAU provides the wind tunnel (WT 2) for measurements, design & construction shops for fabrication of the test models and experiment rigging. WT 2 is of a closed-type with an oval 0.42 m x 0.7 m x 1.5 m test section, free-stream velocity up to 28 m/s; equipped with the 3-component strain gauge (values of streamwise and normal forces measured up to 3N and 6 N correspondingly, measurement error of no more than 1.5%). For future investigations, the big wind tunnel can be used together with a proper 3-dimensional model: test section of 4m x 2.5m x 5.5m, free-stream velocities up to 42 m/s, multi-base 6-component strain gauge.

Project Manager: Nina F. Yurchenko, Ph.D., Senior Research Associate, IHM, NASU.

2. PERSONNEL RESPONSIBILITIES AND COMMITMENTS

1) Dr. N. Yurchenko, project manager:

- Formulation of the problem based on earlier investigations, organization of the research team and distribution of tasks: (1) Institute of Hydromechanics, National Academy of Sciences, Department of Thermal and Fluid Mechanic Modeling and Department of Boundary Layer Control, (2) National Aviation University.
- Estimation of geometrical and thermal-control parameters of the test models proceeding from the Goertler theory and previous experience obtained for transitional boundary layers over concave surfaces as well as from preliminary data on turbulent boundary layers over flat plates with generated streamwise vortices (recommendations were made for curvature radii, scales of generated vortices, temperature regimes).
- Development of the measurements strategy and working plans, their correction in a course of the project implementation; initiation of direct surface temperature measurements using a remote temperature sensor.
- Coordination of experimental and numerical tasks: choice of compatible boundary and initial conditions (flow and control parameters) from the viewpoint of physics, joint analysis of the obtained results.

- Processing and analysis of skin friction coefficients found numerically for the case of transitional boundary layers over concave surfaces with thermally generated streamwise vortices of different types and scales; Evaluation of long-term effects of the thermal control method.
- Planned and emergency provision of necessary experimental and office equipment, involvement of additional specialists following the program needs and de-facto situation with the problem solution and available resources;
- Preparation of the quarterly reports and papers. Participation in national and international conferences. Organization of brain-storming discussions to explain contradictory results at first stages of measurements and computations.

2) Prof. G. Voropaev, leader of the numerical group:

- Detailed elaboration of the working program to match its numerical and experimental parts.
- Formation and leadership of the numerical group, distribution of separate computational tasks, joint discussions with experimentalists, planning of next research steps for the most productive outcome. Involvement of additional personnel on a temporary basis according to the work requirements.
- Asymptotic analysis of flow values expansions by the inverse Reynolds number to estimate the effect of small deterministic disturbances. The results validated the choice of the flow control approach using streamwise heated elements in a turbulent boundary layer. The problem was formulated for numerical solution of 3D near-wall turbulent flow of nonisothermal viscous compressible fluid based on the 3D Reynolds stress transport model. Further computations were supposed to determine integral effects of vortical structures.
- Analysis of calculated skin friction coefficients for transitional boundary layers over a concave wall with thermal generation of streamwise vortices (together with N. Yurchenko). These results obtained under conditions mimicking the flow around the airfoil test model helped to formulate the numerical program for the turbulent case as well as to improve the experimental program.
- Development of the numerical algorithm *as a final software product* for simulation of a 3D vortical structure in a turbulent boundary layer under conditions of the applied method of thermal flow control based on full Navier-Stokes equations. Development of a model for numerical simulation of a 3D near-wall turbulent flow. Organization of computations based on this model to get values of normal stress and two shear stress components; it enabled to compare the numerical and experimental results.
- Application of the developed turbulence model to numerical simulation of a 3D vortical structure in turbulent boundary layers over concave and convex surfaces provided that the thermal flow control can be switched on at a given moment.
- Analysis of interim results, flexible adjustment of the numerical simulation to the progress and key issues of experiments. Interpretation of disagreements between results obtained in 2 experimental and in the numerical group. Involvement of the support personnel for data processing.

3) Dr. V. Korobov, IHM:

- Planning of experiments in the IHM Wind Tunnel, WT 1, (design drawings of the airfoil model, adjustment of the 3-component strain gauge, choice of visualization methods).
- Elaboration of the overall measurement program in coordination with the NAU experimental team.
- Preparation of experiments in the IHM Wind Tunnel, WT 1, (preliminary tests and processing of data from the 3-component strain gauge). Assembling and tests of the measurement system that included units for registration of aerodynamic forces, pressure fluctuations and free-stream velocity together with the data acquisition and processing.
- Aerodynamic tests of the airfoil model R800 in the WT 1. Measurement of integral flow characteristics, drag $C_x(\alpha)$ and lift $C_y(\alpha)$ coefficients.
- Estimations of effects related to the boundary layer thermal control based on measured $C_y(\alpha)$ and $C_x(\alpha)$ coefficients of the R800 model depending on the free-stream velocity, angle of attack α, temperature distribution over the model. Preliminary tests of liquid crystal visualization method.

4) Dr. R. Pavlovsky, leader of the NAU experimental group:

- Management of the NAU team including the NAU Subcontract on design and fabrication of test models. Development of the fabrication technology as well of the support-operation systems suitable for the both wind tunnels (in close collaboration with N.Yurchenko and V.Korobov); subsequent provision of the NAU team and shops with necessary materials and instrumentation: temporary involvement of necessary specialists for more efficient and prospective work on the project (e.g. for calculations of geometry and aerodynamic quality of airfoil models);
- Design and fabrication of the airfoil models taking into account the design and flow requirements related to their use in the both Wind Tunnels with specific rigging and measurement tools.
- Technological design of the models (substantiation for choice of materials, processing and assembling together with flush-mounted pressure probes).
- Fabrication and adjustments of 2 basic and 2 subsidiary test models. Reference measurements of aerodynamic characteristics in WT 2. Measurement of the basic flow parameters of the WT 2, measurement and calculation of free-stream turbulence level, preparation of the facility for the planned cycle of flow-control measurements.
- Participation in measurements of lift, drag and momentum carried out in WT 2. Coordination with the parallel experiments in WT 1, IHM.

5) Dr. P. Vinogradsky, NAU:

- Scrupulous analysis and further modernization of available NAU measurement systems to investigate dynamic integral flow characteristics (lift and drag).
- Estimation of expected aerodynamic loading on the test models; design of a test unit consisting of a strain gauge assembled together with the airfoil models.
- Purchase and installation in WT 2 of the hardware for precise and effective measurements of model angles of attack and for processing of the obtained data.
- Mounting of a strain gauge and electric drive of the angle-of-attack setting mechanism in WT-2; estimation of accuracy of controlled values; software development for data acquisition and processing.
- Software development for data acquisition and processing in WT 2.
- Strain gauge tests in the assembled facility-measurement system together with the developed software for the data acquisition and processing in WT 2.
- Repeatedly made error estimations and calibration of the measurement systems in WT-2 as well as the developed software for the data acquisition and processing in WT 2.
- Responsible for the experimental data acquisition and processing with required accuracy (permanent error control during the measurements) in WT 2; participation in drag, lift and momentum measurements.

6) Dr. O. Zhdanov, NAU:

- Analysis and choice of visualization methods applicable to the investigated problem; estimation of working parameters of the proposed aerosol-fluorescent visualization system for the WT 2 accounting for the model and flow conditions.
- Analysis and choice of visualization methods applicable to the investigated problem; estimation of working parameters of the proposed aerosol-fluorescent visualization system for the WT 2 accounting for the model and flow conditions
- Visualization system is fabricated and tested in WT2; it is based on aerosol dispersion in an air flow. Nozzle characteristics are chosen for given experimental parameters, the data having been presented in a form of a table and graphs
- Choice of substances and concentrations for flow visualization in WT2 using the developed droplet method
- Estimation of aerosol visualization system parameters Choice of substances and concentrations for flow visualization in WT2 using the developed droplet method

- Participation in drag, lift and momentum measurements in WT 2; new attempts to get acceptable resolution for near-wall flow visualization using different methods (aerosol spray, surface oil film, liquid crystal).

8) N. Rozumnyuk, IHM post-graduate student:

- Survey of published experimental and theoretical papers on coherent structures in a near-wall region of transitional and turbulent thermal boundary layers. An emphasis was made to classification by vortex typical scales, lifetime, and influence on integral dynamic characteristics. Performed analysis and conclusions assisted both to choose a model and define peculiar computational details related to the problem of a flow control using streamwise vortices initiated due to the thermal boundary condition.
- Calculation of skin friction coefficients for a pre-turbulent boundary layer over a surface with the thermal control.
- Computational work: numerical simulation of a 3D flow fields over convex and concave surfaces subject to the thermal flow control. Realization of the developed (Voropaev) numerical algorithm to calculate velocity and pressure variables.
- Analysis of results obtained in a form of normal and spanwise velocity profiles, normal and tangential forces.

9) V. Tsymbal, IHM engineer:

- Preparations of the laboratory (Thermal and Fluid Dynamic Modeling Department) and the WT 1 to the cycle of planned measurements: revision of available equipment and purchase of necessary parts, and instruments; replacement of separate parts and details of the experimental facility.
- Adjustment of electrical circuits and organization of measurement places including the development of the model/measurement systems rigging. Assistance in installation of a security system in a working room, arrangement of functional working places in the lab and office.
- Reference runs of the wind tunnel to check its basic parameters, tests of canonical bodies in the WT 1. Processing of measured results related to experiments on two airfoil test models.
- Mounting and adjustment of the airfoil models and measurement devices in the test section (together with Korobov and separately); setting up of the heating system and flow temperature control;
- Participation in all measurements of integral flow characteristics (drag and lift) as well as in the data processing; re-mounting and adjustments of the experimental model in the wind tunnel test section according to varied flow and thermal control parameters.

10) T. Gradoboeva, IHM secretary:

Secretarial work.

3. PROBLEM FORMULATION: BACKGROUND, APPROACH AND METHODS

The objective of the proposed work is to show feasibility and effectiveness of streamwise vortices inherent to flows under body forces to control characteristics of boundary layers through modification of their space-time scales as well as to develop an engineering approach to generation and maintenance of a favorable vortical structure near a wall.

3.1. Introduction

Optimal boundary-layer control remains both fundamental and applied fluid dynamic problem for scientists and designers of advanced aerospace vehicles and turbomachinery, in particular, dealing with the performance and operation of gas-turbine-engine blades, vanes or airfoils [107,108].

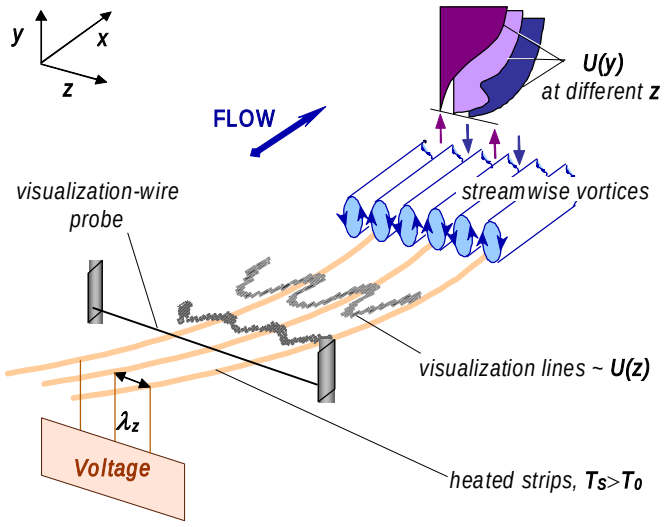

Fig. 3.1.1. Sketch of the flow field illustrating the problem

It is known that practically exploited fluid systems contain large-scale vortical structures that drastically change fluid transport and mixing properties. For instance, flows affected by body forces, i.e. those accounting for the surface geometry or a body-flow temperature difference, reveal a tendency to self-organization of large-scale counter-rotating streamwise vortices. A physical mechanism driving the vortex dynamics of such flows was shown to consist in balanced interaction in boundary layers between forces of body and viscous nature [73]. When vorticity intensities of these two sources become comparable at a certain downstream position of a laminar-turbulent developing boundary layer, it gives rise to longitudinal vortices.

Therefore it is expedient to investigate the feasibility of this inherent flow structural element to control integral characteristics of boundary layers [107,108,103,104,105,106]. Previous numerical and experimental studies yielded an insight into natural and forced evolution of a vortical structure in transitional boundary layers over concave surfaces [108,103, 105].

Boundary-layer flows over concave surfaces in a process of their laminar-turbulent transition are a classical case of flows with naturally developing streamwise vortices. They were extensively studied in a framework of the Goertler stability theory and receptivity approach [35,78,84, 103, 105] and therefore can serve as the prototype for further studies aimed at the vortex dynamics control. Numerous computational, experimental and analytical investigations proved that vortex formation and evolution play a dominant role in producing and sustaining turbulence [5,12,13,61,71,88,87], i.e. processes practically significant for engineering applications. Besides, Goertler vortices were also observed in experimental investigations of a turbulent boundary layer over a concave wall reported by Tani [84].

Therefore for the insight completeness and effective applications, turbulent flows with embedded regular vortices are to be considered.

Widely used engineering models of turbulent transfer give statistical information about the turbulent flow structure. However in case of available large-scale vortices, i.e. with significant turbulence anisotropy, conventional methods of turbulence modeling fail. Exploration of the extent to which turbulence models can mimic the form and the effects of large-scale vortices on the turbulent flow is given in [88,87,3,30, 27, 60,4560]. In spectral terms, contribution of large-scale vortices to the long-wave “energy-carrying” part of the turbulent kinetic energy spectrum plays a main role in fluid transport near a wall. Therefore it is important to study mechanisms of turbulent kinetic-energy redistribution between a long-wave region and the inertial interval of turbulent fluctuations.

In the turbulent environment, the inflectional velocity profiles related to the inviscid Goertler instability result in highly unsteady vortex patterns. The controlled boundary-layer situation supposes spanwise nonuniformities in a flow which provide a more regular vortical pattern. Both experimentally and numerically, it can be realized through the boundary condition in a form of the surface temperature variation periodic in a spanwise direction (See Fig. 3.1.1); the previous experience showed that it can be practically realized using regularly spaced streamwise heated elements flush-mounted in the wall. Calculating or measuring forces/momentums affecting the model, one can conclude about the advantages of the streamwise vortices embedded in a boundary layer and about a method convenience to control integral characteristics.

Thus the present project offers, first of all, a new flow control strategy based on the

flow control similarity principle: optimal management of boundary layer characteristics due to the support of an inherent to flow vortical structure with space scales and intensity modified so that to match basic flow parameters and a boundary-layer control objective.

The application of this principle must require minimum energy outlay and may result in the development of new engineering methods aimed, e.g. to manipulate separation or laminar-turbulent transition of boundary layers, to enhance heat transfer, etc.

3.2. Overview of available data on the vortex dynamics of turbulent boundary layers

Analysis of published and earlier obtained results on physical mechanisms driving the vortex dynamics of laminar-turbulent transition under body forces and its control is presented in reports "DEVELOPMENT OF BOUNDARY LAYER CONTROL TECHNIQUES EFFICIENT FOR FLOWS UNDER BODY FORCES" (Contract F61775-98-WE123) and "OPTIMAL FLOW CONTROL BASED ON EXCITATION OF INHERENT COHERENT VORTICES: FUNDAMENTAL BACKGROUND" (Contract F61775-99-WE075). The present task represents the logical extension of the thermal control approach (applied initially to the regime of a laminar-turbulent transition) to the fully developed turbulent flow. Therefore it requires a detailed review of turbulent vortex dynamics and its correlation with an expected flow control outcome.

A developed turbulent boundary layer is relatively thick having a thin near-wall region with high velocity gradients and a thicker outer region with low gradients. Both regions are characterized with their typical scales of fluid motion. Under the Kolmogoroff's hypothesis, one can neglect correlation between small- and large-scale disturbances at sufficiently high Reynolds numbers. Thus different scale disturbances are assumed to be statistically independent. Small-scale disturbances are isotropic, and large-scale disturbances being determined by typical gradients of mean flow quantities are anisotropic. However they are connected energetically and topologically: large vortices are known to elongate and break down into smaller vortices.
Large random vortical structures in the outer region generate large vortices downstream thus resulting in an abrupt growth of a boundary layer thickness and, accordingly, in the increased friction drag. In this connection, the boundary-layer control aimed, for instance, at drag reduction should be based on such modification of vortex scales that to prevent appearance of large vortices or/and to delay their breakdown. The same purpose of turbulent drag reduction in the near-wall region requires to maintain vortex scales so that not to permit vortices to break up to viscous scales that would increase energy dissipation.
This conditional division of motion scales and mechanisms allows to confine a range of phenomena under consideration and to study evolution of specified vortical structures and their influence onto integral flow characteristics.

The formulated problem of a turbulent flow control stipulated that the survey of published experimental and theoretical data has been focused on coherent structures in a near-wall region of transitional and turbulent boundary layers. Vortical structures in turbulent boundary layers (TBL) were classified by their typical scales, lifetime, and influence on integral flow characteristics [21, 22, 34, 36, 38, 39, 100].

Organized vortical structures are found against the statistically uniform background of random pressure and velocity fluctuations both in the near-wall and outer regions of boundary layers [14, 25, 32, 49, 50, 53, 59]. These structures interact, exchange energy and determine resultant pulsation of velocity and pressure, temperature and mass inside the boundary layer and in the vicinity of the surface [3, 7, 27, 35, 42, 44, 47, 51, 54, 101].
The near-wall region of turbulent boundary layers studied in [14, 49, 53] displayed small-scale low-speed coherent structures, called streaks. These structures are related to counter-rotating streamwise vortices [7, 35, 56]. The authors [3, 27, 42, 44] consider the streaks as "legs" of counter-rotating hairpin or saddle-shaped vortices. Being generated in the near-wall region, these vortices rise from the wall, start oscillating with

growing amplitude and finally break down bursting low-speed fluid [12, 47, 51, 101]. Typical streamwise scales of these structures are $\lambda_x^+ \approx 1000$ [14, 15, 23, 75] and their spanwise scales are about $\lambda^+_Z \approx 100$ [7, 45, 49, 53, 75]. Their convective velocity is (0,2-0,5)U_∞ [28, 45] and time interval between bursts $-T_B u_\tau^2 / \nu \approx 100$ [15, 60, 92, 97, 101].

Boundary layers studied over the whole thickness [19, 32, 59] displayed available organized motion in their logarithmic and outer regions [16, 82, 101] with much larger scales compared to the mentioned above near-wall structures. Large-scale coherent structures named bulges or horseshoe vortices were found to arise from the breakdown of the near-wall small-scale structures and their merging into large vortical conglomerations which extend from $y^+ \approx 250$ [30] to outer layers of TBL. Their streamwise scale can reach 2δ [19, 23, 32, 75], a spanwise scale is of the order of (0,5-1)δ and a spacing between the centers is (2-3)δ at $y=0.8\delta$ [23, 30, 82]. These structures move with the convective velocity $U_c \approx (0,8\text{-}0,9)U_\infty$ [19, 30, 82, 101].

Flow geometry and thermodynamic parameters essentially influence the structure of transitional and turbulent boundary layers. The effects depend on the inhomogeneity scale. Large-scale geometric inhomogeneities ($L_{geom}>\delta$) are considered as "curvature", and small ones ($L_{geom}<\delta$) are referred to the "roughness". Convex longitudinal curvature leads to elongation and stabilization of vortical structures in the near-wall region, and significant effects (up to 20% drag reduction) can be found even for large enough radii of curvature [22, 38]. All three components of normal Reynolds stress decrease that means invariable level of anisotropy; the same happens with the Reynolds shear stress $-\overline{uv}$ which can even become positive in the outer region of the boundary layer [1, 9, 70].
Concave longitudinal curvature tends to create quasi-stable longitudinal vortices in the TBL outer region that distorts a typical turbulence pattern [21, 70] increasing intensity of turbulent stresses.
Effects of both sign curvature can be seen up to 100δ downstream [20, 22, 70].

Boundary layer control is used to reduce drag, increase flight elevation, manipulate heat- and mass transfer, delay/prevent flow separation, control aerodynamic noise. From the viewpoint of vortex dynamics, it ties together a fluid motion structure and scales with integral flow characteristics. From the viewpoint of energy outlay, boundary layer control methods can be passive and active, the latter requiring an additional power source.

In [54], effects of changeable wall temperature on forced disturbances were analyzed along with nonlinear stability of transitional boundary layer ($Re=10^5$, $Pr=6.3$). Optimal width of spanwise heated elements was related to the Tollmin-Schlihting wavelength. It was shown that, at specific wall heating law, the growth rate of Tollmin-Schlihting waves could be decreased downstream up to the disturbance damping at certain regimes. To influence small disturbances (~0.05%U_∞), temperature variation of 2-3°C was sufficient. This value had to reach 10-15°C to control more intense disturbances. There was also shown an essential difference in the development and control of 2D- and 3D-disturbances. Homogeneous wall heating [55] can decrease the intensity of disturbances, as well. Local friction drag was shown to be lower where the wall temperature was lower.

Favorable pressure gradient causes certain elongation of the near-wall longitudinal vortices, their stabilization and weakens bursting. Intensity of normal and shear stresses decreases, especially in the viscous sublayer and buffer zones, at $y^+<50$ [71, 92]. Under relatively high values of favorable pressure gradient, the flow is laminarized, but available residual fluctuations lead to fast development of turbulence after the pressure (as a control factor) is removed [80, 103].
Unfavorable pressure gradient increases bursting frequency and fluctuating pressure/velocity amplitudes. The Reynolds stresses differ noticeably in the outer region of TBL with a second maximum appearing there [80, 92].

Roughness affects mainly the near-wall turbulence [18, 57]. Passage of vortical structures provokes local bursts and intensifies energy exchange between the near-wall and outer regions of TBL [41]. Mean velocity profile is less full on a rough surface than that on a smooth one (up to 20%, at $y/\delta \sim 0.1$) [57, 58].
Small-scale longitudinal riblets create strong crosswise viscous forces that sweep turbulence away from the wall and weaken its intensity [83, 87, 93]. Streamwise vortices elongate and stabilize; spacing between them grows followed by a slight decrease of a bursting frequency. Inside riblet valleys, fluid is almost immovable due to the strong damping effect of crosswise viscous forces [5, 40, 94].

To destroy vortices, basically those of a large scale, honeycombs, screens, and large-eddy breakup devices (LEBU) are used. Honeycombs and screens destroy vortices across entire boundary layer. Skin friction can be reduced to 20% however additional drag because of applied external devices diminishes total drag reduction [67, 78]. Application of the LEBU is considered to be high performance in hydrodynamic drag reduction [8, 26, 42, 52]. Tandem of plates mounted at about $0{,}85\delta$ reduces friction drag reduction up to 20% [1,10,64,95]. Along with that, the boundary-layer thickness grows slower, bursting intensity decreases, turbulence intensity is suppressed. Friction drag reduction can be registered at a distance of $100\text{-}150\delta$ downstream from the LEBU location [1, 10, 52].

Application of soluble polymer additives and substances like surfactants and fibers can be referred to techniques with the highest performance of hydrodynamic drag reduction [11, 64, 68, 73]. In polymer solutions, the turbulence intensity decreases due to deformation of the polymer molecules. It generates local anisotropy of fluid viscosity that weakens local spanwise energy exchange. As shown in [76], while any-scale vortical streaks are deformed in flows of Newtonian fluids, elongation of small streaks is weaker in polymer solution flows. The mean velocity profile is fuller and its linear region is thicker, the highest effect of polymer additives having been found within $10<y^+<100$ [63, 96]. Maximum in a normal distribution of fluctuating longitudinal velocity moves from the location at $y^+\approx 15$ in water to $y^+\approx 30$ in polymer solution flow. Energy redistribution in power spectrum of pressure fluctuations occurs from high- to low-frequency range. Polymer additives strongly suppress normal velocity fluctuations in the whole frequency range and across the boundary layer thickness, their maximum shifts to $y^+=150\div 200$. Power spectrum width for water is about four times of that for polymer solutions [96]. Normalized shear stresses in the outer region of TBL are the same for both flows but in polymer solutions, a maximum is farther away of the wall. The Reynolds stresses decrease, and even negative values were reported in [11, 84, 96].

Thus coherent (in particular, streamwise) vortices were found to be one of the intrinsic features of turbulent boundary layers that justifies the application of the *flow similarity principle* to control these vortical structures and, consequently, TBL integral characteristics.
The effective flow control, i.e. one yielding a favorable outcome with minimal energy/costs outlay, is expected under a purposeful modification of space-time scales of the inherent to flow vortical motion. From the exploitation viewpoint, it should provide flexibility, i.e. possibilities to adjust control parameters to varying flow and/or operation requirements, simple and reliable design, performance and long-term exploitation characteristics. The thermal-control technique satisfies these requirements. A spanwise-periodic temperature gradient, $\Delta T(z)$, stimulates the generation of preferred-scale streamwise vortices. Due to the division of the whole control surface onto sections, easy temperature (applied voltage) regulation and a possibility to change a scale of induced vortical structure during the operation makes the proposed method versatile, simple and reliable in exploitation.

According to the Work Program, the investigations were carried out numerically and experimentally in transitional and turbulent boundary layers with controllably embedded large-scale vortices. The control factor was introduced as a boundary condition in a form of a periodic variation of $\Delta T(z)$ where both its z-scale and intensity could be varied in the matched manner for the most efficient analysis of computational and measurement results.

4. THEORETICAL/NUMERICAL APPROACH

4.1. Guidance of asymptotic estimates. Theoretical model of a boundary layer to be controlled by the surface properties

Asymptotic analysis based on a small parameter in a form of an inverse Reynolds number has been performed to estimate the influence of small deterministic disturbances on zero- and first-order terms in expansions of flow characteristics. Having used a general model developed and successfully tested earlier for a case of a deformable (visco-elastic) surface, it was shown that its transversal deformation changes the both terms in the expansion unlike the case of a smooth rigid surface. The fact of longitudinal flow structures maintaining the Prandtl's form of a zero-order approximation validates the chosen approach as well as the investigated thermal-control technique to generate streamwise vortices.

To determine integral effects owing to regular large-scale vortical structures, the theoretical work was planned in two parallel directions:

- Skin friction coefficients are to be calculated for the case of a transitional boundary layer in the framework of the Goertler approach for streamwise vortices generated with different scales over a concave surface;
- Numerical simulation of a 3D near-wall turbulent flow of nonisothermal viscous compressible fluid based on the 3D Reynolds stress transport model should provide values of normal stress and two shear stress components, $-\overline{u'v'}$ and $-\overline{u'w'}$.

It was supplemented with the experiments on the two airfoil models tested under different angles of attack to match with computations in terms of values of aerodynamic loading and a location of flow separation depending on scales and intensity of generated regular vortices.

4.2. Theoretical model of near-wall flows at varying boundary conditions

Local properties of turbulence in a near-wall region are determined by the upstream flow prehistory and by boundary conditions on a wall (impermeability, non-slip, local deformations, heating/cooling, blowing/suction). If these conditions do not destroy the boundary layer, then, at a stochastic flow regime, the downstream influence of the boundary inhomogeneities is limited by 5-10 values of a boundary layer thickness and their effect can be considered as local. Generation of certain vortical structures in a TBL can extend their influence much farther downstream which is determined by the scale and lifetime of these structures. Distributed (opposite to localized) type of disturbances induced by the wall, e.g. like surface deformation or temperature variation, will cause local characteristics of the balanced gradient flow to depend on the wall parameters.

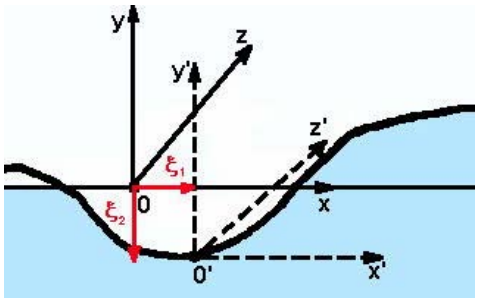

Fig. 4.2.1. The coordinate system (x,y,z) is associated with a neutral surface.

Let us consider two coordinate systems. The origin of a stable system (x, y, z) lays on a neutral surface and the second, moving system (x', y', z'), is associated with a deformable surface as shown in Fig. 4.2.1. In this case:

$$t = t';$$

$$x = x' + \xi_1(x,t);$$

$$y = y' + \xi_2(x,t);$$

$$z = z' + \xi_3(x,t).$$

i.e., coordinates of a point in the fixed system (x,y,z) may be expressed through nonstationary coordinate (x',y',z',t'). Then the moving system can be expressed in terms of stable

coordinates:

$$x' = x - \xi_1(x,z,t);$$
$$y' = y - \xi_2(x,z,t);$$
$$z' = z - \xi_3(x,z,t);$$
$$t' = t.$$

The moving coordinate system is shifted by oscillations about a neutral surface, so that the velocity components will be:

$$U_i = U_i' + \frac{\partial \xi_i}{\partial t};$$

where U_i' are velocity components in the moving coordinate system.

Introduce the change of variables:

$$\frac{\partial}{\partial x} = \frac{\partial}{\partial x'}\frac{\partial x'}{\partial x} + \frac{\partial}{\partial y'}\frac{\partial y'}{\partial x} + \frac{\partial}{\partial z'}\frac{\partial z'}{\partial x} + \frac{\partial}{\partial t'}\frac{\partial t'}{\partial x} = \frac{\partial}{\partial x'}\left(1 - \frac{\partial \xi_1}{\partial x}\right) + \frac{\partial}{\partial y'}\left(-\frac{\partial \xi_2}{\partial x}\right) + \frac{\partial}{\partial z'}\left(-\frac{\partial \xi_3}{\partial x}\right);$$

$$\frac{\partial}{\partial y} = \frac{\partial}{\partial x'}\frac{\partial x'}{\partial y} + \frac{\partial}{\partial y'}\frac{\partial y'}{\partial y} + \frac{\partial}{\partial z'}\frac{\partial z'}{\partial y} + \frac{\partial}{\partial t'}\frac{\partial t'}{\partial y} = \frac{\partial}{\partial y'};$$

$$\frac{\partial}{\partial z} = \frac{\partial}{\partial x'}\frac{\partial x'}{\partial z} + \frac{\partial}{\partial y'}\frac{\partial y'}{\partial z} + \frac{\partial}{\partial z'}\frac{\partial z'}{\partial z} + \frac{\partial}{\partial t'}\frac{\partial t'}{\partial z} = \frac{\partial}{\partial x'}\left(-\frac{\partial \xi_1}{\partial z}\right) + \frac{\partial}{\partial y'}\left(-\frac{\partial \xi_2}{\partial z}\right) + \frac{\partial}{\partial z'}\left(-\frac{\partial \xi_3}{\partial z}\right);$$

$$\frac{\partial}{\partial t} = \frac{\partial}{\partial x'}\frac{\partial x'}{\partial t} + \frac{\partial}{\partial y'}\frac{\partial y'}{\partial t} + \frac{\partial}{\partial z'}\frac{\partial z'}{\partial t} + \frac{\partial}{\partial t'}\frac{\partial t'}{\partial t} = \frac{\partial}{\partial x'}\left(-\frac{\partial \xi_1}{\partial t}\right) + \frac{\partial}{\partial y'}\left(-\frac{\partial \xi_2}{\partial t}\right) + \frac{\partial}{\partial z'}\left(-\frac{\partial \xi_3}{\partial t}\right) + \frac{\partial}{\partial t'};$$

$$\frac{\partial^2}{\partial x^2} = \frac{\partial^2}{\partial x'^2}\left(1 - \frac{\partial \xi_1}{\partial x}\right)^2 + \frac{\partial^2}{\partial y'^2}\left(-\frac{\partial \xi_2}{\partial x}\right)^2 + \frac{\partial^2}{\partial z'^2}\left(-\frac{\partial \xi_3}{\partial x}\right)^2 + 2\frac{\partial^2}{\partial x'\partial y'}\left(1 - \frac{\partial \xi_1}{\partial x}\right)\left(-\frac{\partial \xi_2}{\partial x}\right)$$
$$+ 2\frac{\partial^2}{\partial x'\partial z'}\left(1 - \frac{\partial \xi_1}{\partial x}\right)\left(-\frac{\partial \xi_3}{\partial x}\right) + 2\frac{\partial^2}{\partial y'\partial z'}\left(-\frac{\partial \xi_2}{\partial x}\right)\left(-\frac{\partial \xi_3}{\partial x}\right) + \frac{\partial}{\partial x'}\left(-\frac{\partial^2 \xi_1}{\partial x^2}\right) + \frac{\partial}{\partial y'}\left(-\frac{\partial^2 \xi_2}{\partial x^2}\right) + \frac{\partial}{\partial z'}\left(-\frac{\partial^2 \xi_3}{\partial x^2}\right);$$

$$\frac{\partial^2}{\partial z^2} = \frac{\partial^2}{\partial x'^2}\left(-\frac{\partial \xi_1}{\partial z}\right)^2 + \frac{\partial^2}{\partial y'^2}\left(-\frac{\partial \xi_2}{\partial z}\right)^2 + \frac{\partial^2}{\partial z'^2}\left(1 - \frac{\partial \xi_3}{\partial z}\right)^2 + 2\frac{\partial^2}{\partial y'\partial z'}\left(-\frac{\partial \xi_2}{\partial z}\right)\left(1 - \frac{\partial \xi_3}{\partial z}\right)$$
$$+ \frac{\partial}{\partial x'}\left(-\frac{\partial^2 \xi_1}{\partial z^2}\right) + \frac{\partial}{\partial y'}\left(-\frac{\partial^2 \xi_2}{\partial z^2}\right) + \frac{\partial}{\partial z'}\left(-\frac{\partial^2 \xi_3}{\partial z^2}\right);$$

$$\frac{\partial^2}{\partial y^2} = \frac{\partial^2}{\partial y'^2}.$$

The Navier-Stokes equations in the new coordinates are as follows.
For U-component:

$$\frac{\partial U'}{\partial t'} + \left[\frac{\partial^2 \xi_1}{\partial t^2} + \frac{\partial \xi_1}{\partial t}\frac{\partial^2 \xi_1}{\partial x \partial t} + \frac{\partial \xi_3}{\partial t}\frac{\partial^2 \xi_1}{\partial z \partial t}\right] + U'\frac{\partial U'}{\partial x'} + V'\frac{\partial U'}{\partial y'} + W'\frac{\partial U'}{\partial z'}$$
$$+ \left(U' + \frac{\partial \xi_1}{\partial t}\right)\left[\frac{\partial U'}{\partial x'}\left(-\frac{\partial \xi_1}{\partial x}\right) + \frac{\partial U'}{\partial y'}\left(-\frac{\partial \xi_2}{\partial x}\right) + \frac{\partial U'}{\partial z'}\left(-\frac{\partial \xi_3}{\partial x}\right)\right]$$
$$+ \left(W' + \frac{\partial \xi_3}{\partial t}\right)\left[\frac{\partial U'}{\partial x'}\left(-\frac{\partial \xi_1}{\partial z}\right) + \frac{\partial U'}{\partial y'}\left(-\frac{\partial \xi_2}{\partial z}\right) + \frac{\partial U'}{\partial z'}\left(-\frac{\partial \xi_3}{\partial z}\right)\right]$$
$$+ U'\frac{\partial^2 \xi_1}{\partial t \partial x} + W'\frac{\partial^2 \xi_1}{\partial t \partial z} = -\frac{1}{\rho}\frac{\partial P}{\partial x'} - \frac{1}{\rho}\left[\frac{\partial P}{\partial x'}\left(-\frac{\partial \xi_1}{\partial x}\right) + \frac{\partial P}{\partial y'}\left(-\frac{\partial \xi_2}{\partial x}\right) + \frac{\partial P}{\partial z'}\left(-\frac{\partial \xi_3}{\partial x}\right)\right] \quad (1)$$

$$+\nu\left[\frac{\partial^2 U'}{\partial x'^2}+\frac{\partial^2 U'}{\partial y'^2}+\frac{\partial^2 U'}{\partial z'^2}\right]$$

$$-2\nu\left[\frac{\partial^2 U'}{\partial x'^2}\frac{\partial \xi_1}{\partial x}+\frac{\partial^2 U'}{\partial x'\partial y'}\frac{\partial \xi_2}{\partial x}+\frac{\partial^2 U'}{\partial x'\partial z'}\left(\frac{\partial \xi_3}{\partial x}+\frac{\partial \xi_1}{\partial z}\right)+\frac{\partial^2 U'}{\partial y'\partial z'}\frac{\partial \xi_2}{\partial z}+\frac{\partial^2 U'}{\partial z'^2}\frac{\partial \xi_3}{\partial z}\right]$$

$$+\nu\left\{\frac{\partial^2 U'}{\partial x'^2}\left[\left(\frac{\partial \xi_1}{\partial x}\right)^2+\left(\frac{\partial \xi_1}{\partial z}\right)^2\right]+\frac{\partial^2 U'}{\partial y'^2}\left[\left(\frac{\partial \xi_2}{\partial x}\right)^2+\left(\frac{\partial \xi_2}{\partial z}\right)^2\right]\right\}+\nu\frac{\partial^2 U'}{\partial y'^2}\left[\left(\frac{\partial \xi_3}{\partial x}\right)^2+\left(\frac{\partial \xi_3}{\partial z}\right)^2\right]$$

$$+2\nu\left\{\frac{\partial^2 U'}{\partial x'\partial y'}\left[\frac{\partial \xi_1}{\partial x}\frac{\partial \xi_2}{\partial x}+\frac{\partial \xi_1}{\partial z}\frac{\partial \xi_2}{\partial z}\right]+\frac{\partial^2 U'}{\partial x'\partial z'}\left[\frac{\partial \xi_1}{\partial x}\frac{\partial \xi_3}{\partial x}+\frac{\partial \xi_1}{\partial z}\frac{\partial \xi_3}{\partial z}\right]\right\}$$

$$+2\nu\frac{\partial^2 U'}{\partial y'\partial z'}\left[\frac{\partial \xi_2}{\partial x}\frac{\partial \xi_3}{\partial x}+\frac{\partial \xi_2}{\partial z}\frac{\partial \xi_3}{\partial z}\right]+\nu\left\{2\frac{\partial^2 U'}{\partial y'\partial z'}\left[\frac{\partial \xi_2}{\partial x}\frac{\partial \xi_3}{\partial x}+\frac{\partial \xi_2}{\partial z}\frac{\partial \xi_3}{\partial z}\right]\right\}$$

$$+\nu\left\{\frac{\partial U'}{\partial x'}\left[-\left(\frac{\partial^2 \xi_1}{\partial x^2}+\frac{\partial^2 \xi_1}{\partial z^2}\right)\right]+\frac{\partial U'}{\partial y'}\left[-\left(\frac{\partial^2 \xi_2}{\partial x^2}+\frac{\partial^2 \xi_2}{\partial z^2}\right)\right]+\frac{\partial U'}{\partial z'}\left[-\left(\frac{\partial^2 \xi_3}{\partial x^2}+\frac{\partial^2 \xi_3}{\partial z^2}\right)\right]\right\}$$

$$+\nu\frac{\partial}{\partial t}\left[\frac{\partial^2 \xi_1}{\partial x^2}+\frac{\partial^2 \xi_1}{\partial z^2}\right];$$

For W-component:

$$\frac{\partial W'}{\partial t}+\left[\frac{\partial^2 \xi_3}{\partial t^2}+\frac{\partial \xi_1}{\partial t}\frac{\partial^2 \xi_3}{\partial x\partial t}+\frac{\partial \xi_3}{\partial t}\frac{\partial^2 \xi_3}{\partial z\partial t}\right]+U'\frac{\partial W'}{\partial x'}+V'\frac{\partial W'}{\partial y'}+W'\frac{\partial W'}{\partial z'}$$

$$+\left(U'+\frac{\partial \xi_1}{\partial t}\right)\left[\frac{\partial W'}{\partial x'}\left(-\frac{\partial \xi_1}{\partial x}\right)+\frac{\partial W'}{\partial y'}\left(-\frac{\partial \xi_2}{\partial x}\right)+\frac{\partial W'}{\partial z'}\left(-\frac{\partial \xi_3}{\partial x}\right)\right] \qquad (2)$$

$$+\left(W'+\frac{\partial \xi_3}{\partial t}\right)\left[\frac{\partial W'}{\partial x'}\left(-\frac{\partial \xi_1}{\partial z}\right)+\frac{\partial W'}{\partial y'}\left(-\frac{\partial \xi_2}{\partial z}\right)+\frac{\partial W'}{\partial z'}\left(-\frac{\partial \xi_3}{\partial z}\right)\right]$$

$$+U'\frac{\partial^2 \xi_3}{\partial t\partial x}+W'\frac{\partial^2 \xi_3}{\partial t\partial z}=-\frac{1}{\rho}\frac{\partial P}{\partial z'}-\frac{1}{\rho}\left[\frac{\partial P}{\partial x'}\left(-\frac{\partial \xi_1}{\partial z}\right)+\frac{\partial P}{\partial y'}\left(-\frac{\partial \xi_2}{\partial z}\right)+\frac{\partial P}{\partial z'}\left(-\frac{\partial \xi_3}{\partial z}\right)\right]$$

$$+\nu\left[\frac{\partial^2 W'}{\partial x'^2}+\frac{\partial^2 W'}{\partial y'^2}+\frac{\partial^2 W'}{\partial z'^2}\right]-2\nu\left[\frac{\partial^2 W'}{\partial x'^2}\frac{\partial \xi_1}{\partial x}+\frac{\partial^2 W'}{\partial x'\partial y'}\frac{\partial \xi_2}{\partial x}+\frac{\partial^2 W'}{\partial y\partial z}\frac{\partial \xi_2}{\partial z}\right]-2\nu\left[\frac{\partial^2 W}{\partial x\partial z}\left(\frac{\partial \xi_3}{\partial x}+\frac{\partial \xi_1}{\partial z}\right)+\frac{\partial^2 W'}{\partial z'^2}\frac{\partial \xi_3}{\partial z}\right]$$

$$+\nu\left\{\frac{\partial^2 W'}{\partial x'^2}\left[\left(\frac{\partial \xi_1}{\partial x}\right)^2+\left(\frac{\partial \xi_3}{\partial z}\right)^2\right]+\frac{\partial^2 W'}{\partial y'^2}\left[\left(\frac{\partial \xi_2}{\partial x}\right)^2+\left(\frac{\partial \xi_2}{\partial z}\right)^2\right]\right\}+\nu\frac{\partial^2 W'}{\partial z'^2}\left[\left(\frac{\partial \xi_3}{\partial x}\right)^2+\left(\frac{\partial \xi_3}{\partial z}\right)^2\right]$$

$$+\nu\left\{\frac{\partial^2 W'}{\partial x'^2}\left[\left(\frac{\partial \xi_1}{\partial x}\right)^2+\left(\frac{\partial \xi_3}{\partial z}\right)^2\right]+\frac{\partial^2 W'}{\partial y'^2}\left[\left(\frac{\partial \xi_2}{\partial x}\right)^2+\left(\frac{\partial \xi_2}{\partial z}\right)^2\right]\right\}$$

$$+\nu\frac{\partial^2 W'}{\partial z'^2}\left[\left(\frac{\partial \xi_3}{\partial x}\right)^2+\left(\frac{\partial \xi_3}{\partial z}\right)^2\right]$$

$$+\nu\left\{\frac{\partial^2 W'}{\partial x'\partial y'}\left[\frac{\partial \xi_1}{\partial x}\frac{\partial \xi_2}{\partial x}+\frac{\partial \xi_1}{\partial z}\frac{\partial \xi_2}{\partial z}\right]+2\frac{\partial^2 W'}{\partial x'\partial z'}\left[\frac{\partial \xi_1}{\partial x}\frac{\partial \xi_3}{\partial x}+\frac{\partial \xi_1}{\partial z}\frac{\partial \xi_3}{\partial z}\right]\right\}$$

$$+\nu\left\{2\frac{\partial^2 W'}{\partial y'\partial z'}\left[\frac{\partial \xi_2}{\partial x}\frac{\partial \xi_3}{\partial x}+\frac{\partial \xi_2}{\partial z}\frac{\partial \xi_3}{\partial z}\right]\right\}$$

$$-\nu\left\{\frac{\partial W'}{\partial x'}\left[\frac{\partial^2\xi_1}{\partial x^2}+\frac{\partial^2\xi_1}{\partial z^2}\right]+\frac{\partial W'}{\partial y'}\left[\frac{\partial^2\xi_2}{\partial x^2}+\frac{\partial^2\xi_2}{\partial z^2}\right]+\frac{\partial W'}{\partial z'}\left[\frac{\partial^2\xi_3}{\partial x^2}+\frac{\partial^2\xi_3}{\partial z^2}\right]\right\}+\nu\frac{\partial}{\partial t}\left[\frac{\partial^2\xi_3}{\partial x^2}+\frac{\partial^2\xi_3}{\partial z^2}\right];$$

For V-component:

$$\begin{aligned}
&\frac{\partial V'}{\partial t'}+\left[\frac{\partial^2\xi_2}{\partial t^2}+\frac{\partial\xi_1}{\partial t}\frac{\partial^2\xi_2}{\partial t\partial x}+\frac{\partial\xi_3}{\partial t}\frac{\partial^2\xi_2}{\partial t\partial z}\right]+U'\frac{\partial V'}{\partial x'}+V'\frac{\partial V'}{\partial y'}+W'\frac{\partial V'}{\partial z'}\\
&-\left(U'+\frac{\partial\xi_1}{\partial t}\right)\left[\frac{\partial V'}{\partial x'}\left(\frac{\partial\xi_1}{\partial x}\right)+\frac{\partial V'}{\partial y'}\left(\frac{\partial\xi_2}{\partial x}\right)+\frac{\partial V'}{\partial z'}\left(\frac{\partial\xi_3}{\partial x}\right)\right]\\
&-\left(W'+\frac{\partial\xi_3}{\partial t}\right)\left[\frac{\partial V'}{\partial x'}\left(\frac{\partial\xi_1}{\partial z}\right)+\frac{\partial V'}{\partial y'}\left(\frac{\partial\xi_2}{\partial z}\right)+\frac{\partial V'}{\partial z'}\left(\frac{\partial\xi_3}{\partial z}\right)\right]+U'\left(\frac{\partial^2\xi_2}{\partial t\partial x}\right)+W'\left(\frac{\partial^2\xi_2}{\partial t\partial z}\right)=\\
&-\frac{1}{\rho}\frac{\partial P}{\partial y'}+\nu\left[\frac{\partial^2 V'}{\partial x'^2}+\frac{\partial^2 V'}{\partial y'^2}+\frac{\partial^2 V'}{\partial z'^2}\right]\\
&-2\nu\left[\frac{\partial^2 V'}{\partial x'^2}\left(\frac{\partial\xi_1}{\partial x}\right)+\frac{\partial^2 V'}{\partial x'\partial y'}\left(\frac{\partial\xi_2}{\partial x}\right)++\frac{\partial^2 V'}{\partial y'\partial z'}\left(\frac{\partial\xi_2}{\partial z}\right)+\frac{\partial^2 V'}{\partial x'\partial z'}\left(\frac{\partial\xi_3}{\partial x}+\frac{\partial\xi_1}{\partial z}\right)\right]\\
&-2\nu\frac{\partial^2 V'}{\partial z'^2}\left(\frac{\partial\xi_3}{\partial z}\right)\\
&+\nu\left\{\frac{\partial^2 V'}{\partial x'^2}\left[\left(\frac{\partial\xi_1}{\partial x}\right)^2+\left(\frac{\partial\xi_3}{\partial z}\right)^2\right]+\frac{\partial^2 V'}{\partial y'^2}\left[\left(\frac{\partial\xi_2}{\partial x}\right)^2+\left(\frac{\partial\xi_2}{\partial z}\right)^2\right]+\frac{\partial^2 V'}{\partial z'^2}\left[\left(\frac{\partial\xi_3}{\partial x}\right)^2+\left(\frac{\partial\xi_3}{\partial z}\right)^2\right]\right\}\\
&+\nu\left\{2\frac{\partial^2 V'}{\partial x'\partial y'}\left[\frac{\partial\xi_1}{\partial x}\frac{\partial\xi_2}{\partial x}+\frac{\partial\xi_1}{\partial z}\frac{\partial\xi_2}{\partial z}\right]+2\frac{\partial^2 V'}{\partial x'\partial z'}\left[\frac{\partial\xi_1}{\partial x}\frac{\partial\xi_3}{\partial x}+\frac{\partial\xi_1}{\partial z}\frac{\partial\xi_3}{\partial z}\right]\right\}\\
&+\left\{2\frac{\partial^2 V'}{\partial y'\partial z'}\left[\frac{\partial\xi_2}{\partial x}\frac{\partial\xi_3}{\partial x}+\frac{\partial\xi_2}{\partial z}\frac{\partial\xi_3}{\partial z}\right]\right\}\\
&-\nu\left\{\frac{\partial V'}{\partial x'}\left[\frac{\partial^2\xi_1}{\partial x^2}+\frac{\partial^2\xi_1}{\partial z^2}\right]+\frac{\partial V'}{\partial y'}\left[\frac{\partial^2\xi_2}{\partial x^2}+\frac{\partial^2\xi_2}{\partial z^2}\right]+\frac{\partial V'}{\partial z'}\left[\frac{\partial^2\xi_3}{\partial x^2}+\frac{\partial^2\xi_3}{\partial z^2}\right]\right\}+\nu\frac{\partial}{\partial t}\left[\frac{\partial^2\xi_2}{\partial x^2}+\frac{\partial^2\xi_2}{\partial z^2}\right];
\end{aligned}\tag{3}$$

The continuity equation:

$$\begin{aligned}
&\frac{\partial U'}{\partial x'}\left(1-\frac{\partial\xi_1}{\partial x}\right)+\frac{\partial U'}{\partial y'}\left(-\frac{\partial\xi_2}{\partial x}\right)+\frac{\partial U'}{\partial z'}\left(-\frac{\partial\xi_3}{\partial x}\right)+\frac{\partial V'}{\partial y'}+\frac{\partial W'}{\partial x'}\left(-\frac{\partial\xi_1}{\partial z}\right)+\frac{\partial W'}{\partial y'}\left(-\frac{\partial\xi_2}{\partial z}\right)+\frac{\partial W'}{\partial z'}\left(1-\frac{\partial\xi_3}{\partial z}\right)\\
&+\frac{\partial^2\xi_1}{\partial x\partial t}+\frac{\partial^2\xi_3}{\partial z\partial t}=0
\end{aligned}$$

will be given as:

$$\frac{\partial U'}{\partial x'}+\frac{\partial V'}{\partial y'}+\frac{\partial W'}{\partial z'}+M_\xi=0;\tag{4}$$

where

$$M_\xi=-\left[\frac{\partial U'}{\partial x'}\left(\frac{\partial\xi_1}{\partial x}\right)+\frac{\partial U'}{\partial y'}\left(\frac{\partial\xi_2}{\partial x}\right)+\frac{\partial U'}{\partial z'}\left(\frac{\partial\xi_3}{\partial x}\right)+\frac{\partial W'}{\partial x'}\left(\frac{\partial\xi_1}{\partial z}\right)\right]-\left[\frac{\partial W'}{\partial y'}\left(\frac{\partial\xi_2}{\partial z}\right)+\frac{\partial U'}{\partial z'}\left(\frac{\partial\xi_3}{\partial z}\right)\right]+\left(\frac{\partial^2\xi_1}{\partial x\partial t}+\frac{\partial^2\xi_3}{\partial z\partial t}\right),$$

is a source term that characterizes variation of mass in a point.

The surface displacement is given in a form of

$\xi_1 = A_1 e^{i\alpha x - i\omega t + i\theta_1 + i\beta z}$;

$\xi_2 = A_2 e^{i\alpha x - i\omega t + i\theta_2 + i\beta z}$;

$\xi_3 = A_3 e^{i\alpha x - i\omega t + i\theta_3 + i\beta z}$,

that allows to characterize all additional terms in the equations by quantities A_i, α, β, ω.

Consider the near-wall flow region and assume $A_i = \tilde{A}_i \delta \varepsilon^k$ where δ is a boundary layer thickness, $\varepsilon \sim \frac{1}{\sqrt{Re}}$ is a small parameter. Expanding velocity components in a series by the small parameter, we get

$U_i = U_{i0} + \varepsilon U_{i1} + \varepsilon^2 U_{i2} + \ldots$

Here, characteristic scales are as follows:

δ - length scale normally to the surface,
L - streamwise length scale,
S - spanwise length scale,
U_0 - streamwise velocity component,
$V_0 = U_0\delta_0/L$ - normal velocity,
$W_0 = U_0 S/L$ - spanwise velocity,
$\omega_0 = U_0/\delta$ - frequency.

Consider the equations retaining the zero and first-order terms by ε. Assuming that

$$U' = U_0\left[\tilde{U}_0 + \varepsilon\tilde{U}_1 + \varepsilon^2\tilde{U}_2 + \ldots\right];$$

$$V' = \frac{U_0\delta}{L}\left[\tilde{V}_0 + \varepsilon\tilde{V}_1 + \varepsilon^2\tilde{V}_2 + \ldots\right];$$

$$W' = \frac{U_0 s}{L}\left[\tilde{W}_0 + \varepsilon\tilde{W}_1 + \varepsilon^2\tilde{W}_2 + \ldots\right]$$

and considering wavy deformations with a wavelength of the order of the boundary layer thickness $\lambda_x \sim \lambda_z \sim 1/\delta$, $\left(\tilde{\alpha} = \alpha\delta, \tilde{\beta} = \beta\delta, \tilde{\omega} = \omega\frac{U_0}{\delta}\right)$ where $\alpha = \frac{2\pi}{\lambda_x}, \beta = \frac{2\pi}{\lambda_z}$, we can derive equations of a zero-order approximation.

$$\frac{\partial\tilde{U}_0}{\partial\tilde{x}} + \frac{\partial\tilde{V}_0}{\partial\tilde{y}} + \frac{\partial\tilde{W}_0}{\partial\tilde{z}} + \varepsilon\left(\frac{\partial\tilde{U}_1}{\partial\tilde{x}} + \frac{\partial\tilde{V}_1}{\partial\tilde{y}} + \frac{\partial\tilde{W}_1}{\partial\tilde{z}}\right)$$
$$+ \varepsilon^k\left[\frac{\partial\tilde{U}_0}{\partial\tilde{x}}\left(i\tilde{A}_1\tilde{\alpha}\right) + \frac{L}{\delta}\frac{\partial\tilde{U}_0}{\partial\tilde{y}}\left(i\tilde{A}_2\tilde{\alpha}\right) + \frac{L}{s}\frac{\partial\tilde{U}_0}{\partial\tilde{z}}\left(i\tilde{A}_3\tilde{\alpha}\right)\right]$$
$$+ \varepsilon^k\left[\frac{s}{L}\frac{\partial\tilde{W}_0}{\partial\tilde{x}}\left(i\tilde{A}_1\tilde{\beta}\right) + \frac{s}{\delta}\frac{\partial\tilde{W}_0}{\partial\tilde{y}}\left(i\tilde{A}_2\tilde{\beta}\right) + \frac{\partial\tilde{W}_0}{\partial\tilde{z}}\left(i\tilde{A}_3\tilde{\beta}\right)\right]$$
$$+ \left(\tilde{A}_1\tilde{\alpha}\tilde{\omega}\right)\frac{L}{\delta}\varepsilon^k + \left(\tilde{A}_3\tilde{\beta}\tilde{\omega}\right)\frac{L}{\delta}\varepsilon^k = 0;$$

If typical scales S and L are of the same order, $\delta/L \sim \varepsilon$, and the surface deforms with a frequency corresponding to the energy-carrying frequency of the boundary layer, then the zero-order approximation of the continuity equation at k=1 takes a form of

$$\frac{\partial\tilde{U}_0}{\partial\tilde{x}} + \frac{\partial\tilde{V}_0}{\partial\tilde{y}} + \frac{\partial\tilde{W}_0}{\partial\tilde{z}} - \frac{\partial\tilde{U}_0}{\partial\tilde{y}}\frac{\partial\xi_2}{\partial x} - \frac{\partial\tilde{W}_0}{\partial\tilde{y}}\frac{\partial\xi_2}{\partial z} + \frac{\partial}{\partial t}\left[\frac{\partial\xi_1}{\partial x} + \frac{\partial\xi_3}{\partial z}\right] = 0.$$

Under available typical vortex scales of an order of a boundary layer thickness (S~δ, $\delta/L \sim \varepsilon$), the zero-order continuity equation is:

$$\frac{\partial \tilde{U}_0}{\partial \tilde{x}}+\frac{\partial \tilde{V}_0}{\partial \tilde{y}}+\frac{\partial \tilde{W}_0}{\partial \tilde{z}}-\left[\frac{\partial \tilde{U}_0}{\partial \tilde{y}}\frac{\partial \xi_2}{\partial x}+\frac{\partial \tilde{U}_0}{\partial \tilde{z}}\frac{\partial \xi_3}{\partial x}\right]+\frac{\partial}{\partial t}\left[\frac{\partial \xi_1}{\partial x}+\frac{\partial \xi_3}{\partial z}\right]=0.$$

Let us retain only zero-order terms governing the surface deformation in the Navier-Stokes equations:

$$\begin{aligned}
&\frac{\partial U'}{\partial t'}+\frac{\partial^2 \xi_1}{\partial t'^2}+U'\frac{\partial U'}{\partial x'}+V'\frac{\partial U'}{\partial y'}+W'\frac{\partial U'}{\partial z'}\\
&+U'\left[\frac{\partial U'}{\partial x'}\left(-\frac{\partial \xi_1}{\partial x}\right)+\frac{\partial U'}{\partial y'}\left(-\frac{\partial \xi_2}{\partial x}\right)+\frac{\partial U'}{\partial z'}\left(-\frac{\partial \xi_3}{\partial x}\right)\right]+U'\frac{\partial^2 \xi_1}{\partial t\partial x}\\
&+W'\left[\frac{\partial U'}{\partial x'}\left(-\frac{\partial \xi_1}{\partial z}\right)+\frac{\partial U'}{\partial y'}\left(-\frac{\partial \xi_2}{\partial z}\right)+\frac{\partial U'}{\partial z'}\left(-\frac{\partial \xi_3}{\partial z}\right)\right]+W'\frac{\partial^2 \xi_1}{\partial t\partial z}\\
&=-\frac{1}{\rho}\frac{\partial P}{\partial x'}-\frac{1}{\rho}\left[\frac{\partial P}{\partial x'}\left(-\frac{\partial \xi_1}{\partial x}\right)+\frac{\partial P}{\partial y'}\left(-\frac{\partial \xi_2}{\partial x}\right)+\frac{\partial P}{\partial z'}\left(-\frac{\partial \xi_3}{\partial x}\right)\right]+\nu\left[\frac{\partial^2 U'}{\partial x'^2}+\frac{\partial^2 U'}{\partial y'^2}+\frac{\partial^2 U'}{\partial z'^2}\right]\\
&-2\nu\left[\frac{\partial^2 U'}{\partial x'^2}\left(\frac{\partial \xi_1}{\partial x}\right)+\frac{\partial^2 U'}{\partial x'\partial y'}\left(\frac{\partial \xi_2}{\partial x}\right)++\frac{\partial^2 U'}{\partial x'\partial z'}\left(\frac{\partial \xi_3}{\partial x}+\frac{\partial \xi_1}{\partial z}\right)+\frac{\partial^2 U'}{\partial y'\partial z'}\left(\frac{\partial \xi_2}{\partial z}\right)+\frac{\partial^2 U'}{\partial z'^2}\left(\frac{\partial \xi_3}{\partial z}\right)\right]\\
&-\nu\left[\frac{\partial U'}{\partial x'}\left(\frac{\partial^2 \xi_1}{\partial x^2}+\frac{\partial^2 \xi_1}{\partial z^2}\right)+\frac{\partial U'}{\partial y'}\left(\frac{\partial^2 \xi_2}{\partial x^2}+\frac{\partial^2 \xi_2}{\partial z^2}\right)+\frac{\partial U'}{\partial z'}\left(\frac{\partial^2 \xi_3}{\partial x^2}+\frac{\partial^2 \xi_3}{\partial z^2}\right)\right]+\nu\frac{\partial}{\partial t}\left[\frac{\partial^2 \xi_1}{\partial x^2}+\frac{\partial^2 \xi_1}{\partial z^2}\right]
\end{aligned}$$

At $S \approx L$, $\delta/L \approx \varepsilon$, $\varepsilon \approx 1/\sqrt{Re}$, and surface deformations following a bursting frequency in a viscous sublayer, the U-equation with retained ε^k –order terms (k>0) is

$$\begin{aligned}
&\frac{\partial \tilde{U}_0}{\partial \tilde{t}}+\tilde{U}_0\frac{\partial \tilde{U}_0}{\partial \tilde{x}}+\tilde{V}_0\frac{\partial \tilde{U}_0}{\partial \tilde{y}}+\tilde{W}_0\frac{\partial \tilde{W}_0}{\partial \tilde{z}}-\left(\tilde{\omega}^2\tilde{A}_1\right)\varepsilon^{k-1}\\
&+\varepsilon^{k-1}\tilde{U}_0\frac{\partial \tilde{U}_0}{\partial \tilde{y}}\left(-\tilde{\alpha}\tilde{A}_2\right)+\varepsilon^{k-1}\left(-\tilde{\beta}\tilde{A}_2\right)\tilde{W}_0\frac{\partial \tilde{U}_0}{\partial \tilde{y}}+\left(\tilde{\omega}\tilde{A}_1\tilde{\alpha}\right)\tilde{U}_0\varepsilon^{k-1}\\
&+\left(\tilde{\omega}\tilde{A}_1\tilde{\beta}\right)\tilde{W}_0\varepsilon^{k-1}+\varepsilon\frac{\partial \tilde{U}_1}{\partial t}+\varepsilon\tilde{U}_1\frac{\partial \tilde{U}_0}{\partial \tilde{x}}+\varepsilon\tilde{U}_0\frac{\partial \tilde{U}_1}{\partial \tilde{x}}\\
&+\varepsilon\tilde{V}_1\frac{\partial \tilde{U}_0}{\partial \tilde{y}}+\varepsilon\tilde{V}_0\frac{\partial \tilde{U}_1}{\partial \tilde{y}}+\varepsilon\tilde{W}_1\frac{\partial \tilde{U}_0}{\partial \tilde{z}}+\varepsilon\tilde{W}_0\frac{\partial \tilde{U}_1}{\partial \tilde{z}}\\
&\tilde{U}_0\frac{\partial \tilde{U}_0}{\partial \tilde{x}}\left(-\tilde{\alpha}\tilde{A}_1\right)\varepsilon^k+\tilde{W}_0\frac{\partial U_0}{\partial \tilde{z}}\left(-\tilde{\beta}\tilde{A}_3\right)\varepsilon^k\\
&+\varepsilon^k\left(-\tilde{\alpha}\tilde{A}_2\right)\left[\tilde{U}_1\frac{\partial \tilde{U}_0}{\partial \tilde{y}}+\tilde{U}_0\frac{\partial \tilde{U}_1}{\partial \tilde{y}}\right]+\varepsilon^k\left(-\tilde{\beta}\tilde{A}_2\right)\left[\tilde{W}_1\frac{\partial \tilde{U}_0}{\partial \tilde{y}}+\tilde{W}_0\frac{\partial \tilde{U}_1}{\partial \tilde{y}}\right]\\
&+\varepsilon^k\left(-\tilde{\alpha}\tilde{A}_3\right)\left[\tilde{U}_0\frac{\partial \tilde{U}_0}{\partial \tilde{z}}\right]+\varepsilon^k\left(-\tilde{\beta}\tilde{A}_1\right)\left[\tilde{W}_0\frac{\partial \tilde{U}_0}{\partial \tilde{x}}\right]+\varepsilon^k\tilde{U}_1\left(\tilde{\alpha}\tilde{A}_1\right)+\varepsilon^k\tilde{W}_1\left(\tilde{\beta}\tilde{A}_1\right)\\
&=-\frac{\partial \tilde{P}_0}{\partial \tilde{x}}+\frac{\partial \tilde{P}_0}{\partial \tilde{y}}\varepsilon^k\left(\tilde{\alpha}\tilde{A}_2\right)+\frac{\partial^2 U_0}{\partial \tilde{y}^2}-\varepsilon\frac{\partial \tilde{P}_1}{\partial \tilde{x}}+\frac{\partial \tilde{P}_0}{\partial \tilde{z}}\varepsilon^k\left(\tilde{\alpha}\tilde{A}_3\right)+\frac{\partial \tilde{P}_0}{\partial \tilde{x}}\varepsilon^k\left(\tilde{\alpha}\tilde{A}_1\right)+\frac{\partial \tilde{P}_1}{\partial \tilde{y}}\varepsilon^k\left(\tilde{\alpha}\tilde{A}_2\right)+\varepsilon\frac{\partial^2 U_1}{\partial \tilde{y}^2}\\
&-\frac{\partial \tilde{U}_0}{\partial \tilde{y}}\left(\tilde{\alpha}^2+\tilde{\beta}^2\right)\tilde{A}_2\varepsilon^k+\tilde{\omega}\left(\tilde{\alpha}^2+\tilde{\beta}^2\right)\varepsilon^k\tilde{A}_1+O\left(\varepsilon^{1+k}\right).
\end{aligned}$$

If k>1; $\varepsilon = \frac{\delta}{L}; \omega_0 \approx \frac{U_0}{\delta}; \alpha \approx \frac{1}{\delta}$, i.e. an amplitude of the surface deformation is less than 0.1δ, influence of the deformated surface onto the flow structure can be neglected.

If k=1, the zero-order approximation is:

$$\frac{\partial \tilde{U}_0}{\partial \tilde{t}} + \tilde{U}_0 \frac{\partial \tilde{U}_0}{\partial \tilde{x}} + \tilde{V}_0 \frac{\partial \tilde{U}_0}{\partial \tilde{y}} + \tilde{W}_0 \frac{\partial \tilde{U}_0}{\partial \tilde{z}}$$
$$+ \frac{\partial^2 \xi_1}{\partial t^2} - \tilde{U}_0 \frac{\partial \tilde{U}_0}{\partial \tilde{y}} \frac{\partial \xi_2}{\partial x} - \tilde{W}_0 \frac{\partial \tilde{U}_0}{\partial \tilde{y}} \frac{\partial \xi_2}{\partial z} + \tilde{U}_0 \frac{\partial^2 \xi_1}{\partial x \partial t} + \tilde{W}_0 \frac{\partial^2 \xi_1}{\partial z \partial t}$$
$$= -\frac{\partial \tilde{P}_0}{\partial \tilde{x}} + \frac{\partial \tilde{P}_0}{\partial \tilde{y}} \frac{\partial \xi_2}{\partial x} + \frac{1}{Re} \frac{\partial^2 \tilde{U}_0}{\partial \tilde{y}^2}.$$

When $\alpha \approx \beta \approx \frac{1}{\delta}; \quad A_i \approx \delta \varepsilon^k; \quad \frac{\delta}{L} \approx \frac{s}{L} \approx \varepsilon \approx \frac{1}{\sqrt{Re}}$, i.e. there exist longitudinal structures with typical

spanwise scales of the order of a boundary layer thickness, than U-equation over the deformated surface is:

$$\frac{\partial \tilde{U}_0}{\partial \tilde{t}} + \tilde{U}_0 \frac{\partial \tilde{U}_0}{\partial \tilde{x}} + \tilde{V}_0 \frac{\partial \tilde{U}_0}{\partial \tilde{y}} + \tilde{W}_0 \frac{\partial \tilde{W}_0}{\partial \tilde{z}} - \left(\tilde{\omega}^2 \tilde{A}_1\right) \varepsilon^k \frac{L}{\delta}$$
$$+ \varepsilon^{k-1} \tilde{U}_0 \frac{\partial \tilde{U}_0}{\partial \tilde{y}} \left(-\tilde{\alpha} \tilde{A}_2\right) + \left(\tilde{\omega} \tilde{A}_1 \tilde{\alpha}\right) \tilde{U}_0 \varepsilon^{k-1}$$
$$+ \varepsilon^{k-1} \left(-\tilde{\alpha} \tilde{A}_3\right) \tilde{U}_0 \frac{\partial \tilde{U}_0}{\partial \tilde{z}} + \varepsilon \frac{\partial \tilde{U}_1}{\partial t} + \varepsilon \tilde{U}_1 \frac{\partial \tilde{U}_0}{\partial \tilde{x}} + \varepsilon \tilde{U}_0 \frac{\partial \tilde{U}_1}{\partial \tilde{x}}$$
$$+ \varepsilon \tilde{V}_1 \frac{\partial \tilde{U}_0}{\partial \tilde{y}} + \varepsilon \tilde{V}_0 \frac{\partial \tilde{U}_1}{\partial \tilde{y}} + \varepsilon \tilde{W}_1 \frac{\partial \tilde{U}_0}{\partial \tilde{z}} + \varepsilon \tilde{W}_0 \frac{\partial \tilde{U}_1}{\partial \tilde{z}}$$
$$\tilde{U}_0 \frac{\partial \tilde{U}_0}{\partial \tilde{x}} \left(-\tilde{\alpha} \tilde{A}_1\right) \varepsilon^k + \tilde{W}_0 \frac{\partial \tilde{U}_0}{\partial \tilde{y}} \left(-\tilde{\beta} \tilde{A}_3\right) \varepsilon^k + \left(\tilde{\omega} \tilde{A}_1 \tilde{\beta}\right) \tilde{W}_0 \varepsilon^k$$
$$+ \varepsilon^k \left(-\tilde{\alpha} \tilde{A}_2\right) \left[\tilde{U}_1 \frac{\partial \tilde{U}_0}{\partial \tilde{y}} + \tilde{U}_0 \frac{\partial \tilde{U}_1}{\partial \tilde{y}}\right] + \varepsilon^k \tilde{U}_1 \left(\tilde{\alpha} \tilde{A}_1\right)$$
$$= -\frac{\partial \tilde{P}_0}{\partial \tilde{x}} + \frac{\partial \tilde{P}_0}{\partial \tilde{y}} \varepsilon^{k-1} \left(\tilde{\alpha} \tilde{A}_2\right) + \frac{\partial \tilde{P}_0}{\partial \tilde{z}} \varepsilon^{k-1} \left(\tilde{\alpha} \tilde{A}_3\right) + \frac{\partial^2 U_0}{\partial \tilde{y}^2} + \frac{\partial^2 U_0}{\partial \tilde{z}^2}$$
$$- \varepsilon \frac{\partial \tilde{P}_1}{\partial x} + \frac{\partial \tilde{P}_0}{\partial x} \varepsilon^k \left(\tilde{\alpha} \tilde{A}_1\right) + \frac{\partial \tilde{P}_1}{\partial y} \varepsilon^k \left(\tilde{\alpha} \tilde{A}_2\right) + \frac{\partial \tilde{P}_1}{\partial z} \varepsilon^k \left(\tilde{\alpha} \tilde{A}_3\right) + \varepsilon \frac{\partial^2 \tilde{U}_1}{\partial \tilde{z}^2} + \varepsilon \frac{\partial^2 \tilde{U}_1}{\partial \tilde{y}^2}$$
$$- \frac{\partial \tilde{U}_0}{\partial \tilde{y}} \left(\tilde{\alpha}^2 + \tilde{\beta}^2\right) \tilde{A}_2 \varepsilon^k + \frac{\partial \tilde{U}_0}{\partial \tilde{z}} \left(\tilde{\alpha}^2 + \tilde{\beta}^2\right) \tilde{A}_3 \varepsilon^k + \tilde{\omega} \left(\tilde{\alpha}^2 + \tilde{\beta}^2\right) \varepsilon^k \tilde{A}_1 + O\left(\varepsilon^{k+1}\right).$$

And at k=1, the zero-order approximation is:

$$\frac{\partial \tilde{U}_0}{\partial \tilde{t}} + \tilde{U}_0 \frac{\partial \tilde{U}_0}{\partial \tilde{x}} + \tilde{V}_0 \frac{\partial \tilde{U}_0}{\partial \tilde{y}} + \tilde{W}_0 \frac{\partial \tilde{U}_0}{\partial \tilde{z}}$$
$$+ \frac{\partial^2 \xi_1}{\partial t^2} - \tilde{U}_0 \frac{\partial \tilde{U}_0}{\partial \tilde{y}} \frac{\partial \xi_2}{\partial x} - \tilde{U}_0 \frac{\partial \tilde{U}_0}{\partial \tilde{z}} \frac{\partial \xi_3}{\partial x} + \tilde{U}_0 \frac{\partial^2 \xi_1}{\partial x \partial t}$$
$$= -\frac{\partial \tilde{P}_0}{\partial \tilde{x}} + \frac{\partial \tilde{P}_0}{\partial \tilde{y}} \frac{\partial \xi_2}{\partial x} + \frac{\partial \tilde{P}_0}{\partial \tilde{z}} \frac{\partial \xi_3}{\partial x} + \frac{1}{\mathrm{Re}} \left[\frac{\partial^2 \tilde{U}_0}{\partial \tilde{y}^2} + \frac{\partial^2 \tilde{U}_0}{\partial \tilde{z}^2} \right].$$

The zero-order equations for $\tilde{W}_0$ -component are different for two cases (S~L and S/L~ε). For the first one, it is similar to U_o -equation:

$$\frac{\partial \tilde{W}_0}{\partial t} + \tilde{U}_0 \frac{\partial \tilde{W}_0}{\partial \tilde{x}} + \tilde{V}_0 \frac{\partial \tilde{W}_0}{\partial \tilde{y}} + \tilde{W}_0 \frac{\partial \tilde{W}_0}{\partial \tilde{z}}$$
$$+ \frac{\partial^2 \xi_3}{\partial t^2} + \tilde{U}_0 \frac{\partial \tilde{W}_0}{\partial \tilde{y}} \frac{\partial \xi_2}{\partial x} - \tilde{W}_0 \frac{\partial \tilde{W}_0}{\partial \tilde{y}} \frac{\partial \xi_2}{\partial z} + \tilde{U}_0 \frac{\partial^2 \xi_3}{\partial t \partial x} + \tilde{W}_0 \frac{\partial^2 \xi_3}{\partial t \partial z}$$
$$= -\frac{1}{\rho} \frac{\partial \tilde{P}_0}{\partial \tilde{z}} + \frac{\partial \tilde{P}_0}{\partial \tilde{y}} \frac{\partial \xi_2}{\partial z} + \frac{1}{\mathrm{Re}} \frac{\partial^2 \tilde{W}_0}{\partial y};$$

and for S/L~δ/L~ε, W-equation with ε^2-order terms retained:

$$\varepsilon^2 \frac{\partial \tilde{W}_0}{\partial t} + \varepsilon^k \frac{\partial^2 \xi_3}{\partial t^2} + \varepsilon^2 \left[\tilde{U}_0 \frac{\partial \tilde{W}_0}{\partial \tilde{x}} + \tilde{V}_0 \frac{\partial \tilde{W}_0}{\partial \tilde{y}} + \tilde{W}_0 \frac{\partial \tilde{W}_0}{\partial \tilde{z}} \right]$$
$$- \varepsilon^{k+1} \tilde{U}_0 \frac{\partial \tilde{W}_0}{\partial \tilde{y}} \frac{\partial \xi_2}{\partial x} - \varepsilon^k \tilde{U}_0 \frac{\partial^2 \xi_3}{\partial x \partial t} + \varepsilon^{k+1} \left(\tilde{U}_0 \frac{\partial \tilde{W}_1}{\partial \tilde{y}} + \tilde{U}_1 \frac{\partial \tilde{W}_0}{\partial \tilde{y}} \right) \frac{\partial \xi_2}{\partial x}$$
$$- \varepsilon^{k+1} \tilde{U}_0 \frac{\partial \tilde{W}_0}{\partial \tilde{z}} \frac{\partial \xi_3}{\partial x} + \varepsilon^{k+1} \tilde{U}_1 \frac{\partial^2 \xi_3}{\partial x \partial t} + \varepsilon^{k+1} \tilde{W}_0 \frac{\partial^2 \xi_3}{\partial z \partial t}$$
$$= -\frac{\partial \tilde{P}_0}{\partial \tilde{z}} - \varepsilon \frac{\partial \tilde{P}_1}{\partial \tilde{z}} + \varepsilon^k \left[\frac{\partial \tilde{P}_0}{\partial \tilde{y}} \frac{\partial \xi_2}{\partial z} + \frac{\partial \tilde{P}_0}{\partial \tilde{z}} \frac{\partial \xi_3}{\partial z} \right]$$
$$+ \varepsilon^2 \frac{\partial^2 \tilde{W}_0}{\partial \tilde{y}^2} + \varepsilon^2 \frac{\partial^2 \tilde{W}_0}{\partial \tilde{z}^2} + \varepsilon^{k+1} \frac{\partial}{\partial t} \left[\frac{\partial^2 \xi_3}{\partial x^2} + \frac{\partial^2 \xi_3}{\partial z^2} \right] + O\left(\varepsilon^3\right).$$

V-component equation also differs for these cases, but the difference is not essential. For (S~L):

$$\varepsilon^2 \frac{\partial \tilde{V}_0}{\partial t} + \varepsilon^k \frac{\partial^2 \xi_2}{\partial t^2} + \varepsilon^2 \left[\tilde{U}_0 \frac{\partial \tilde{V}_0}{\partial \tilde{x}} + \tilde{V}_0 \frac{\partial \tilde{V}_0}{\partial \tilde{y}} + \tilde{W}_0 \frac{\partial \tilde{V}_0}{\partial \tilde{z}} \right]$$
$$- \varepsilon^{k+1} \tilde{U}_0 \frac{\partial \tilde{V}_0}{\partial \tilde{y}} \frac{\partial \xi_2}{\partial x} + \varepsilon^k \tilde{U}_0 \frac{\partial^2 \xi_2}{\partial t \partial x} + \varepsilon^{k+1} \tilde{U}_1 \frac{\partial^2 \xi_2}{\partial t \partial x} + \varepsilon^{k+1} \tilde{W}_0 \frac{\partial^2 \xi_2}{\partial t \partial z}$$
$$= -\frac{\partial \tilde{P}_0}{\partial \tilde{y}} - \varepsilon \frac{\partial \tilde{P}_1}{\partial \tilde{y}} + \varepsilon^2 \frac{\partial^2 \tilde{V}_0}{\partial \tilde{y}^2} + \varepsilon^{k+1} \frac{\partial}{\partial t} \left[\frac{\partial^2 \xi_2}{\partial x^2} + \frac{\partial^2 \xi_2}{\partial z^2} \right] + O\left(\varepsilon^3\right),$$

and for S/L~δ/L~ε:

$$\varepsilon^2\frac{\partial\tilde{V}_0}{\partial t}+\varepsilon^k\frac{\partial^2\xi_2}{\partial t^2}+\varepsilon^2\left[\tilde{U}_0\frac{\partial\tilde{V}_0}{\partial\tilde{x}}+\tilde{V}_0\frac{\partial\tilde{V}_0}{\partial\tilde{y}}+\tilde{W}_0\frac{\partial\tilde{V}_0}{\partial\tilde{z}}\right]$$

$$-\varepsilon^{k+1}\left[\tilde{U}_0\frac{\partial\tilde{V}_0}{\partial\tilde{y}}\frac{\partial\xi_2}{\partial x}+\tilde{U}_0\frac{\partial\tilde{V}_0}{\partial\tilde{z}}\frac{\partial\xi_3}{\partial x}\right]+\varepsilon^k\tilde{U}_0\frac{\partial^2\xi_2}{\partial t\partial x}+\varepsilon^{k+1}\tilde{U}_1\frac{\partial^2\xi_2}{\partial t\partial x}+\varepsilon^{k+1}\tilde{W}_0\frac{\partial^2\xi_2}{\partial t\partial z}$$

$$=-\frac{\partial\tilde{P}_0}{\partial\tilde{y}}-\varepsilon\frac{\partial\tilde{P}_1}{\partial\tilde{y}}+\varepsilon^2\left[\frac{\partial^2\tilde{V}_0}{\partial\tilde{y}^2}+\frac{\partial^2\tilde{V}_0}{\partial\tilde{z}^2}\right]+\varepsilon^{k+1}\frac{\partial}{\partial t}\left[\frac{\partial^2\xi_2}{\partial x^2}+\frac{\partial^2\xi_2}{\partial z^2}\right]+O\left(\varepsilon^3\right).$$

Thus we can assume to ε:

$$\frac{\partial\tilde{P}_0}{\partial\tilde{y}}=0;$$

and first-order approximation for normal pressure gradient, at k=1:

$$\frac{\partial\tilde{P}_1}{\partial\tilde{y}}=\frac{\partial^2\xi_2}{\partial t^2}+\tilde{U}_0\frac{\partial^2\xi_2}{\partial x\partial t}+\tilde{W}_0\frac{\partial^2\xi_2}{\partial z\partial t}.$$

At S/L~ε, normal and spanwise pressure gradients for zero- and first-order approximation:

$$\frac{\partial\tilde{P}_0}{\partial\tilde{z}}=0;\frac{\partial\tilde{P}_1}{\partial\tilde{y}}=\frac{\partial^2\xi_2}{\partial t^2}+\tilde{U}_0\frac{\partial^2\xi_2}{\partial x\partial t};\frac{\partial\tilde{P}_1}{\partial\tilde{z}}=\frac{\partial^2\xi_3}{\partial t^2}+\tilde{U}_0\frac{\partial^2\xi_3}{\partial x\partial t}.$$

So, for S~L, the Navier–Stokes equations are reduced to:

$$\frac{\partial\tilde{U}_0}{\partial t}+\tilde{U}_0\frac{\partial\tilde{U}_0}{\partial\tilde{x}}+\tilde{V}_0\frac{\partial\tilde{U}_0}{\partial\tilde{y}}+\tilde{W}_0\frac{\partial\tilde{U}_0}{\partial\tilde{z}}+\frac{\partial^2\xi_1}{\partial t^2}+\tilde{U}_0\frac{\partial^2\xi_1}{\partial x\partial t}+\tilde{W}_0\frac{\partial^2\xi_1}{\partial z\partial t}$$

$$-\tilde{U}_0\frac{\partial\tilde{U}_0}{\partial\tilde{y}}\frac{\partial\xi_2}{\partial x}-\tilde{W}_0\frac{\partial\tilde{U}_0}{\partial\tilde{y}}\frac{\partial\xi_2}{\partial z}=-\frac{\partial\tilde{P}_0}{\partial x}+\frac{1}{Re}\frac{\partial^2\tilde{U}_0}{\partial\tilde{y}^2};$$

$$\frac{\partial\tilde{W}_0}{\partial t}+\tilde{U}_0\frac{\partial\tilde{W}_0}{\partial\tilde{x}}+\tilde{V}_0\frac{\partial\tilde{W}_0}{\partial\tilde{y}}+\tilde{W}_0\frac{\partial\tilde{W}_0}{\partial\tilde{z}}+\frac{\partial^2\xi_3}{\partial t^2}+\tilde{U}_0\frac{\partial^2\xi_3}{\partial x\partial t}+\tilde{W}_0\frac{\partial^2\xi_3}{\partial z\partial t}$$

$$-\tilde{U}_0\frac{\partial\tilde{W}_0}{\partial\tilde{y}}\frac{\partial\xi_2}{\partial x}-\tilde{W}_0\frac{\partial\tilde{W}_0}{\partial\tilde{y}}\frac{\partial\xi_2}{\partial z}=-\frac{\partial\tilde{P}_0}{\partial z}+\frac{1}{Re}\frac{\partial^2\tilde{W}_0}{\partial\tilde{y}^2};$$

$$\frac{\partial\tilde{P}_0}{\partial\tilde{y}}=0;$$

$$\frac{\partial\tilde{U}_0}{\partial\tilde{x}}+\frac{\partial\tilde{V}_0}{\partial\tilde{y}}+\frac{\partial\tilde{W}_0}{\partial\tilde{z}}-\frac{\partial\tilde{U}_0}{\partial\tilde{y}}\frac{\partial\xi_2}{\partial x}-\frac{\partial\tilde{W}_0}{\partial\tilde{y}}\frac{\partial\xi_2}{\partial z}+\frac{\partial}{\partial t}\left[\frac{\partial\xi_1}{\partial x}+\frac{\partial\xi_3}{\partial z}\right]=0.$$

At S/L~ε, the system is more simple:

$$\frac{\partial\tilde{U}_0}{\partial\tilde{t}}+\tilde{U}_0\frac{\partial\tilde{U}_0}{\partial\tilde{x}}+\tilde{V}_0\frac{\partial\tilde{U}_0}{\partial\tilde{y}}+\tilde{W}_0\frac{\partial\tilde{U}_0}{\partial\tilde{z}}$$

$$+\frac{\partial^2\xi_1}{\partial t^2}-\tilde{U}_0\frac{\partial\tilde{U}_0}{\partial\tilde{y}}\frac{\partial\xi_2}{\partial x}-\tilde{U}_0\frac{\partial\tilde{U}_0}{\partial\tilde{z}}\frac{\partial\xi_3}{\partial x}+\tilde{U}_0\frac{\partial^2\xi_1}{\partial x\partial t}=-\frac{\partial\tilde{P}_0}{\partial\tilde{x}}+\frac{1}{Re}\left[\frac{\partial^2\tilde{U}_0}{\partial\tilde{y}^2}+\frac{\partial^2\tilde{U}_0}{\partial\tilde{z}^2}\right];$$

$$\frac{\partial\tilde{P}_0}{\partial y}=0;\frac{\partial\tilde{P}_0}{\partial z}=0;$$

$$\frac{\partial\tilde{U}_0}{\partial\tilde{x}}+\frac{\partial\tilde{V}_0}{\partial\tilde{y}}+\frac{\partial\tilde{W}_0}{\partial\tilde{z}}-\frac{\partial\tilde{U}_0}{\partial\tilde{y}}\frac{\partial\xi_2}{\partial x}-\frac{\partial\tilde{U}_0}{\partial\tilde{z}}\frac{\partial\xi_3}{\partial x}+\frac{\partial}{\partial t}\left[\frac{\partial\xi_1}{\partial x}+\frac{\partial\xi_3}{\partial z}\right]=0.$$

Thus, if the surface properties are regularly structured along x and z, the Navier-Stokes equations are as follows:

for S~L:

$$\tilde{U}_0\frac{\partial\tilde{U}_0}{\partial\tilde{x}}+\tilde{V}_0\frac{\partial\tilde{U}_0}{\partial\tilde{y}}+\tilde{W}_0\frac{\partial\tilde{U}_0}{\partial\tilde{z}}+-\tilde{U}_0\frac{\partial\tilde{U}_0}{\partial\tilde{y}}\frac{\partial\xi_2}{\partial x}-\tilde{W}_0\frac{\partial\tilde{U}_0}{\partial\tilde{y}}\frac{\partial\xi_2}{\partial z}=-\frac{\partial\tilde{P}_0}{\partial x}+\frac{1}{Re}\frac{\partial^2\tilde{U}_0}{\partial\tilde{y}^2};$$

$$\tilde{U}_0\frac{\partial\tilde{W}_0}{\partial\tilde{x}}+\tilde{V}_0\frac{\partial\tilde{W}_0}{\partial\tilde{y}}+\tilde{W}_0\frac{\partial\tilde{W}_0}{\partial\tilde{z}}-\tilde{U}_0\frac{\partial\tilde{W}_0}{\partial\tilde{y}}\frac{\partial\xi_2}{\partial x}-\tilde{W}_0\frac{\partial\tilde{W}_0}{\partial\tilde{y}}\frac{\partial\xi_2}{\partial z}=-\frac{\partial\tilde{P}_0}{\partial z}+\frac{1}{Re}\frac{\partial^2\tilde{W}_0}{\partial\tilde{y}^2};\qquad(*)$$

$$\frac{\partial\tilde{P}_0}{\partial\tilde{y}}=0;$$

$$\frac{\partial\tilde{U}_0}{\partial\tilde{x}}+\frac{\partial\tilde{V}_0}{\partial\tilde{y}}+\frac{\partial\tilde{W}_0}{\partial\tilde{z}}-\frac{\partial\tilde{U}_0}{\partial\tilde{y}}\frac{\partial\xi_2}{\partial x}-\frac{\partial\tilde{W}_0}{\partial\tilde{y}}\frac{\partial\xi_2}{\partial z}=0,$$

for S/L~ε:

$$\tilde{U}_0\frac{\partial\tilde{U}_0}{\partial\tilde{x}}+\tilde{V}_0\frac{\partial\tilde{U}_0}{\partial\tilde{y}}+\tilde{W}_0\frac{\partial\tilde{U}_0}{\partial\tilde{z}}-\tilde{U}_0\frac{\partial\tilde{U}_0}{\partial\tilde{y}}\frac{\partial\xi_2}{\partial x}-\tilde{U}_0\frac{\partial\tilde{U}_0}{\partial\tilde{z}}\frac{\partial\xi_3}{\partial x}=-\frac{\partial\tilde{P}_0}{\partial\tilde{x}}+\frac{1}{Re}\left[\frac{\partial^2\tilde{U}_0}{\partial\tilde{y}^2}+\frac{\partial^2\tilde{U}_0}{\partial\tilde{z}^2}\right];$$

$$\frac{\partial\tilde{P}_0}{\partial y}=0;\quad\frac{\partial\tilde{P}_0}{\partial z}=0;\qquad(**)$$

$$\frac{\partial U_0}{\partial x}+\frac{\partial V_0}{\partial y}+\frac{\partial W_0}{\partial z}-\frac{\partial U_0}{\partial y}\frac{\partial\xi_2}{\partial x}-\frac{\partial U_0}{\partial z}\frac{\partial\xi_3}{\partial x}=0.$$

On the basis of (**), it is easy to show that for a surface with longitudinal riblets (ξ_2=f(z), $\xi_1=\xi_3=0$) the zero-order approximation of Navier-Stokes equations can be reduced to Prandtl equation.

Thus using the Favre's averaging, a system of equations has been derived to describe a flow of nonisothermal viscous compressible fluid. Since free-stream velocities are subsonic, fluid density is assumed not to depend on pressure fluctuations according to the Morkovin's hypothesis. Dissipation is taken isotropic; correlation between velocity and pressure fluctuation derivatives is modeled by Lumly, solenoidal tensor A_{ij} being picked out and the rest of this correlation combined with triple correlations of velocity fluctuations where the gradient diffusion model is applied. The equation system is closed by the model transport equation of a turbulent dissipation rate.

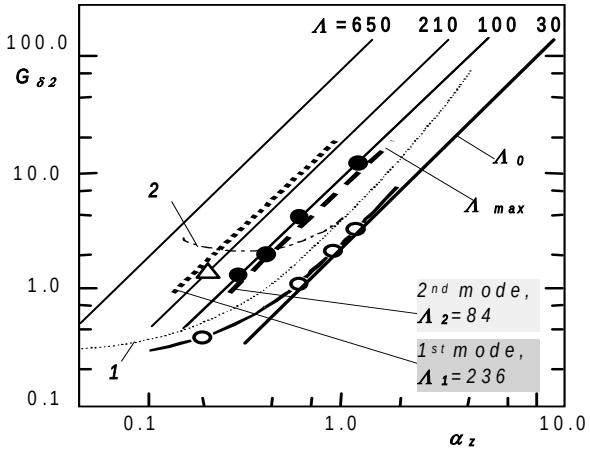

Fig. 5.1.1. Goertler diagram ($G_{\delta 2}=\delta_2^{3/2}U_\infty\nu^{-1}R^{-1/2}$, $\alpha_z=2\pi/\lambda_z$); neutral curves by different authors [78]; $\Lambda_0\approx30$ and $\Lambda_{max}\approx100$ - experimental curves for vortices with zero and maximum growth rates; Λ_1 and Λ_2 – 1st and 2nd modes

5. CHOICE OF BASIC FLOW PARAMETERS, BOUNDARY CONDITIONS FOR COMPUTATIONS AND EXPERIMENTS, TEST MODELS

5.1. Guidance of the Goertler instability approach to match space scales of control vortices with basic flow parameters

Natural laminar-turbulent transition in boundary layers over various surfaces is characterized with the intense chaotic development of eigen modes typical for a certain kind of flows. Numerical and experimental investigations of the transition are based, as a rule, on bringing deterministic features into this process due to setting of specific structure

and scales of the motion under consideration. This approach is much better logically justified in the studied case of a flow under body forces. Both the experimental evidence of a boundary-layer flow developing over a concave wall and numerical simulation based on 3D nonstationary Navier-Stokes equations showed self-organized coherent vortical structures known as Goertler vortices. Their space scales and intensity can be determined depending on the basic flow parameters.

The formulation of the flow control task is specified by the assumption that self-organized vortical structures can be more receptive to the control factor having a commensurable scale. This hypothesis has been checked in the previous experimental and DNS research cycles dealt with laminar-turbulent transition control. Computations and experiments in boundary layers over a concave surface, R_0=0.2m, at the Reynolds number of Re=$5 \cdot 10^5$ showed the best effect on flow characteristics for a spanwise scale of surface temperature variation corresponding to the first Goertler mode (Fig. 5.1.1).

Here, following the general strategy and accounting for the geometry, dimensions and basic flow parameters of available wind tunnels, the Goertler diagram was used as a reference to design test models. As a result, two airfoil-type test models with the thermal control systems were designed and fabricated with equal streamwise curvature along most parts of their concave and convex sides, radii R_1=200 mm and R_2=800 mm, and with the span S=200 mm in both cases. Relative thickness of both models is the same, equal to 0.15. The leading and trailing edges are designed aerodynamically so that the airfoils can be placed in the flow back to front too so that to investigate both classical flow over a surface with constant curvature and typical separation problems arising on turbine blades. It also allows more careful and correct comparative analysis of numerical and experimental results.

The computations have been made for the flow over a curved surface, R_0=0.2m, at the free-stream velocity U_0=10m/s. Following the experimental arrangement where the controlled conditions were realized due to flush-mounted longitudinal elements, these strips were heated numerically to T=328 K° both over concave and convex surfaces of a model. Two values of the distance between heated elements were considered, λ_z=0.0025m and 0.005m, to match with experimental conditions. The first obtained results have shown the clear dependence of developing vortical structures on the thermally controlled z-scale of a forcing factor. However intensity of these vortices was found to be weak for both convex and concave surfaces. Therefore further computations have been carried out for higher values of a free-stream velocity, U_0=15m/s and 20m/s, and the same values of the surface curvature and the control factor.

Vortical motion developing in a boundary layer over a concave surface with a uniform constant temperature was considered as a reference case. For greater flow velocities, it showed the formation of 3D structures with higher intensity. Boundary layer over a convex surface displayed no noticeable vortical structures.

5.2. Design of experiments (DOE) and airfoil test models

The experimental part of the working program consisted of the development of the general measurement strategy for the two wind tunnels WT1 (IHM) and WT2 (NAU), design and fabrication of airfoil models and a flat-plate model with similar thermal control systems, their mounting and operation tests (e.g. under varying angles of attack) as well as the development/adjustment of various measurement, data acquisition and processing systems.

Based on the Goertler approach and available wind tunnel parameters, estimates were made for the design of airfoil test models. They were obtained in a form of reasonable dimensions (120 x 120 mm), relative thickness (C_{max}=0.12), basic radii of the surface curvature (R=200 mm and 800 mm) and a spamwise distance between the streamwise heated elements (λ_z = 2.5 an 5 mm); they served as the given initial conditions to design the aerodynamically correct shape of the models. The airfoil geometry and corresponding pressure distribution along the models were calculated to choose best model profiles to escape early flow separation.

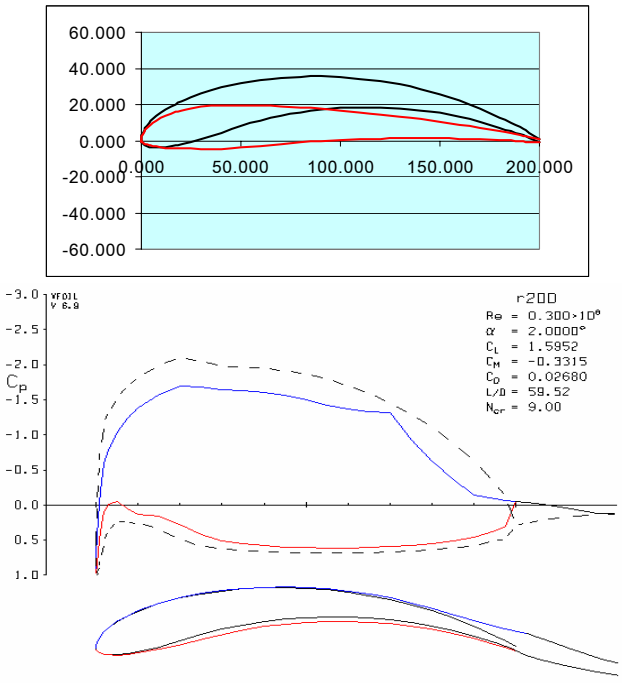

Fig. 5.2.1. Calculated pressure distribution along convex (blue) and concave (red) parts of the airfoil model with the basic curvature radius, R=200 mm

In addition, the design should have taken into account the planned possibility to install and to test the airfoils in wind tunnels at their direct and inverse positions, i.e. making their leading and trailing edges inter-convertible.

These DOE calculations were implemented using the standard XFOIL interactive program for the design and analysis of subsonic isolated airfoils. The general XFOIL methodology is described in "Drela, M., XFOIL: An Analysis and Design System for Low Reynolds Number Airfoils, Conference on Low Reynolds Number Airfoil Aerodynamics, University of Notre Dame, June 1989". The program allows to generate new airfoil geometry based on given parameters (e.g. like the mentioned above value of C_{max}=0.12) as well as to calculate pressure and drag, lift and moment coefficients. Analyzing pressure distributions along a model (similar to one illustrated in Fig. 5.2.1) under different angles of attack, a choice of an advanced geometry could be made that to provide a wider operation range without early flow separation.

In addition to an optimal choice of the model geometry, XFOIL panel method of symmetric singularities (Fig. 5.2.2) was applied to estimate the range of experimental conditions (free-stream velocities, angles of attack) of subsonic isolated airfoils with an infinite span. It allowed to reduce a number of test runs to find out effects of the boundary layer control on lift and drag characteristics of airfoils. These characteristics were calculated for the both R200 and R800 models under their direct and inverse position in the flow (see. Figs. 5.2.2-5.2.12). Preliminary experiments gave values of drag X and lift Y. Aerodynamic coefficients were found from $X = C_x Sq$; $Y = C_y Sq$, where $q = (1/2)\rho U^2$. There was found a significant discrepancy between calculated values of lift coefficients and those obtained from initial measurements in WT 1. After having analyzed possible reasons, experimental and computational approaches were mutually adjusted so that to be identical for the formulated problem.

In this connection, washers were installed in a working section to model a greater airfoil elongation. Using the "PANSYM" software where a method of symmetric peculiarities has been realized, aerodynamic characteristics of airfoil models were calculated taking into account typical flow conditions and real experiment arrangement, in particular, gaps between installation washers and test section walls. The wind tunnel has been modeled with top and bottom screens and with side walls as it is shown in

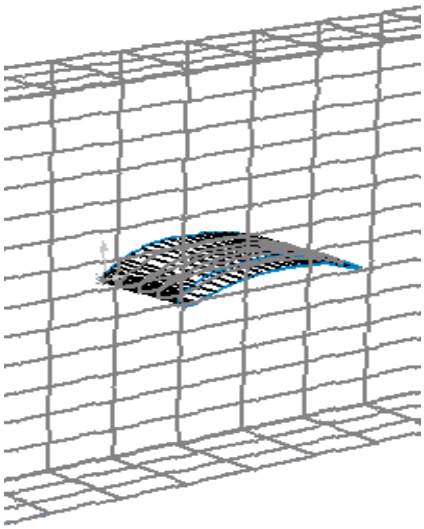

Fig. 5.2.2. Numerical model for calculations of integral flow characteristics around the airfoil

panel presentation of Fig. 5. The calculations were aimed to determine overall and distributed airfoil characteristics.

Thus later obtained numerical and experimental results for the both models (with a profile curvature equal correspondingly to $\bar{f}=f/b\approx5.8\%$ and $\bar{f}\approx15\%$) were found to be in a good agreement. The models were tested at $U_\infty \approx 20$ m/s in a range of angle of attacks $\alpha=-20°\div45°$, the angle of attack having been determined between a flow vector and a tangent to the profile. The model cross-section square was taken as $F=0.1$ m^2.

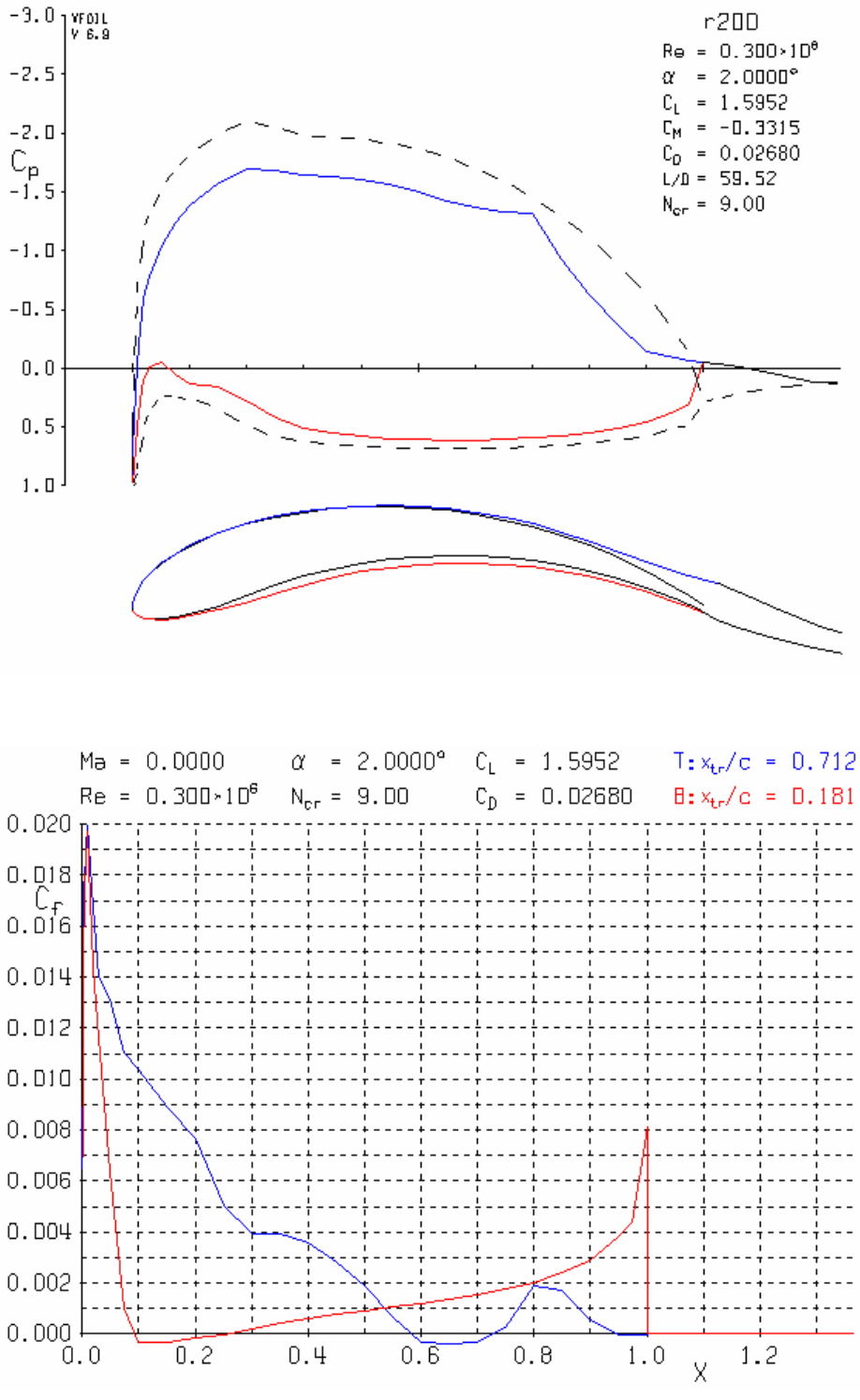
XFOIL
v 6.9
r200
Re = 0.300×10⁶
α = 2.0000°
C_L = 1.5952
C_M = -0.3315
C_D = 0.02680
L/D = 59.52
N_cr = 9.00
C_p
-3.0
-2.5
-2.0
-1.5
-1.0
-0.5
0.0
0.5
1.0
Ma = 0.0000
α = 2.0000°
C_L = 1.5952
T: x_tr/c = 0.712
Re = 0.300×10⁶
N_cr = 9.00
C_D = 0.02680
B: x_tr/c = 0.181
C_f
0.020
0.018
0.016
0.014
0.012
0.010
0.008
0.006
0.004
0.002
0.000
0.0
0.2
0.4
0.6
0.8
1.0
1.2
X

Fig. 5.2.3.

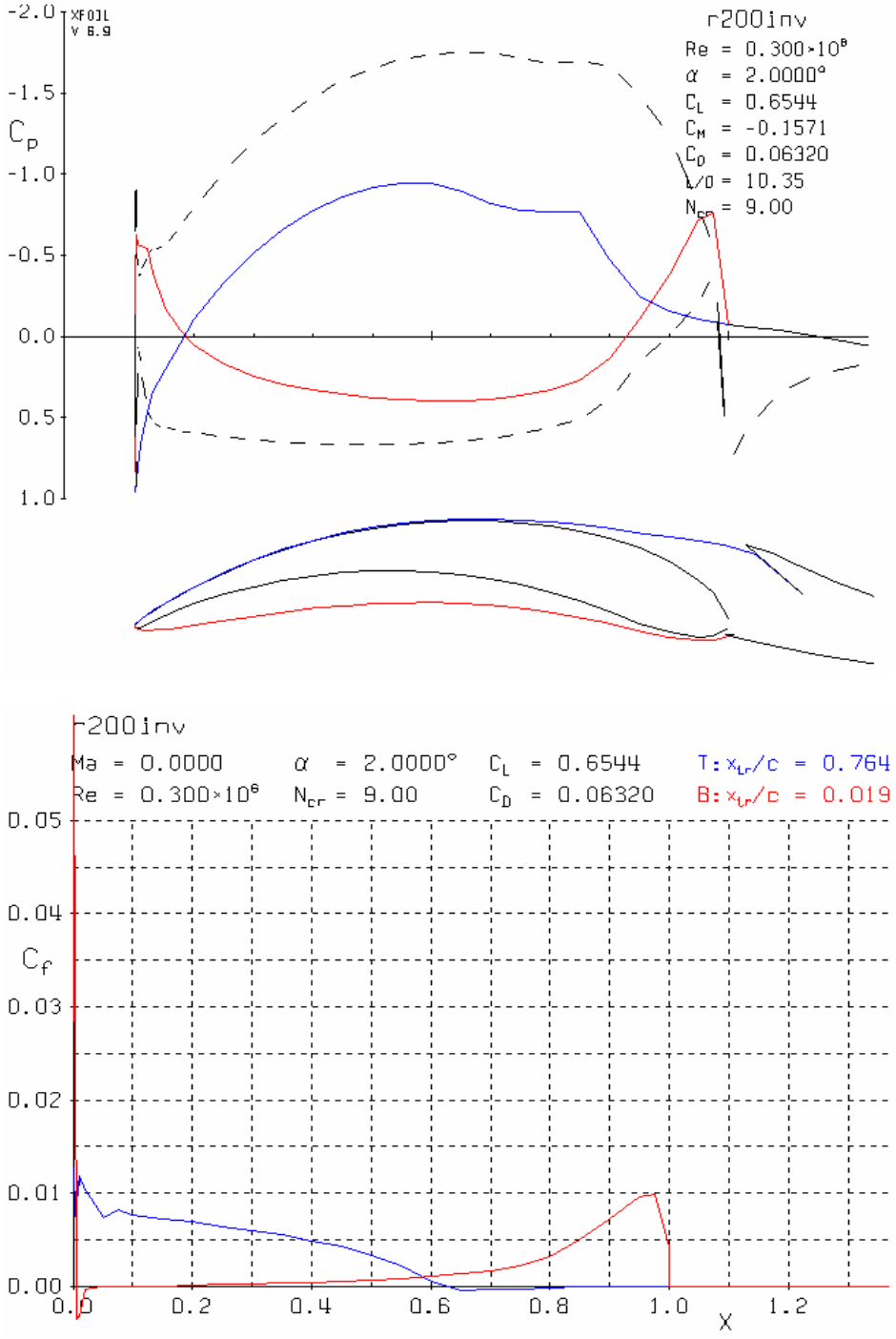
XFOIL
v 6.9
r200inv
Re = 0.300×10⁶
α = 2.0000°
C_L = 0.6544
C_M = -0.1571
C_D = 0.06320
L/D = 10.35
N_cr = 9.00
C_p
-2.0
-1.5
-1.0
-0.5
0.0
0.5
1.0
r200inv
Ma = 0.0000
α = 2.0000°
C_L = 0.6544
T: x_tr/c = 0.764
Re = 0.300×10⁶
N_cr = 9.00
C_D = 0.06320
B: x_tr/c = 0.019
C_f
0.05
0.04
0.03
0.02
0.01
0.00
0.0
0.2
0.4
0.6
0.8
1.0
1.2
X

Fig. 5.2.4.

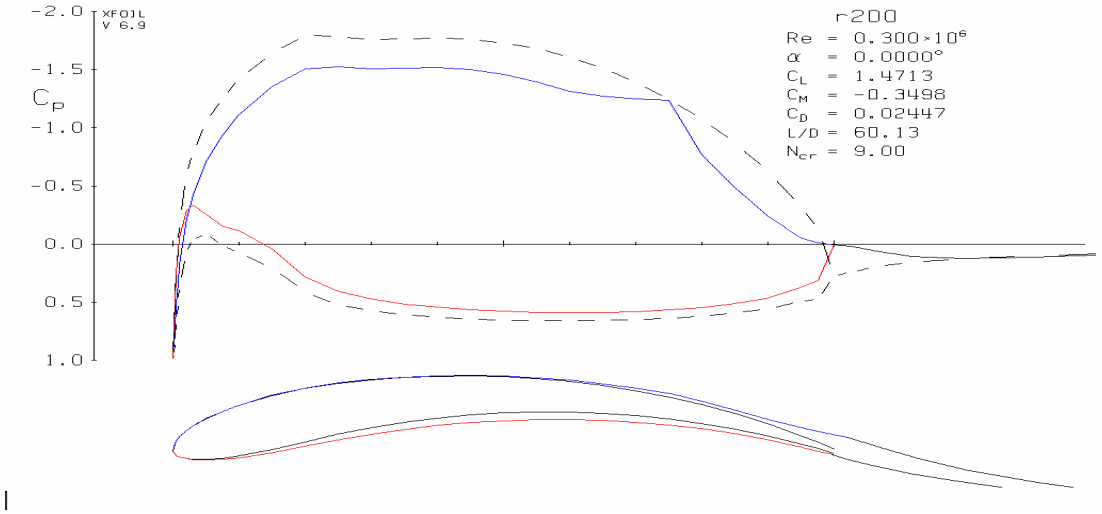
XFOIL
v 6.9
r200
Re = 0.300×10⁶
α = 0.0000°
CL = 1.4713
CM = -0.3498
CD = 0.02447
L/D = 60.13
Ncr = 9.00
Cp
-2.0
-1.5
-1.0
-0.5
0.0
0.5
1.0

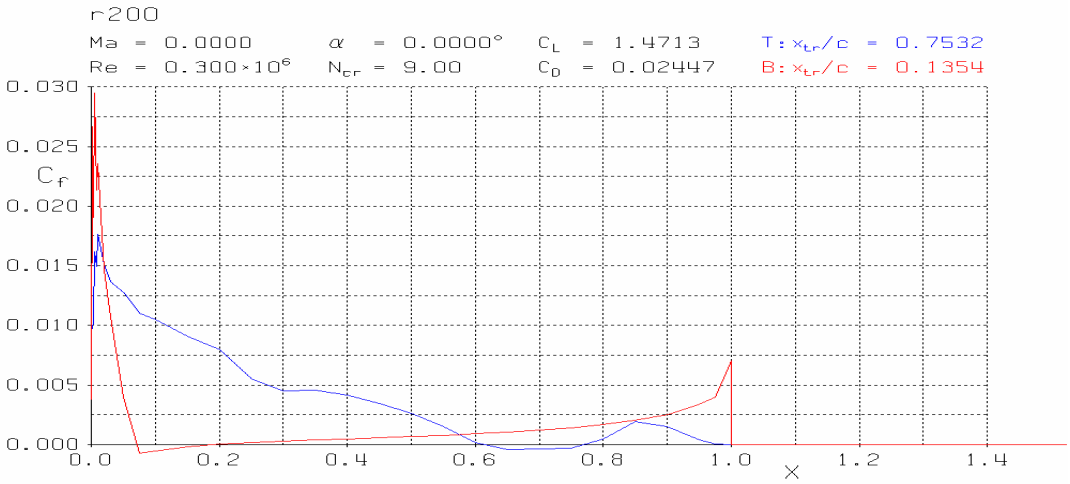
r200
Ma = 0.0000
α = 0.0000°
CL = 1.4713
T: xtr/c = 0.7532
Re = 0.300×10⁶
Ncr = 9.00
CD = 0.02447
B: xtr/c = 0.1354
Cf
0.030
0.025
0.020
0.015
0.010
0.005
0.000
0.0
0.2
0.4
0.6
0.8
1.0
1.2
1.4
x

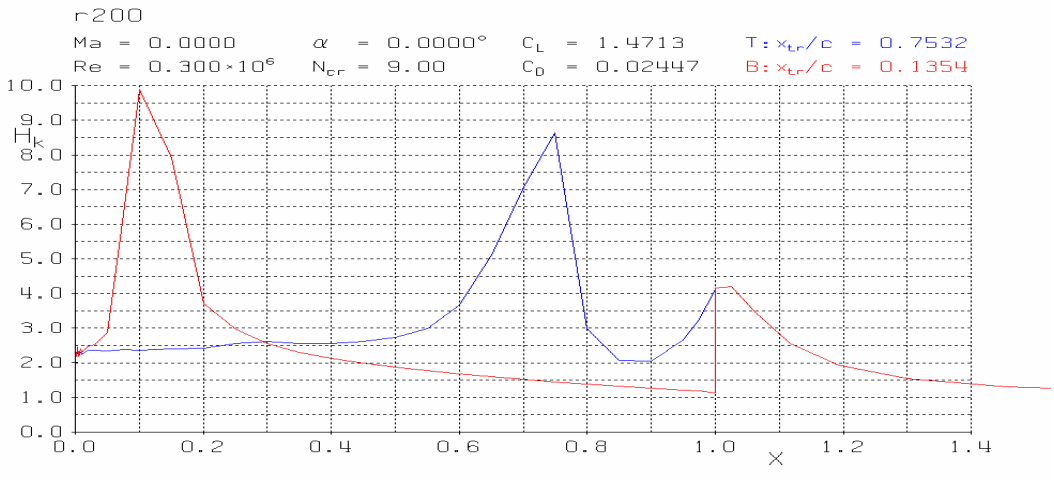
r200
Ma = 0.0000
α = 0.0000°
CL = 1.4713
T: xtr/c = 0.7532
Re = 0.300×10⁶
Ncr = 9.00
CD = 0.02447
B: xtr/c = 0.1354
Hk
10.0
9.0
8.0
7.0
6.0
5.0
4.0
3.0
2.0
1.0
0.0
0.0
0.2
0.4
0.6
0.8
1.0
1.2
1.4
x

Fig. 5.2.5.

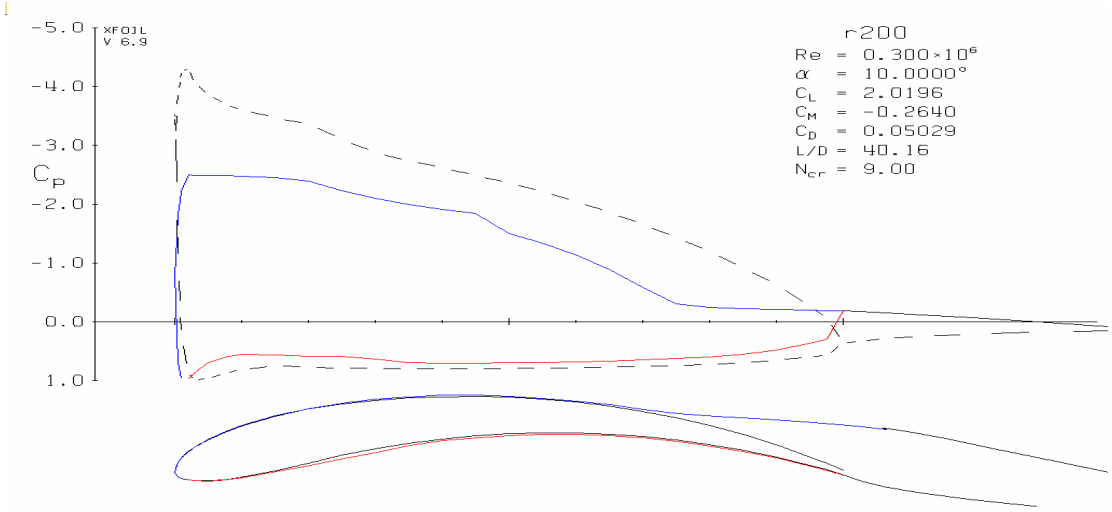
XFOIL
v 6.9
r200
Re = 0.300×10⁶
α = 10.0000°
CL = 2.0196
CM = -0.2640
CD = 0.05029
L/D = 40.16
Ncr = 9.00
Cp
-5.0
-4.0
-3.0
-2.0
-1.0
0.0
1.0

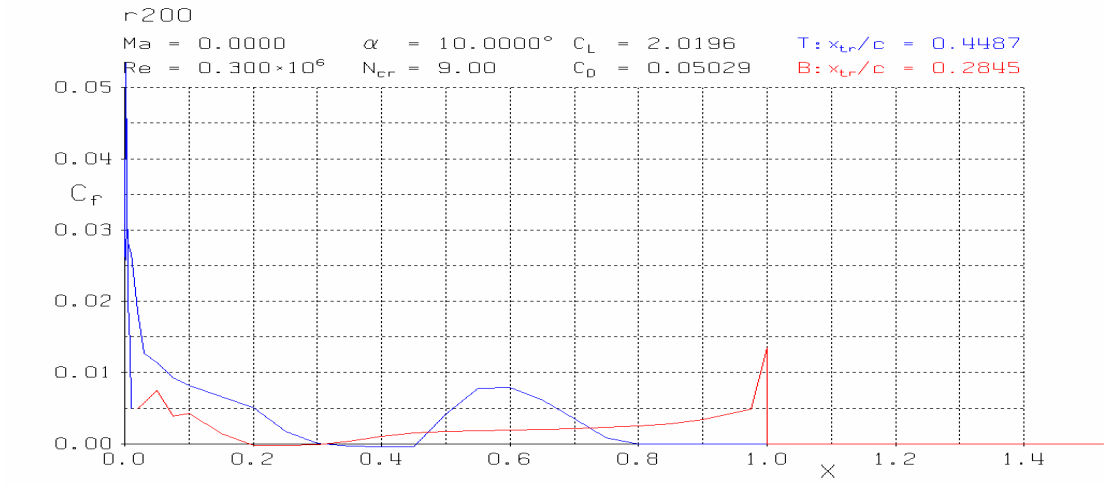
r200
Ma = 0.0000
α = 10.0000°
CL = 2.0196
T: xtr/c = 0.4487
Re = 0.300×10⁶
Ncr = 9.00
CD = 0.05029
B: xtr/c = 0.2845
Cf
0.05
0.04
0.03
0.02
0.01
0.00
0.0
0.2
0.4
0.6
0.8
1.0
1.2
1.4
x

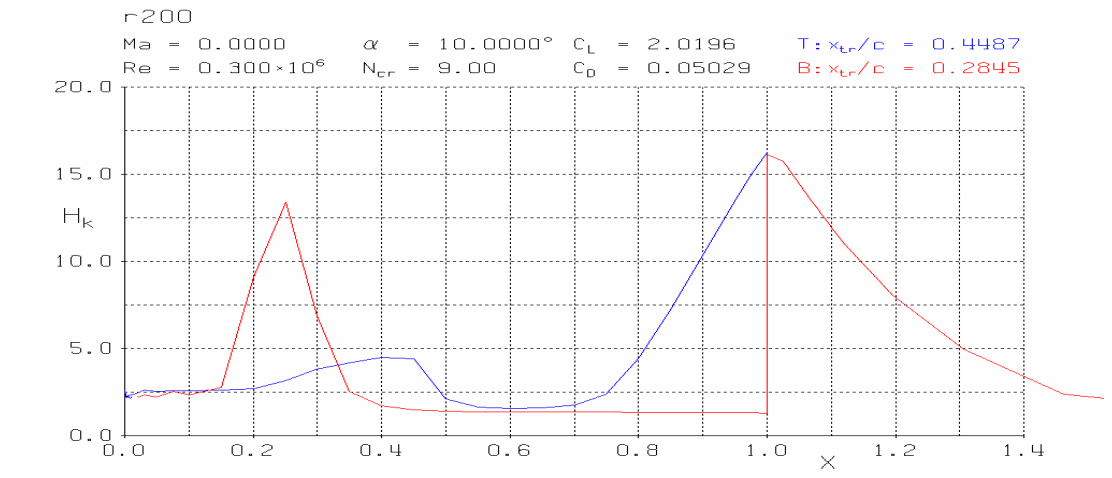
r200
Ma = 0.0000
α = 10.0000°
CL = 2.0196
T: xtr/c = 0.4487
Re = 0.300×10⁶
Ncr = 9.00
CD = 0.05029
B: xtr/c = 0.2845
Hk
20.0
15.0
10.0
5.0
0.0
0.0
0.2
0.4
0.6
0.8
1.0
1.2
1.4
x

Fig. 5.2.6.

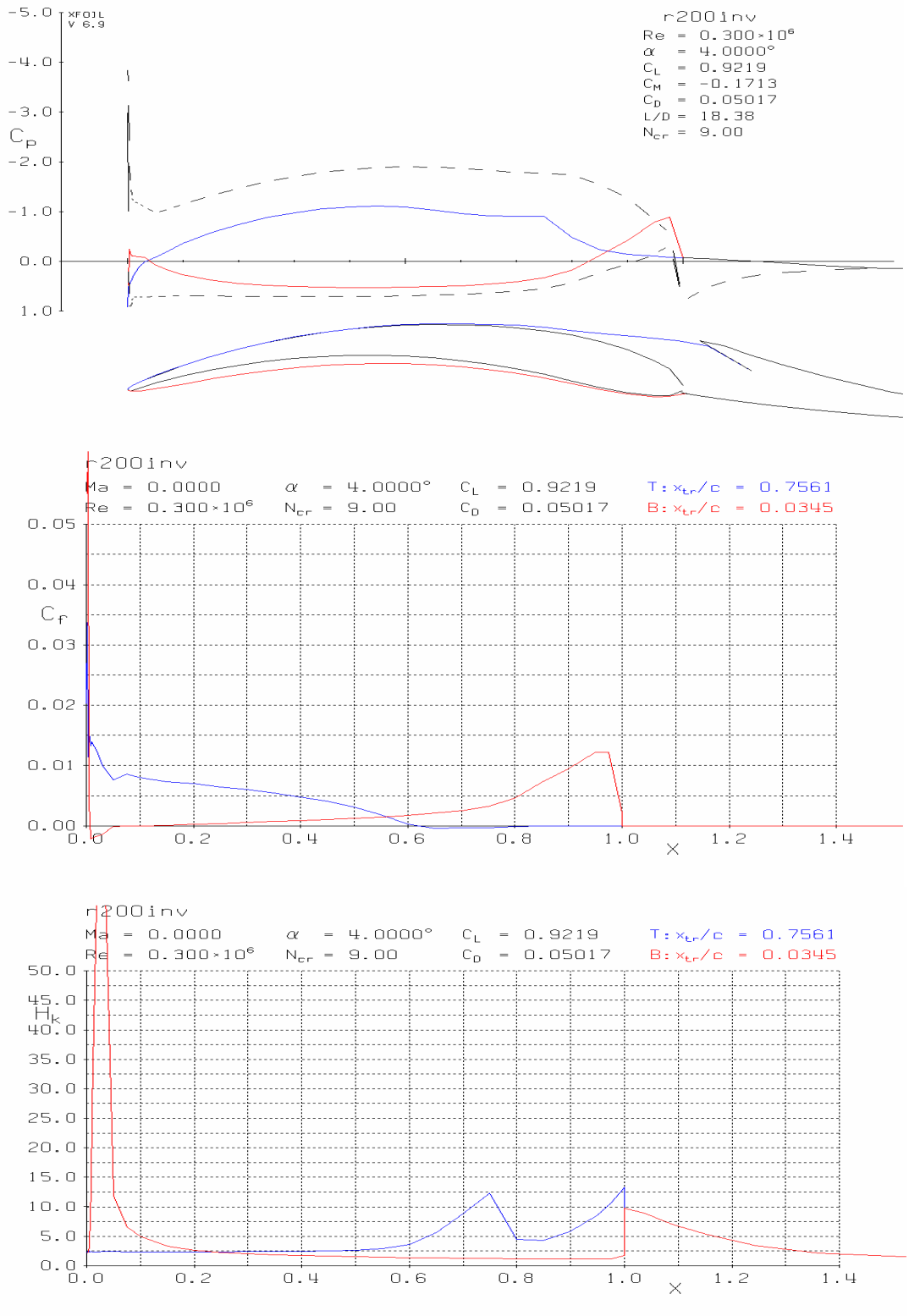
XFOIL
v 6.9
r200inv
Re = 0.300×10⁶
α = 4.0000°
C_L = 0.9219
C_M = -0.1713
C_D = 0.05017
L/D = 18.38
N_cr = 9.00
C_P
r200inv
Ma = 0.0000 α = 4.0000° C_L = 0.9219 T: x_tr/c = 0.7561
Re = 0.300×10⁶ N_cr = 9.00 C_D = 0.05017 B: x_tr/c = 0.0345
C_f
X
r200inv
Ma = 0.0000 α = 4.0000° C_L = 0.9219 T: x_tr/c = 0.7561
Re = 0.300×10⁶ N_cr = 9.00 C_D = 0.05017 B: x_tr/c = 0.0345
H_k
X

Fig. 5.2.7.

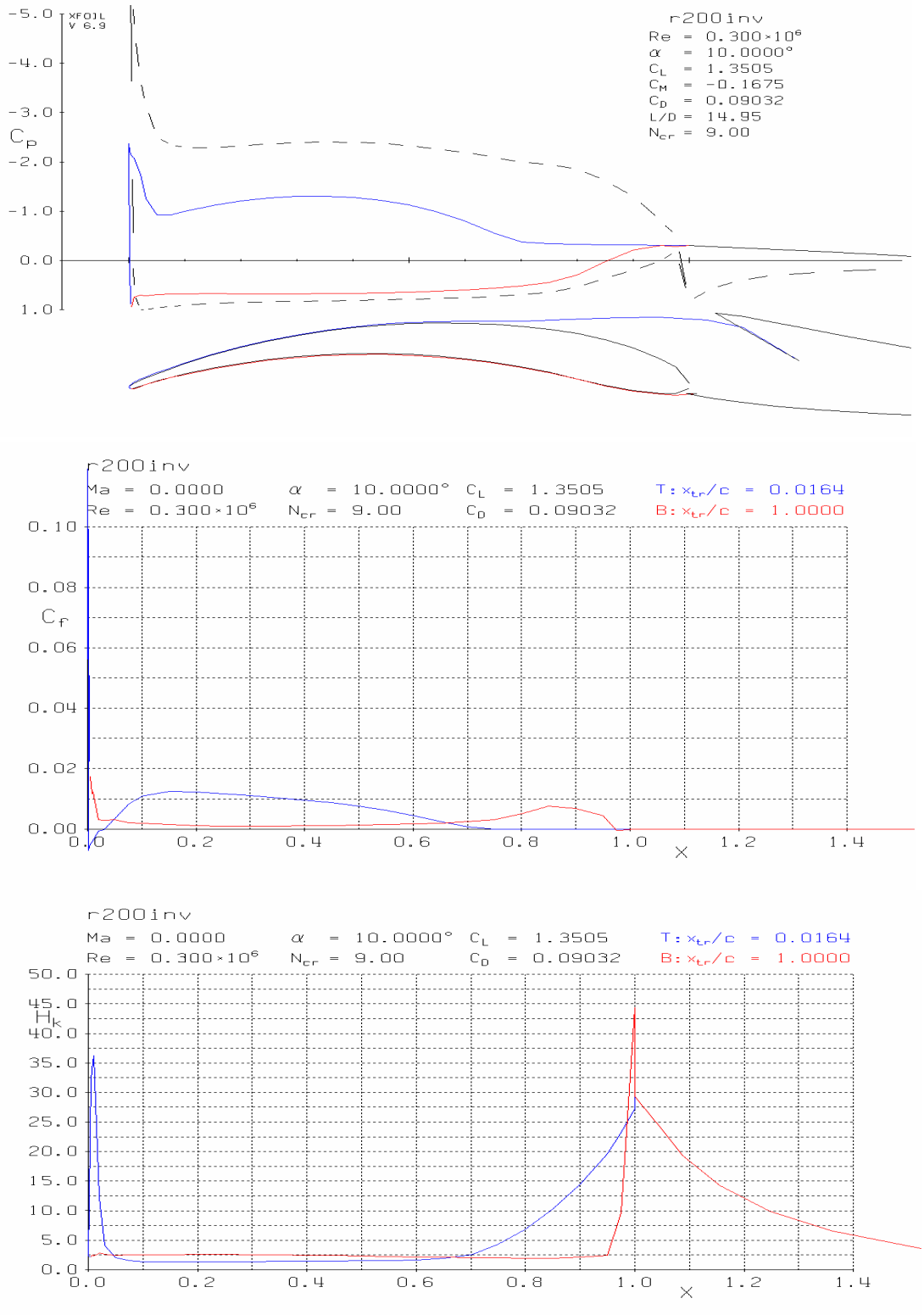
XFOIL
V 6.9
r200inv
Re = 0.300×10⁶
α = 10.0000°
C_L = 1.3505
C_M = -0.1675
C_D = 0.09032
L/D = 14.95
N_cr = 9.00
C_P
-5.0
-4.0
-3.0
-2.0
-1.0
0.0
1.0
r200inv
Ma = 0.0000
Re = 0.300×10⁶
α = 10.0000°
N_cr = 9.00
C_L = 1.3505
C_D = 0.09032
T: x_tr/c = 0.0164
B: x_tr/c = 1.0000
C_f
0.10
0.08
0.06
0.04
0.02
0.00
0.0
0.2
0.4
0.6
0.8
1.0
1.2
1.4
X
r200inv
Ma = 0.0000
Re = 0.300×10⁶
α = 10.0000°
N_cr = 9.00
C_L = 1.3505
C_D = 0.09032
T: x_tr/c = 0.0164
B: x_tr/c = 1.0000
H_K
50.0
45.0
40.0
35.0
30.0
25.0
20.0
15.0
10.0
5.0
0.0
0.0
0.2
0.4
0.6
0.8
1.0
1.2
1.4
X

Fig. 5.2.8.

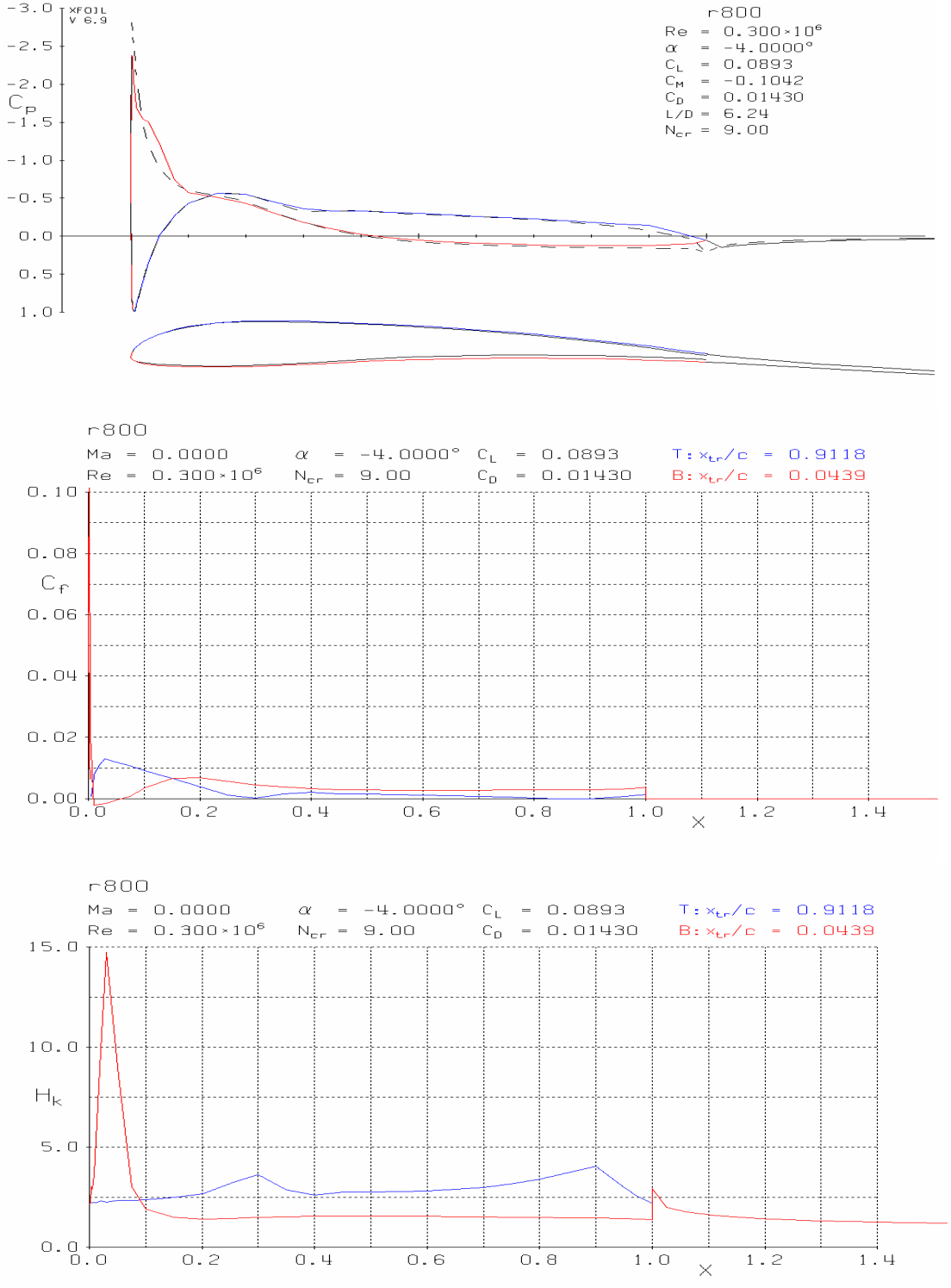
XFOIL
V 6.9
r800
Re = 0.300×10⁶
α = -4.0000°
CL = 0.0893
CM = -0.1042
CD = 0.01430
L/D = 6.24
Ncr = 9.00
Cp
r800
Ma = 0.0000
α = -4.0000°
CL = 0.0893
T: xtr/c = 0.9118
Re = 0.300×10⁶
Ncr = 9.00
CD = 0.01430
B: xtr/c = 0.0439
Cf
X
r800
Ma = 0.0000
α = -4.0000°
CL = 0.0893
T: xtr/c = 0.9118
Re = 0.300×10⁶
Ncr = 9.00
CD = 0.01430
B: xtr/c = 0.0439
Hk
X

Fig. 5.2.9.

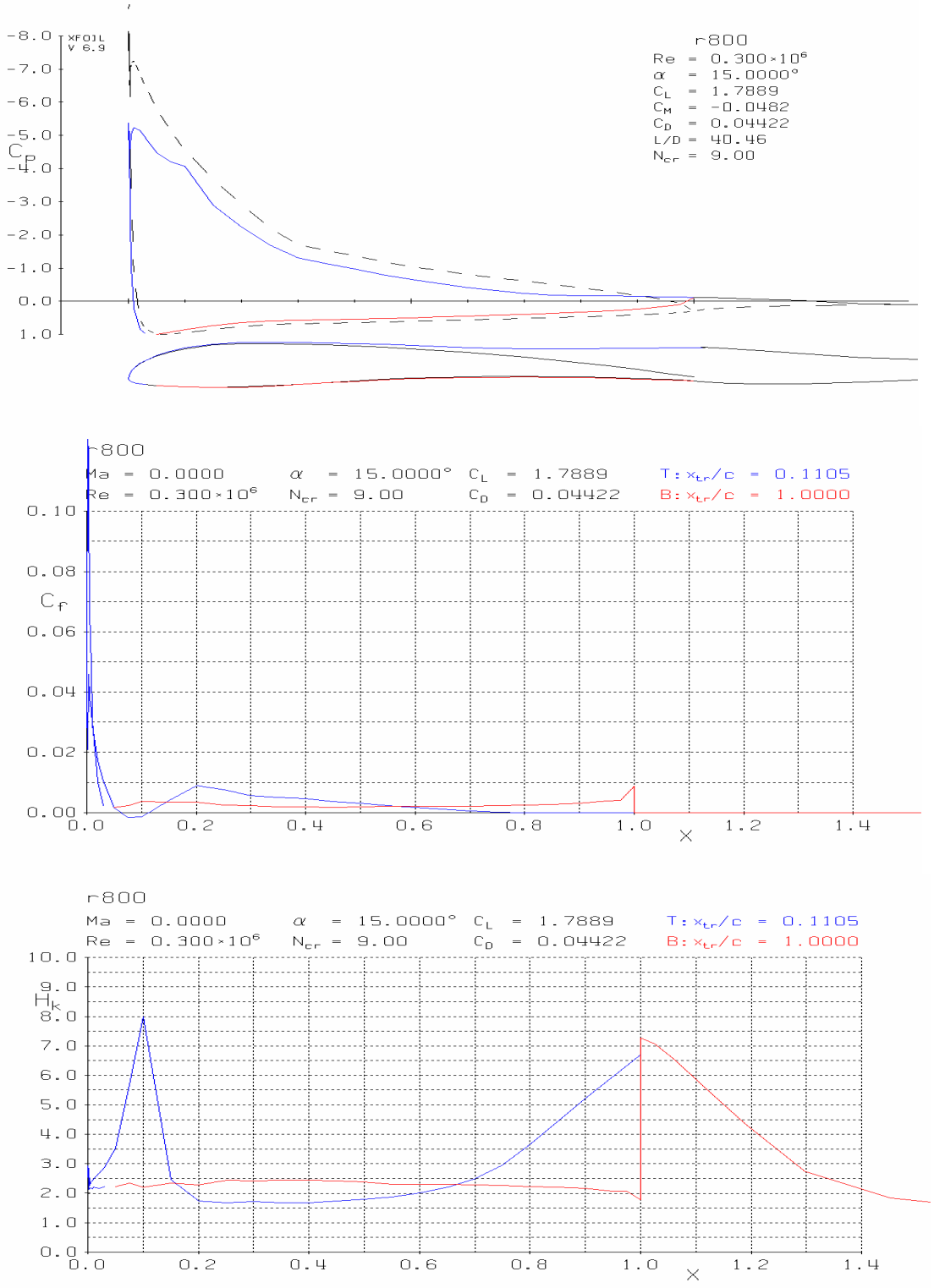
XFOIL
v 6.9
r800
Re = 0.300×10⁶
α = 15.0000°
C_L = 1.7889
C_M = -0.0482
C_D = 0.04422
L/D = 40.46
N_cr = 9.00
C_P
r800
Ma = 0.0000
Re = 0.300×10⁶
α = 15.0000°
N_cr = 9.00
C_L = 1.7889
C_D = 0.04422
T: x_tr/c = 0.1105
B: x_tr/c = 1.0000
C_f
X
r800
Ma = 0.0000
Re = 0.300×10⁶
α = 15.0000°
N_cr = 9.00
C_L = 1.7889
C_D = 0.04422
T: x_tr/c = 0.1105
B: x_tr/c = 1.0000
H_k
X

Fig. 5.2.10.

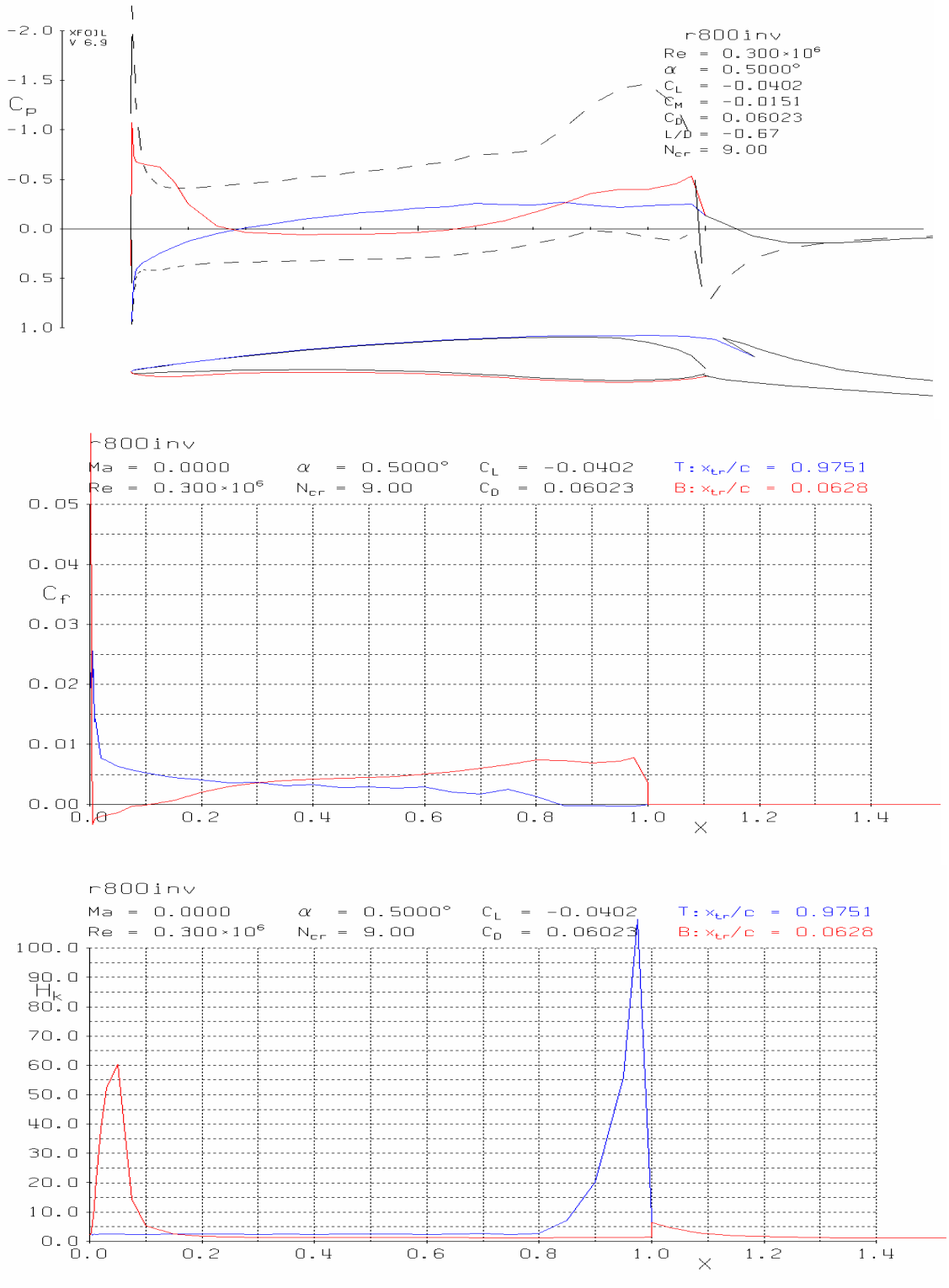
XFOIL
v 6.9
r800inv
Re = 0.300×10⁶
α = 0.5000°
C_L = -0.0402
C_M = -0.0151
C_D = 0.06023
L/D = -0.67
N_cr = 9.00
C_P
r800inv
Ma = 0.0000
α = 0.5000°
C_L = -0.0402
T: x_tr/c = 0.9751
Re = 0.300×10⁶
N_cr = 9.00
C_D = 0.06023
B: x_tr/c = 0.0628
C_f
X
r800inv
Ma = 0.0000
α = 0.5000°
C_L = -0.0402
T: x_tr/c = 0.9751
Re = 0.300×10⁶
N_cr = 9.00
C_D = 0.06023
B: x_tr/c = 0.0628
H_K
X

Fig. 5.2.11.

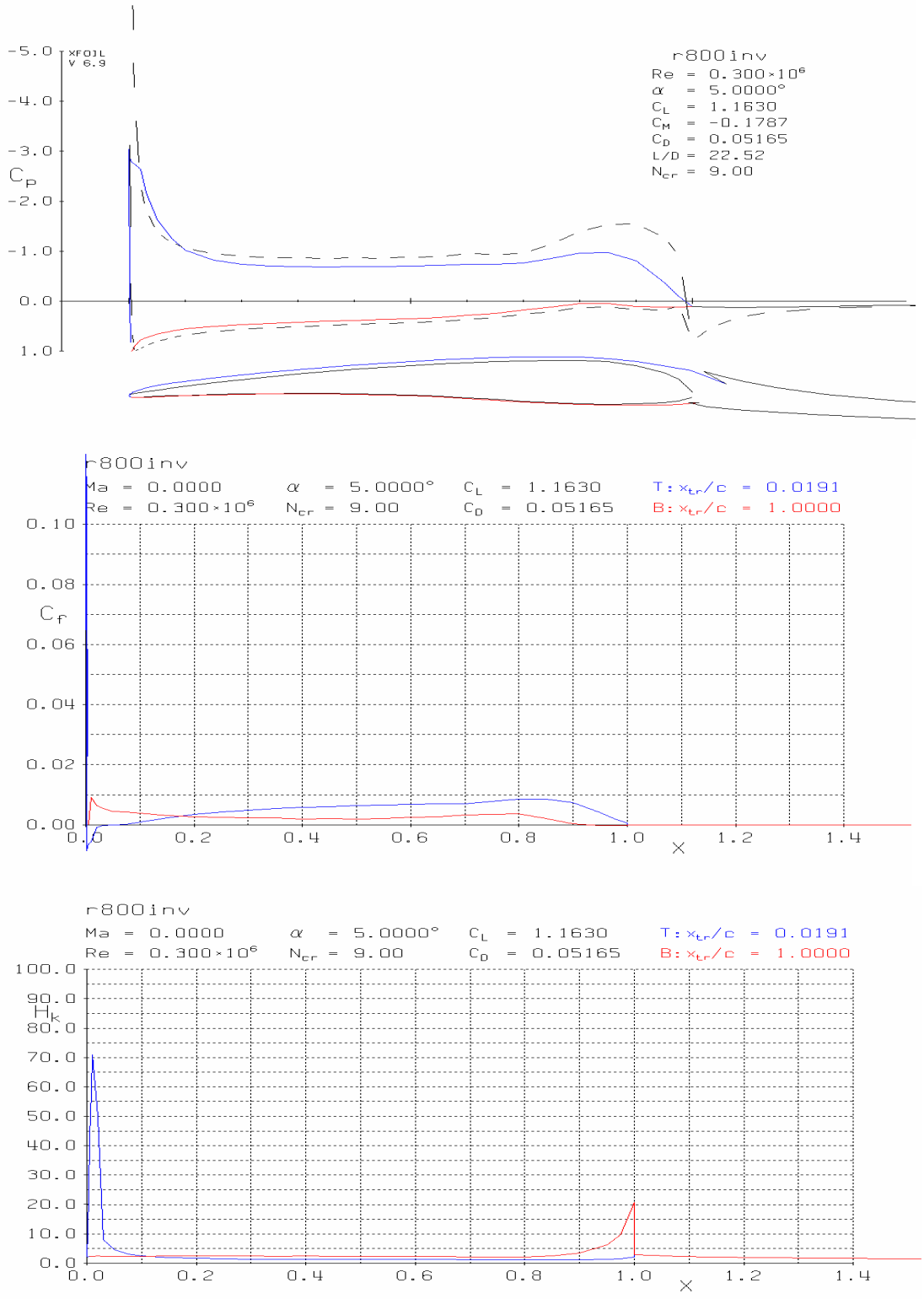
XFOIL
v 6.9
r800inv
Re = 0.300×10⁶
α = 5.0000°
CL = 1.1630
CM = -0.1787
CD = 0.05165
L/D = 22.52
Ncr = 9.00
Cp
r800inv
Ma = 0.0000
Re = 0.300×10⁶
α = 5.0000°
Ncr = 9.00
CL = 1.1630
CD = 0.05165
T: xtr/c = 0.0191
B: xtr/c = 1.0000
Cf
X
r800inv
Ma = 0.0000
Re = 0.300×10⁶
α = 5.0000°
Ncr = 9.00
CL = 1.1630
CD = 0.05165
T: xtr/c = 0.0191
B: xtr/c = 1.0000
Hk
X

Fig. 5.2.12.

Detailed results of calculations are presented above (see Figs 6-15) in a form of pressure distributions along the R200 and R800 models mounted directly and inversely, drag and lift coefficients, momentum and form parameter in a range of angles of attack corresponding to one planned in experiments. It was recommended to focus measurements on momentum and lift coefficients as most sensitive characteristics to distinguish flow control effects due to generated streamwise vortices.

5.3. Construction and fabrication of models and rigging

The purpose of investigations together with the analysis of the made calculations of pressure distribution around models for several versions of the airfoil geometry enabled to choose

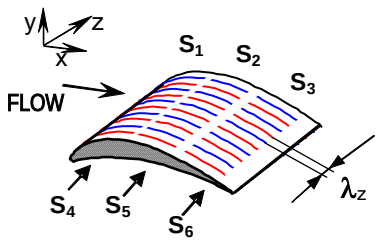

Fig. 5.3.1. Airfoil test model with 6 independent thermal control sections on its both sides

(1) optimal configuration of the model leading edge so that it would not provoke an early flow separation in a wider range of angles of attack (considered up to 20°);

(2) optimal downstream extension of 3 thermal control sections along the model pressure and suction sides depending on the pressure distribution so that the control effect could be reached with minimal efforts, e.g. using a minimal number of heated sections to compensate the unfavorable basic flow situation.

It resulted in acceptance of the design shown in Figs. 5.3.1, 5.3.2: 200 x 200 mm, λ_z = 2.5 and 5 mm provided due to the flush mounted high-resistance wires connected to the voltage source with independent electrical circuits. Preliminary design of test models supposed their maximum relative thickness to be C_{max}=0.15. However improved design of pressure probes that are to be installed inside the models allowed to reach a value of C_{max}=0.12 which corresponds to the better aerodynamic quality of the both airfoils.

Fig. 5.3.2. Fabrication of the 2 airfoil models

Requirements to materials of the test models were formulated as follows.

- High insulating properties of electrical circuits used both on a surface and within model bodies;
- Low thermal conductivity and high dielectric properties of the basic (body) material that would allow mounting of electrical/heating and pressure probes circuits inside a model;
- Sufficiently high insulating and strength properties of a surface layer, their high-quality processing to provide a smooth surface;
- Long-term thermal resistance of the construction for temperatures of 60-60°C.

Analysis of a set of materials with account of the mentioned requirements showed that priority is to be given to *foam plastic and cotton-based materials*. As a result, a composite multi-layer construction has been designed and given in the detailed construction drawings together with instructions for the fabrication technology. Thermal control circuit parameters were estimated that required 0.05 mm diameter Tungsten/Nichrome wires (about 80 pieces) that will be flush-mounted at a spanwise distance of 2.5 mm (i.e. an order of the boundary-layer thickness at a basic measurement section). Two isolated electrical circuits will provide a variable distance between the neighboring activated streamwise wires from 2.5 to 5.0 mm. Besides, three similar control sections will be arranged in a streamwise direction to study necessary and sufficient conditions to affect integral flow characteristics.

Thorough drainage of a surface along a model chord will make it possible to place 5 flush-mounted piezo-ceramic pressure probes to measure near-wall pressure fluctuations and correlation functions.

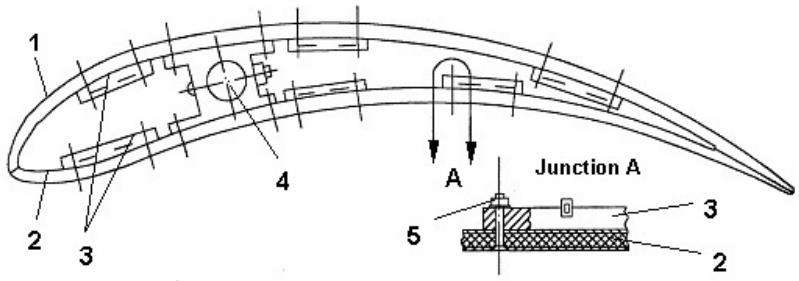

Fig. 5.3.3. Construction of the airfoil model, side view:
1 – convex panel; 2 – concave panel; 3- voltage clamps for heated wires;
4 – holder to provide airfoil inflexibility; 5 – standard screw junction

The test airfoil body was constructed as a hollow shell (Fig. 5.3.3) fabricated from a multi-layer material with a total thickness of 4 mm. Two external and two internal layers are made from cotton and the middle one from the special fine-pore foam plastic (for more detail, see Fig. 5.3.4). All the layers are glued together in vacuum using a thermo-resistant resin. Upper and lower (convex and concave) parts of the model are made sectional with individual heating circuits, drainage and piezo-ceramic pressure probes. The partly open hollow of the model is meant to provide heat exchange with the environment so that to prevent internal general heating of the model, i.e. to maintain the spanwise periodic temperature gradient. Bracket holders fixing the two panels together serve also to take wires of heaters and pressure probes, to provide necessary rigidity of the model and to mount it in the wind tunnel test section.

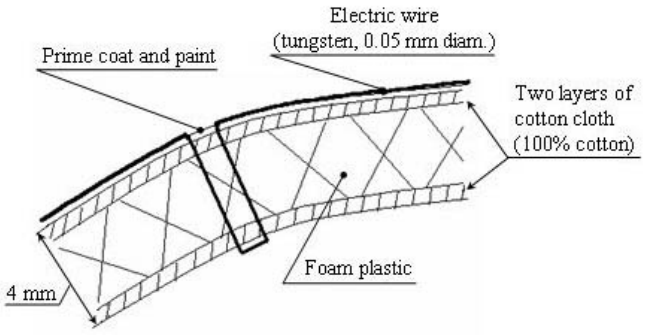

Fig. 5.3.4. Design of the model shell providing thermal control of a near-wall flow

The essential issue of the model fabrication relates to the design of the heating control system. It is shown in the scaled drawing of electrical heating (Fig. 5.3..5). Separate electrical circuits are arranged so that to prevent any mutual interaction between the heated sections. Heating is organized so that switching on different circuits, one can induce spanwise scales of disturbances λ_z=2.5 and 5 mm. In addition, three streamwise heated sections over both sides of the model are made in order that to find optimal control regimes for given flow conditions due to variation of both intensity (applied voltage) and scale (a distance between the neighboring heated wires) of generated disturbances.

Additionally, there were designed and fabricated simpler test models. They were necessary to provide parallel jobs and various adjustment studies. Two of them (identical to R200 and R800 but without the thermal control) were used to investigate general aerodynamic properties of the airfoils, others were made for elaboration of thermal conditions for boundary-layer control like a choice of proper materials, heating and measurement methods, configuration of heating elements along a surface, optimal temperature difference between them and an ambient flow, operation possibilities to vary flexibly control parameters during experiments. The latter was made with the flat-plate model of 300 mm (chord), 200 mm (span), and 4 mm (thickness). Its leading and trailing edges were sharpened with an angle of 20°.

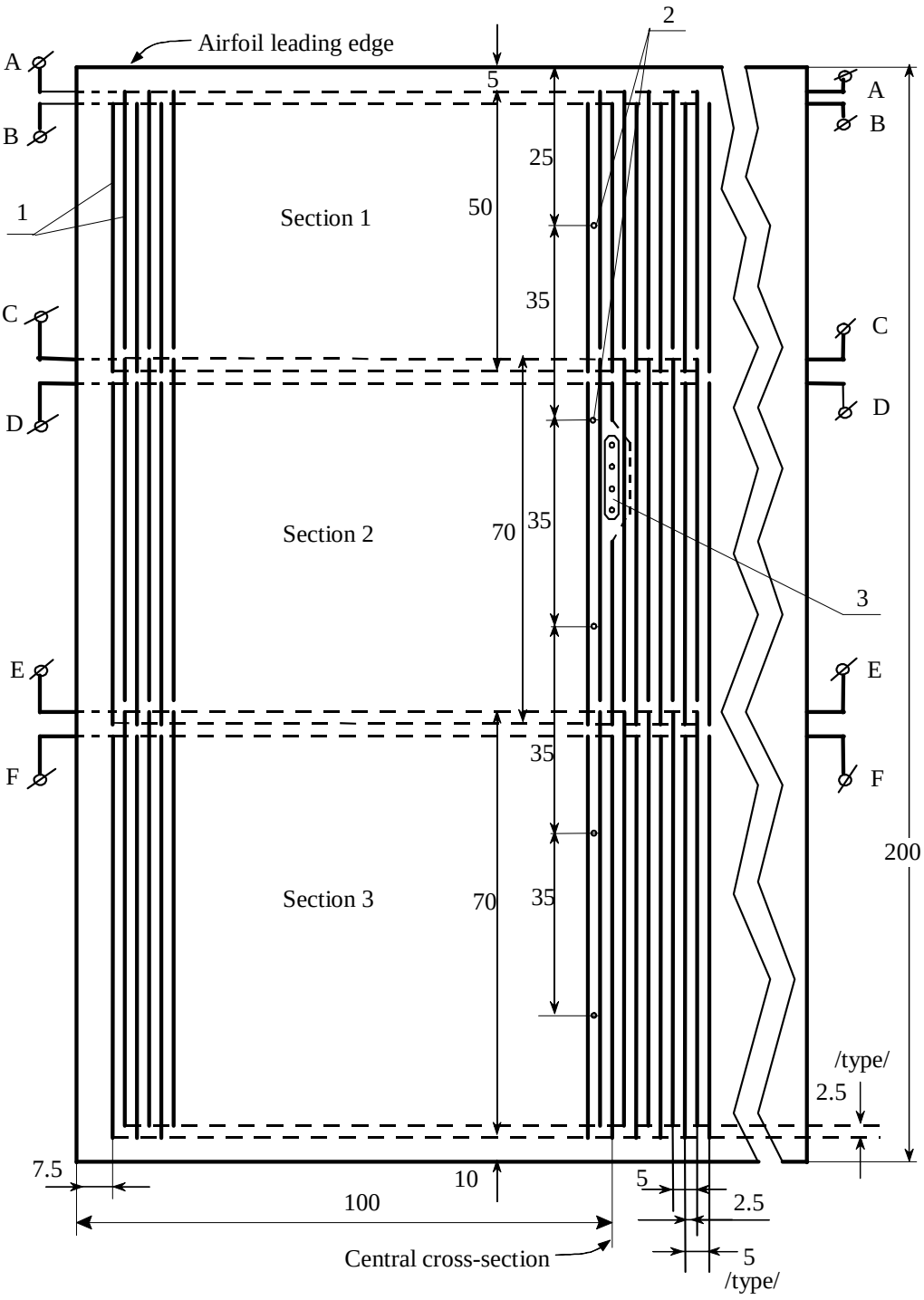

Fig. 5.3.5. Sketch of the thermal control arrangement in the airfoil model: 1 - electrical circuits, heated Nichrome wires of ⌀ 0.1 mm; 2 - drainage points for single pressure probes; 3 - blocks of piezo-ceramic pressure probes

6. EXPERIMENTAL FACILITIES, THEIR PREPARATION TO MEASUREMENTS. CALIBRATIONS, MEASUREMENT OF BASIC FLOW PARAMETERS, ACCURACY OF MEASUREMENTS

6.1. Wind Tunnels WT1 and WT2

Analysis of necessary measurement tools, data acquisition and processing systems was made in conformity with the wind tunnels of IHM (WT1) and NAU (WT2). They are 3-component strain gauge, manometer, visualization system, pressure and temperature probes, angle of attack indicator. The system is developed to conjugate pressure probes and strain gauges with a multi-functional extension board PCI-1002 and PC operating under "Windows". Angle of attack are to be measured and the data transmitted in the same PC through the Encoder-300 board, which provides the accuracy no less than 3°.
Following this working plan, both mentioned boards have been purchased and 7 miniature pressure probes with pre-amplifiers were designed and fabricated according to the given requirements of the model geometry and intended measurements. The basic parameters are as follows: 1.5 mm sensitive element (to be flush-mounted between heated strips placed at a minimum distance of 2.5 mm from each other), sensitivity of 5 μV/Pa (to measure turbulent fluctuations and correlation functions near the wall). The pressure probes will be calibrated and certified after specially ordered test measurements.

The scheme of experimental arrangement is shown in Fig. 6.1.1.

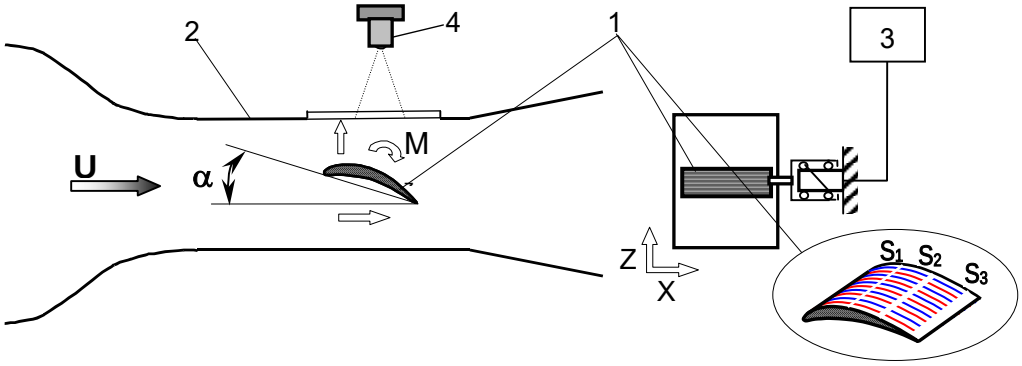

Fig. 6.1.1. Wind tunnel arrangement:
1 – airfoil test model with 3 sections of heated strips; 2 – wind-tunnel test section;
3 – voltage source; 4 – camera/measurement system

Wind Tunnel WT1 of the Hydromechanics Institute, Department of Thermal and Fluid Dynamic Modeling, (see sketch of Fig. 6.1.1) can operate both in an open and closed type regimes; it has 0.2 m x 0.5 m x 3.0 m test section with a rectangular cross section, free-stream turbulence level 0.02%, free-stream velocity up to 18 m/s. WT1 was renovated and adjusted to the set of experiments according to the formulated experimental tasks of the project. Side walls of the test section were changed for the glass to enable the application of flow visualization methods. Two additional windows were made to provide a better access and operation with the test model and measurement systems during experiments. Tweaking of an airfoil model mounted in the test section required fabrication of special washers to imitate an infinite-span wing (so that to reduce the problem to 2D case as it was considered, for instance, in calculations of drag and lift coefficients depending on an angle of attack). The strain gauge was mounted for the force measurements, software was installed for data processing during the experiments.

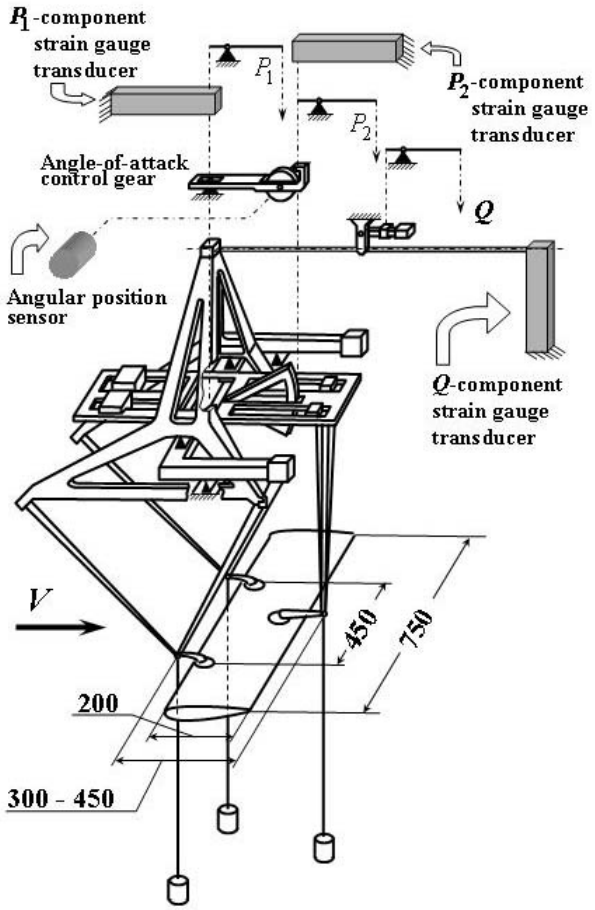

Fig. 6.1.2. Chart of the WT2 strain gauge

Wind Tunnel of National Aviation University (WT2) is of a closed type with an oval 0.42 m x 0.7 m x 1.5 m test section, free-stream velocity up to 28 m/s; equipped with the 3-component strain gauge shown in Fig. 6.1.2 (values of streamwise and normal forces measured up to 3N and 6 N correspondingly, measurement error no more than 1.5%). WT2 was equipped with the system for dynamic pressure measurements that was based on the available devices which were renovated and supplemented with newly developed parts. For efficient operation, the software for data acquisition and processing was developed using drivers of the of analog-digital converter purchased in the framework of the P-053 project. Tests and calibration were carried out for the whole measurement channel in a range of pressure values of 0 – 500 Pa corresponding to the velocity range of 0 – 29 m/s at a standard air density of 1.225 kg/m^3.

WT2 as well as the three-component balance for strain-gaging were inspected, adjusted and calibrated for the objectives of the project tasks. The results of the WT2 calibration are shown in Table 6.1.1.

Table 6.1.1. WT2 parameters

Parameter	Value		
1. Free-stream U_∞ velocity range	3.2 ÷ 28 m/s		
2. Ratio error Δ, m/s of measured velocity values; flow instability, δ, %	Δ, m/s	Requirements to Δ, m/s according to the state standard 8.542-86	δ, %
3,2	0,05	0,051	0,65
5	0,06	0,078	0,6
7	0,1	0,108	0,6
10	0,12	0,153	0,5
15	0,18	0,228	1,0
28	0,3	0,423	0,8

Free-stream turbulence level was carefully measured after all the renovations and adjustments and was found to be **ε=2.4%** at U_∞ = 18.7 m/s, i.e. Re= 1.2x10^5.

The channel output signal is known to depend on temperature that results in a parallel shift of the calibration curve. Therefore pressure depending on the output voltage can be expressed by

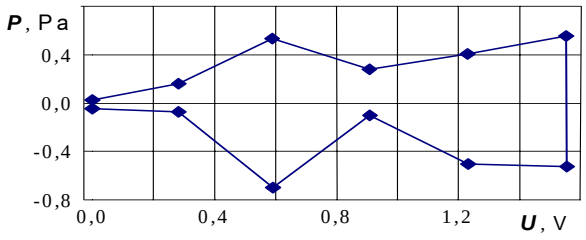

Fig. 6.1.3. Discrepancies given by a polynomial model of a transfer function

$$q = b_0 + \sum_{i=1}^{4} b_i (u - u_0)^i , \qquad (1)$$

where u is a running value of an output voltage and u_0 the value of voltage at a zero value of dynamic pressure.

As it is seen from Fig. 6.1.3, maximum discrepancy was found to be 0.7 Pa that corresponds to the inaccuracy of measurements no more than **0.7 Pa** within the operation velocity range of WT 2.

Calibration of the multi-component balance for strain-gaging was carried out using a transfer function in a form of a regression model:

$$P_j = a_{i0} + \sum_{i=0}^{3} a_{ji} (u_j - u_{0j}) \qquad \{P_j \in \mathbf{P1, P2, Q}\} , \qquad (2)$$

where P_j is a component of a measured load, u_j is an output signal of the *j*-component, u_{0j} is a reference output signal of the *j*-component measured without an aerodynamic loading, a_{ji} are the found coefficients shown in Table 2. This form is chosen to take into account possible interference of components.

Table 6.1.2 shows absolute errors Δ of measured components with account of discrepancies at confidence probability equal to 0.9.

Table 6.1.2. Coefficients for the aerodynamic balance of WT2

j	R^2	a_{j0}	a_{j1}	a_{j2}	a_{j3}	Δ, H
1	1.0000	0.0014	5.4401	0.0	0.0143	±0.01
2	1.0000	0.0145	0.0	5.8969	-0.0538	±0.02
3	0.9996	-0.0708	-0.0321	0.1196	-5.7437	±0.14

6.2. Experiment arrangements and reference boundary-layer measurements in WT1 and WT2

Measurement of forces in the WT2 was organized as it is shown in the general schemes of Figs. 6.2.1 and 6.2.2:

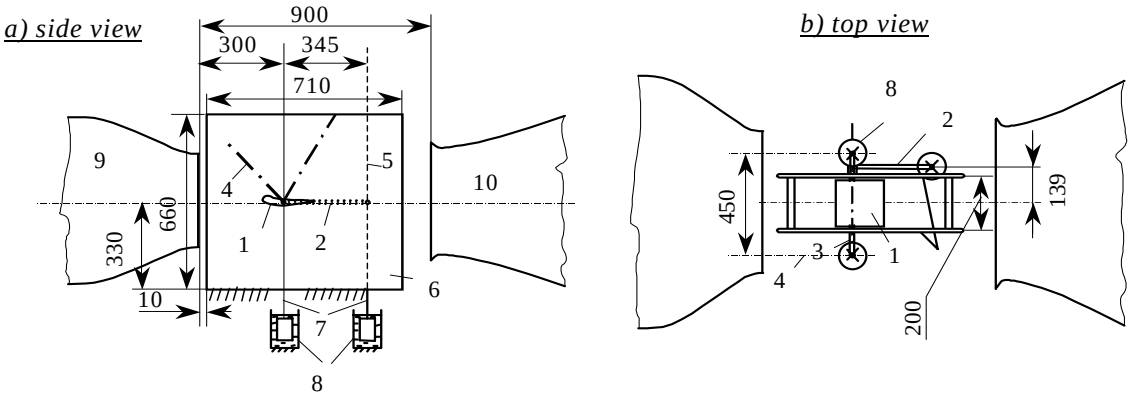

Fig. 6.2.1. Arrangement of the WT2 test section with the installed airfoil model :
1 – model; 2 – trailing-edge holder; 3 – leading-edge holder; 4, 5 – aerodynamic balance strip-holders; 6-side washers; 7 – counterweights with control-rods; 8 – damping vessels; 9 – nozzle; 10 – diffuser

- Airfoil models are mounted on the aerodynamic balance in three points that form a lateral base of l_z=450 mm and the longitudinal base of l_x=345 mm;
- Side aerodynamic washers are used to increase the airfoil effective elongation, the distance between washers and the model surface having been no more than 1 mm;
- Trail holder is mounted so that to exclude its influence on a boundary layer flow in case of the model reversed placement in a test section (i.e. with its trailing edge looking upstream).

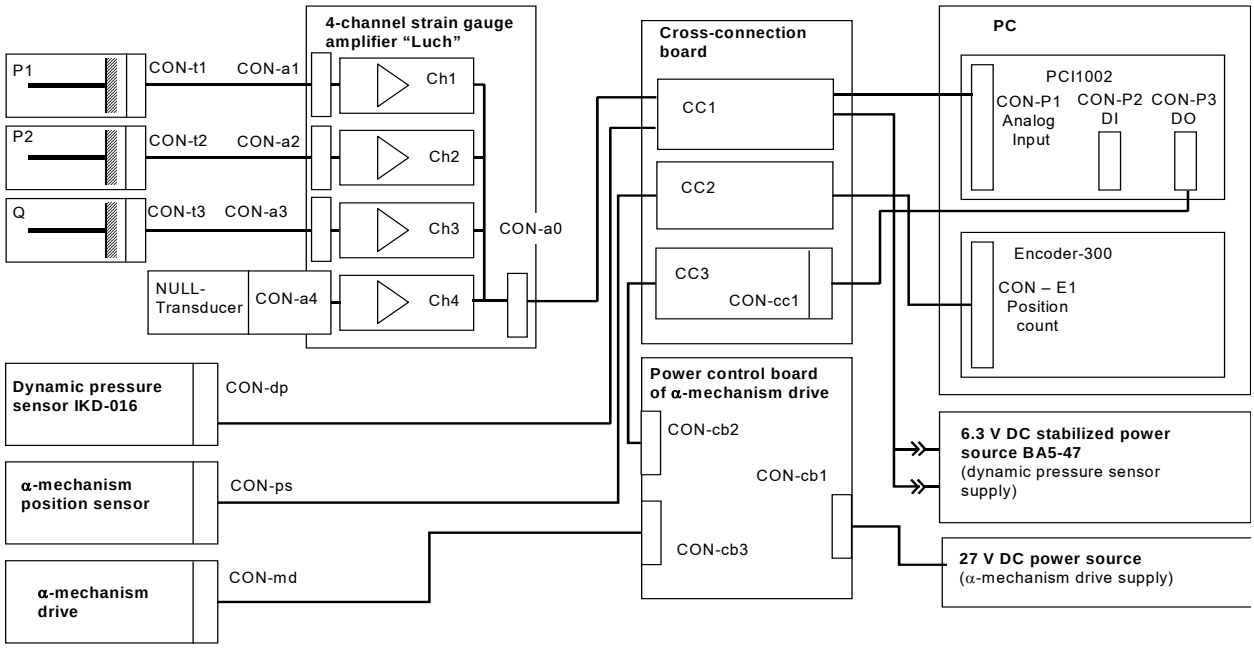

Fig. 6.2.2

The software has been developed and tested for the balance experiments in WT2 to provide automatic measurement of the output balance and the flow-meter signals as well as to calculate aerodynamic coefficients c_x, c_y and m_z in a conventional coordinate system. Balance and flow-meter calibration has been performed repeatedly before the tests. Besides, noise in the output signals has been digitally filtered during the process of measurements that enabled to decrease mean root square deviations from 2.5 to 5 times depending on the angle of attack, i.e. to obtain high accuracy of measurements up to $\sigma_{c_x} = 0.002...0.005$, $\sigma_{c_y} = 0.008...0.015$, $\sigma_{m_z} = 0.001...0.005$.

Capacity of the whole system for work and adjustment measurement results are shown in Fig. 6.2.3.

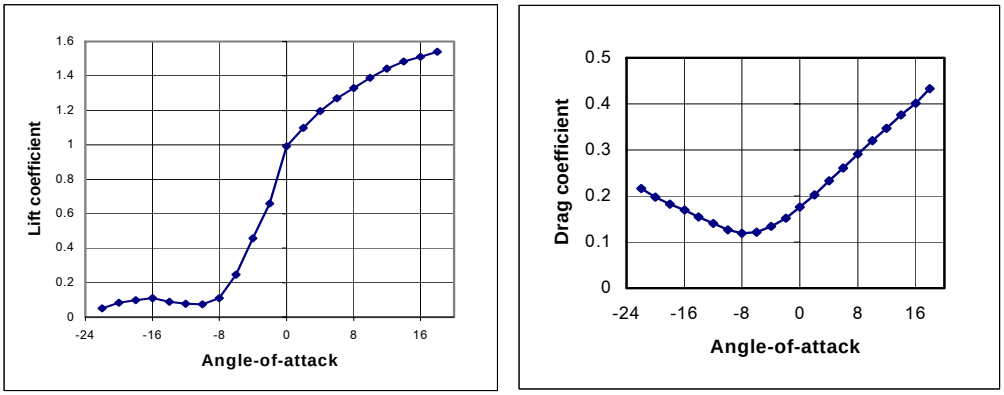

Fig. 6.2.3. WT-2 measurements of the airfoil model with the basic curvature radius R=200 mm

Reference measurements of aerodynamic characteristics of the airfoil models in WT1 were carried out at $U_\infty \approx 20$ m/s in a range of R800 model angles of attack $\alpha = -20° \div 45°$, the angle of attack having been determined between a flow vector and a tangent to the airfoil profile. The model cross-section square was F = 0.1 m^2.

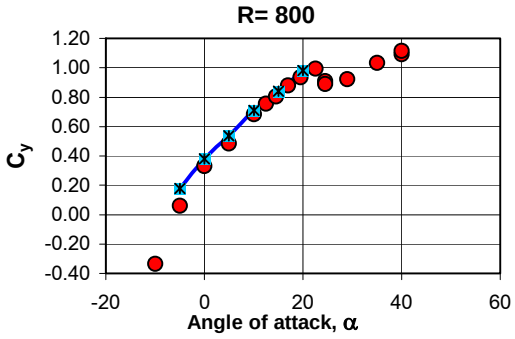

Fig. 6.2.4. Measured (red) and calculated (blue) lift coefficients for the airfoil with R=800 mm depending on an angle of attack

Preliminary experiments gave values of drag X and lift Y. Aerodynamic coefficients were found as $X= C_xSq$; $Y=C_ySq$, where $q=(1/2)\rho U^2$.

A typical feature of $C_y(\alpha)$ was found to be a distinct maximum of C_y at $\alpha \approx 35°$ for the airfoil model R 200 and $\alpha \approx 22{,}5°$ for the model R 800 (See Fig. 6.2.4). It relates to the boundary layer separation under these conditions and the development of a new vortical structure.

These results were considered as the reference data for further measurements under various flow and control conditions.

Momentum and lift coefficients appeared to be the most sensitive parameters to distinguish the influence of a near-wall vortical structure modification on integral characteristics.

References

1. Anders, J.B. Large-eddy breakup devices as low Reynolds number airfoiles . SAE Tehn. Pap. 861769, 1986.
2. Anders, J.B., Walsh, M.J., Bushnell, D.M. The fix for tough spots. 1988, *Aerosp. Amer.*, 26 (1), pp.24-27.
3. Andersson, H.I. Organized structures in rotating channel flow, in *Simulation and Identification of Organized Structures in Flows*, 1999, pp. 81-90, Kluwer
4. Aubry, N., Holmes, P., Lumley, J.L., Stone, E. The dynamics of coherent structures in the wall region of a turbulent boundary layer. 1988, *J. Fluid Mech.*, 192, pp.115-173.
5. Babenko, V.V., Voropaev, G.A. Control of coherent structures in a boundary layer. *Hydromechanics*, 1996, 70, pp.12-20 (in Russian)
6. Bacher, E.V., Smith, C.R. Turbulent boundary-layer modification by surface riblets. 1986, *AIAA J.*, 24 (8), pp.1382-1385.
7. Bakewell, H.P., Lumley, J.L. Viscous sublayer and ajacent region in turbulent pipe flow. 1967, *Phys. Fluids*, 10, pp.1880-1889.
8. Balakumar, P., Widnall, S.E. Application of unsteady aerodynamics to large-eddy breakup devices in a turbulent flow. 1986, *Phys. Fluids.*, 29 (6), pp.1779-1787.
9. Bandyopadhyay, P.R. Viscous drag reduction of a nose body. 1989, *AIAA J.*, 27 (3), pp.274-282.
10. Bandyopadhyay, P.R., Watson, R.D. Pressure field due to drag reducing outer layer devices in turbulent boundary layers. 1987, *Exp. Fluids.*, 5 (6), pp.393-400.
11. Berman, N.S. Drag reduction by polymers. 1978, *Ann. Rev. Fluid Mech.*, 10, pp.47-64.
12. Blackwelder, R. F. Analogies between transitional and turbulent boundary layers, 1983, *Phys. Fluids* **26** (10), 2807
13. Blackwelder, R.F. Coherent structures associated with turbulent transport, in M.Hirata and N.Kasagi (ed.), 1988, *Transport Phenomena in Turbulent Flows*, Hemisphere Publ. Corp., 69-88
14. Blackwelder, R.F., H. Eckelmann, Streamwise vortices associated with the bursting phenomenon. 1979, *J. Fluid Mech.*, 94, pp.577-594.
15. Blackwelder, R.F., Haritonidis, J.H. Scaling of the bursting frequency in turbulent boundary layers. 1983, *J. Fluid Mech.*, 132, pp.87-103.
16. Blackwelder, R.F., Kovasznay, L.S.G. Large-scale motion of a turbulent boundary layer during relaminarization. 1972, *J. Fluid. Mech.*, 53, pp.61-78.
17. Blackwelder, R.F., Kovasznay, L.S.G. Time scales and correlations in a turbulent boundary layer. 1972, *Phys. Fluids.*, 15 (9), pp.1545-1554.

18. Blackwelder, R.F., Roon, J.B. The effects of longitudinal roughness elements upon the turbulent boundary layer. 1988, AIAA Pap.88-0134,
19. Brown, G.L., Thomas, A.S.W. Large structure in a turbulent boundary layer. 1977, *Phys. Fluids.*, 20 (10), pt.2., pp.243-252.
20. Bushnell, D.M. Body-turbulence interaction . 1984, AIAA Pap. 84-1527.
21. Bushnell, D.M. Turbulence sensitivity and control in wall flows. 1985, Theor. Approaches Turbul., New York e.a., pp.1-18.
22. Bushnell, D.M., McGinley, C.B. Turbulence control in wall. 1989, *Ann. Rev. Fluid Mech.*, 21, pp.1-20.
23. Cantwell, B.J. Organized motion in turbulent flow. 1981, *Ann. Rev.Fluid Mech*., 13, pp.457-515.
24. Chen, C.H.P., Blackwelder, R.F. Large-scale motion in a turbulent boundary layer: A study using temperature contamination . 1978, *J. Fluid Mech.*, 89, pp.1-31.
25. Corino, E.R., Brodkey, R.S. A visual investigation of the wall region in turbulent flow. 1969, *J. Fluid Mech*., 37, pt.1, pp.1-30.
26. Corke, T.C., Guezennec, Y.G., Nagib, H.M. Modification in drag of turbulent boundary layers resulting from manipulation of large-scale structures. 1981, NASA CR-3444.
27. Craft, T. J. and Launder, B. E., 'A Reynolds-stress closure designed for complex geometries', *International J. Heat & Fluid Flow*, 1996, 17, pp. 245 – 254
28. Dinkelacker, A. Do tornado-like vortices play a role in turbulent mixing processes? 1982, Proc.IUTAM / ICHMT Symp.Dubrovnik / Ed. Z.P. Zaric-Washington, New York, London: Hemisphere Publuishing Co., pp.59-72.
29. Dinkelacker, A., Hessel, M., Meier, G., Schewe, G. Investigation of pressure fluctuations beneth a turbulent boundary layer by means of an optical method . 1977, *Phys. Fluids*, 20 (10), pt.2, pp.216-224.
30. Dutzler, G.K., Pettersson Reif, B.A., Andersson, H.I. Relaminarization of turbulent flow in the entrance region of a rapidly rotating channel, *Int. J. Heat Fluid Flow*, 2000, 21, pp. 49-57
31. Eckelmann, H. A review of knowledge on pressure fluctuations. Proc. Zoran Zaric Memorial International Seminar on Near Wall Turbulence, May 16-20, 1988, Dubrovnick, Yugoslavia, 21 p.
32. Falco, R.E. Coherent motions in the outer region of turbulent boundary layers. 1977, *Phys. Fluids*, 20 (10), pt.2, pp.124-132.
33. Fiedler, H.E. Coherent structures in turbulent flows . 1988, *Progress in Aerospace Science*, 25, pp.231-269.
34. Fiedler, H.E., Fernholz, H.-H. On management and control of turbulent shear flows . 1990, *Progress in Aerospace Science*, 27, pp.305-387.
35. Floryan, J. M. (1989) Goertler instability of boundary layers over concave and convex walls, *Phys. Fluids*, **29** (8), pp 2380-2387
36. Fucunishi, Y., Sato, H., Inoue, O. Study of developing process of coherent structures in the turbulent boundary layer. 1987, AIAA Pap. 87-1253.
37. Gad-el-Hak, M.Control of low-speed airfoil aerodynamics. 1990, *AIAA J.*, 28 (9), pp.1537-1552.
38. Gad-el-Hak, M. Interactive control of turbulent boundary layers: A futuristic overview. 1994, *AIAA J.*, 32 (9), pp.1753-1765.
39. Gad-el-Hak, M., Bushnell, D.M. Separation control: Review. 1991, *J. Fluid Engineering*, 113, pp.5-30.
40. Gallagher, J.A., Thomas, A.S.W. Turbulent boundary layer characteristics over streamwise grooves. 1984, AIAA Pap.84-2185.
41. Gatski, T.B. Drag characteristics of unsteady, perturbed boundary layer flows. 1985, AIAA Pap.85-0551.
42. Guezennec, Y.G., Nagib, H.M. Documentation of mechanisms leading to net drag reduction in manipulated turbulent boundary layers. 1985, AIAA Pap.85-0519.
43. Hagen, J.P., Kurosaka, M. Corewise cross-flow transport in hairpin vortices - The "tornado effect". 1993, *Phys. Fluids A*, 5 (12), pp.3167-3174.
44. Head, M.R., Bandyopadhyay, P. New aspects of turbulent boundary layer structure. 1981, *J. Fluid Mech*., 107, pp.297-338.
45. Iacovides, H., Launder, B. E. and Li H. Y., 'Application of a reflection-free DSM to turbulent flow and heat transfer in a square-sectioned U-bend', in *Experimental Thermal and Fluid Science*, 13, pp. 419-429, 1996
46. Jimenez, J., Moin, P. The minimal flow unit in near-wall turbulence. 1991, *J. Fluid Mech.*, 225, pp.213-240.
47. Johansen, J.B., Smith, C.R. The effects of cylindrical surface modifications on turbulent boundary layers. 1985, AIAA Pap.85-0547.
48. Jung, W.J., Mangiavacchi, N., Akhavan, R. Suppression of turbulence in wall-bounded flows by high-frequency spanwise oscillations. 1992, *Phys. Fluids A*, 4 (8), pp.1605-1607.
49. Kim, H.T., Kline, S.J., Reynolds, W.C. The production of turbulence near a smooth wall in a turbulent boundary layer. 1971, *J. Fluid Mech*., 50, pt.1, pp.133-160.
50. Kim, J. On the structure of wall-bounded turbulent flows . 1983, *Phys. Fluids.*, 26 (7), pp.2088-2097.

51. Kim, J. Turbulence structures associated with the bursting event. 1985, *Phys. Fluids*., 28 (1), pp.52-58.
52. Kinney, R.B., Taslim, M.E., Hung, S.C. Numerical study of large-eddy breakup and its effect on the drag characteristics of boundary layers. 1985, NASA CR-3884.
53. Kline, S.J., Reynolds, W.G., Schraub, F.A., Runstadler, P.W. The structure of turbulent boundary layers. 1967, *J. Fluid Mech.*, 30, pp.741-773.
54. Kral, L.D., Fasel, H.F. Numerical investigation of three-dimensional active control of boundary-layer transition. 1991, *AIAA J.*, 29 (9), 1407-1417
55. Kral, L.D., Fasel, H.F. Direct numerical simulation of passive control of three-dimensional phenomena in boundary-layer transition using wall heating. 1994, *JFM*, 264, 213-254
56. Kravchenko, A.G., Choi, H., Moin, P. On the relation of near-wall streamwise vortices to wall skin friction in turbulent boundary layers . 1993, *Phys. Fluids A* , 5 (12), pp.3307-3309.
57. Krogstad, P.-A., Antonia, R.A. Structure of turbulent boundary layers on smooth and rough walls. 1994, *J. Fluid Mech*., 277, pp.1-21.
58. Krogstad, P.-A., Antonia, R.A., Browne, L.W.B. Comparison between rough- and smooth-wall turbulent boundary layers . 1992, *J. Fluid Mech.*, 245, pp.599-617.
59. Laufer, J. New trends in experimental tyrbulence research. 1975, *Ann. Rev. Fluid Mech*., 7, pp.307-326.
60. Launder, B. E., 'Modelling the formation and dispersal of streamwise vortices in turbulent flow (the 35th Lanchester Lecture), *The Aeronautical Journal*, 1995, 99, pp 419-431
61. Launder, B. E., The modelling of turbulent flows with significant curvature or rotation effects, 1999. In: *Modeling Complex Turbulent Flows*, Kluwer, pp. 29 – 51
62. Luchik, T.S., Tiederman, W.G. Timescale and structure of ejections and bursts in turbulent channel flows. 1987, *J. Fluid Mech.*, 174, pp.529-552.
63. Luchik, T.S., Tiederman, W.G. Turbulent structure in low-concentration drag-reducing channel flows. 1988, *J. Fluid Mech.*, 190, pp.241-263.
64. Lumley, J.L. Drag reduction by additives. 1969, *Ann. Rev. Fluid Mech*., 1, pp.367-384.
65. Makita, H., Sassa, K., Abe, M., Itabashi, A. Decay process of a manipulated large-scale horseshoe vortex in a turbulent boundary layer . 1989, *AIAA J.*, 27 (2), pp.155-160.
66. McComb, W.D., Rabie, L.H. Local drag reduction due to injection of polymer solutions into turbulent flow in a pipe. 1982, AICHE J., 28, pp.547-565.
67. Mehta, R.D. Turbulent boundary layer perturbed by a screen. 1985, *AIAA J.*, 23 (9), pp.1335-1342.
68. Merkle, C.L., Deutsch, S. Drag reduction by microbubles: current research status. 1985, AIAA Pap. 85-0537.
69. Metzner, A.B. Polymer solution and fiber suspension rheology and their relationship to turbulent drag reduction. 1977, *Phys. Fluids.*, 20 (10), pt.2, pp.145-149.
70. Moser, R.D., Moin, P. The effects of curvature in wall-bounded turbulent flows. 1987, *J. Fluid Mech.*, 175, pp.479-510.
71. Nagano, Y., Tagawa, M. Coherent motions and heat transfer in a wall turbulent shear flow. *J. Fluid Mechanics*, 305, 127-157, 1995
72. Narasimha, R., Sreenivasan, K.R. Relaminarization of fluid flows. 1979, Adv. Appl. Mech., 19, pp.222-309.
73. Nikiforovich, E.I., Yurchenko, N.F. Boundary-layer flows with centrifugal forces. *ERCOFTAC Bulletin*, 1997, 32, pp. 61-65
74. Ohlendorf, D., Interthalm, W., Hoffmann, H. Surfactant systems for drag reduction: physico-chemical properties and rheological behavior. 1986, Rheol. Acta, 25, pp.468-486.
75. Praturi, A.K., Brodkey, R.S. A stereoscopic visual study of coherent structures in turbulent shear flow. 1978, *J. Fluid Mech.*, 89, pp.251-272.
76. Rabin, Y., Zielinska, B.J.A. Scale-dependent enhancement and damping of vorticity disturbances by polymers in elongational flow. 1989, *Phys. Rev. Lett.*, 63, pp.512-523.
77. Robinson, S.K. Coherent motions in the turbulent boundary layer. 1991, *Ann. Rev. Fluid Mech*., 23, pp.601-639.
78. Saric, W. S. Goertler vortices, 1994, *Annu. Rev. Fluid Mech*., **26**, 379-409
79. Savill, A.M., Mumford, J.C. Manipulation of turbulent boundary layers by outer-layer devices: skin-friction and flow-vizualization results. 1988, *J. Fluid Mech*., 191, pp.389-418.
80. Schwarz, W.R., Bradshaw, P. Measurements in a pressure-driven three-dimensional turbulent boundary layer during development and decay . 1993, *AIAA J*., 31 (7), pp.1207-1214.
81. Simon, T.W., Moffat, R.J., Johnston, J.P., Kays, W.M. Turbulent boundary layers heat transfer experiments: Convex curvature effects including introduction and recovery. 1980, Rep. HMT-32, Stanford Univ.
82. Smith, C.R. Vizualization of turbulent boundary layer structure using a moving hydrogen bubble wire probe. 1978, Lehigh Workshop on Coherent structure in turbulent boundary layers / Ed. C.R. Smith, D.E. Abbott. , pp.48-97.

83. Suzuki, Y., Kasagi, N. Turbulent drag reduction mechanism above a riblet surface. 1994, *AIAA J.*, 32 (9), pp.1781-1790.
84. Tani, I. Production of longitudinal vortices in the boundary layer along a concave wall. *J. Geophys. Research*, 1962, 17, No. 8, pp. 3075-3088
85. Tiederman, W.G., Luchik, T.S., Bogard, D.G. Wall-layer structure and drag reduction. 1985, *J. Fluid Mech.*, 156, pp.419-437.
86. W.Thomas, A.S., Bull, M.K. On the role of wall-pressure fluctuations in deterministic motions in the turbulent boundary layer. 1983, *Phys. Fluids.*, 128, pp.283-322.
87. Voropaev, G.A. Numerical simulation of a turbulent boundary layer an unfavourable pressure gradient. *Bionics*. 1998. 27-28, pp. 25-37 (in Russian)
88. Voropaev, G. A., Rozumnyuk, N. V. Numerical simulation of a turbulent flow over a deformable surface. *Applied Hydromechanics*. 2000, vol. 2(74), 2, pp. 23-34 (in Russian)
89. Vucoslavcevic, J.M., Wallace, J.M., Balint, J.-L. Viscous drag reduction using streamwise-aligned riblets. 1992, AIAA J., 30 (4), pp.1119-1122.
90. Walker, D.T., Tiederman, W.G. Turbulent structure in a channel flow with polymer injection at the wall. 1990, *J.Fluid Mech*., 218, pp.377-403.
91. Walker, D.T., Tiederman, W.G., Luchik, T.S. Optimization of the injection process for drag reducing additives. 1986, *Exp. Fluids*, 4, pp.114-120.
92. Walker, J.D.A., Abbott, D.E., Scharnhorst, R.K., Weigand, G.G. Wall-layer model for the velocity profile in turbulent flows. 1989, *AIAA J.*, 27 (2), pp.140-149.
93. Walsh, M.J. Turbulent boundary layer drag reduction using riblets . 1982, AIAA Pap. №82-0169.
94. Walsh, M.J., Lindemann, A.M. Optimisation and aplication of riblets for turbulent drag reduction. 1984, AIAA Pap. №84-0347.
95. Wark, C.E., Naguib, A.M., Nagib, H.M. Effect of plate manipulators on coherent structures in a turbulent boundary layer. 1990, *AIAA J.*, 28 (11), pp.1877-1884.
96. Wei, T., Willmarth, W.W. Modifying turbulent structure with drag-reducing polymer additives in turbulent channel flows. 1992, *J. Fluid Mech.*, 245, pp.619-641.
97. Wei, T., Willmarth, W.W. Reynolds-number effects on the structure of a turbulent channel flow. 1989, *J. Fluid Mech.*, 204, pp.57-95.
98. Wendt, B.J., Greber, I., Hingst, W.R. Structure and development of streamwise vortex arrays embedded in a turbulent boundary layer. 1993, *AIAA J.*, 31 (2), pp.319-325.
99. Wilkinson, S.P. The influence of wall permeability on turbulent boundary layer properties. 1983, AIAA Pap. 83-0294.
100. Wilkinson, S.P., Anders, J.B., Lazos, B.S., Bushnell, Turbulent drag reduction research at NASA Langley: Progress and Plans. 1988, International Journal of Heat and Fluid Flow, 9, pp.266-277.
101. Willmarth, W.W., Bogar, T.J. Survey and new measurement of turbulent structure near the wall. 1977, *Phys. Fluids.*, 20 (10), pt.2, pp.9-21.
102. Willmarth, W.W., Sharma, L.K. Study of turbulent structure with hot wires smaller than the viscous length. 1984, *J. Fluid Mech.*,142, pp.121-149.
103. Yurchenko, N. Receptivity of boundary layers under centrifugal forces, 2000, *Proc. 8th European Turbulence Conference, Barcelona , Spain, June 27-30, 2000, pp. 479-482*
104. Yurchenko, N.F. Optimization of heat transfer control based on a receptivity approach, 1998, *Proc. Turbulent Heat Transfer Conference, Manchester, UK, P72-P81*
105. Yurchenko, N.F., Delfs, J.W., Boundary layer control over an active ribleted surface, 1999. In: *Fluid Mecanics and its Applications*, Vol.53, 217-222, Kluwer, eds. G.E.A.Meier and P.R.Viswanath
106. Yurchenko, N.F., Zygmantas, G.P. Generation of longitudinal vortices in boundary layers affected by body forces. *Engineering-Physical J.*, 1989, 57, 3, pp. 392-398 (in Russian)
107. Yurchenko, N., Rivir, R. Optimization of a turbine blade performance due to active control of vortex dynamics, Proceedings NATO/RTO Active Control Symposium, Braunschweig, Germany, 2000, 8-12 May.
108. Yurchenko, N.F., Rivir, R.B. Flow management using inherent transition and receptivity features, 1998, Proc. International Symposium on Seawater Drag Reduction, Newport, USA
109. Y.H.Zurigat, A.H.Nayfeh, J.A.Masad, Effect of pressure gradient on the stability of compressible boundary layers 1992, AIAA J., 30 (9), pp.2204-2211.

7. NUMERICAL SIMULATION OF TRANSITIONAL BOUNDARY-LAYER FLOWS UNDER THERMAL CONTROL

7.1. Introduction: Effects of generated streamwise vortices on the topology of transitional boundary layers over concave surfaces.

Numerous engineering applications require the solution of the flow control problem, which typically relates to the wall-bounded flows like boundary layers or channels. Besides, these flows of interest appear to be both laminar, transitional and turbulent depending on a certain application. However in any case, this problem naturally reduces to the capability to maintain a favorable vortical structure. Thus its optimal and efficient solution requires first of all clear understanding of the vortex dynamics of flows under consideration; in the present studies, they are the flows under centrifugal forces. Analyzing streamwise vortices intrinsic to such flows, i.e. boundary layers evolving along concave walls, one can pick out advantageous stages of their evolution to modify and maintain the motion scale and intensity in a given range of Reynolds numbers.

To harmonize the developed approach, the first part of the investigation was carried out for laminar/transitional boundary layers according to the Contract F61775-98-WE123. Spectral method was applied for a finite number of harmonics to investigate natural and forced development of streamwise vortices over a concave surface. A constant boundary condition was taken in a form of a temperature varying periodically along a spanwise direction over the surface (a method of flush-mounted heated strips as described in the final report on the mentioned Contract).

The studies were based on the Goertler instability theory and receptivity approach using the numerical code developed for the direct numerical simulation of a laminar-turbulent transition in compressible subsonic boundary layers. It allowed to obtain amplitude and frequency characteristics for each of 12 considered harmonics as time functions for fixed Reynolds and Goertler numbers. The fundamental in the spanwise direction was taken to be $\Lambda=\lambda_z^{3/2}U_0\nu^{-1}R^{-1/2}=236$, i.e. corresponding to the region of most amplified nondimensional wavelengths according to the Goertler diagram. The second mode, $\Lambda=84$, stayed in the domain of amplified wavelengths, while all the other ten numerically considered harmonics were linearly damped. As described in the mentioned above Contract reports, 3 cases of vortical system evolution were analyzed:

(0) Reference case – natural evolution during laminar-turbulent transition;

(1) Case 1 – vortices initiated thermally (spanwise temperature gradient, $\Delta T=30°$ K) with the regular excitation of the second Goertler mode, $\Lambda 2=84$;

(2) Case 2 – vortices generated under slightly irregular excitation of the second mode that made other harmonics available.

It has been shown that the spanwise periodicity of the surface temperature variation $\Delta T(z)$ corresponding to the second Goertler mode (Case 1) induced the initial vortical structure with a scale smaller than the „reference“ one. However later it transformed into a larger one to correspond to the most amplified first mode. Case 2 where the generated and intended to dominate second mode admitted the appearance of other modes showed an immediate grasp and further development of the first mode thus having displayed the enlargement of the vortical structure. In both cases, the constant boundary condition imposing the permanent preference to a given vortex scale could not prevent from developing and final dominance of a larger scale vortical structure. However in Case 1, the flow structure transformation took a longer time, while in Case 2, the initially strongly prevailed second mode gave up in favor of the first one. Both controlled cases demondtrated longer lifetime of streamwise vortices that was extended by 29-47% compared to the „reference“, natural evolution case.

7.2. Skin friction in a transitional boundary layer with embedded streamwise vortices; long-term effects

To extend transitional boundary-layer investigations to the turbulent case with a focus on integral flow characteristics, long-term effects and skin friction were calculated for transitional flows in

presence of thermally generated streamwise vortices. DNS of subsonic boundary layers over a concave surface was carried out in the framework of the Goertler approach (i.e. taking into account a centrifugal force) under a boundary condition in a form of temperature varying periodically along a span. The free-stream Mach number was $M=0.8$, the free-stream temperature was $T_o=290\ K$; the Goertler number based on the momentum thickness ϑ was $G_\vartheta=8$. As earlier, there were considered a reference Case 1 of the natural laminar-turbulent transition and 2 controlled cases where streamwise vortices were generated in accordance with a purely second Goertler mode, $\Lambda=84$, (Case 2) and with "imperfect" generation of the second mode that allowed presence of all other modes including the most amplified first mode, $\Lambda=236$, (Case 3). Fig. 7.2.1 illustrates skin friction results for these cases.

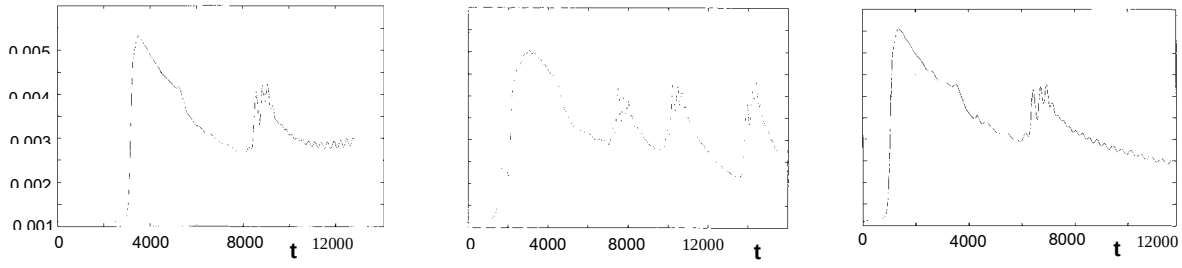

Reference Case: no control (natural development of streamwise vortices)

Case1: Excitation of vortices corresponding to the purely second Goertler mode

Case 2: Excitation of the second Goertler mode including other modes.

Fig. 7.2.1. Friction drag coefficients calculated for the latest stage of the laminar-turbulent transition in a boundary layer over a concave surface controlled by heated flush-mounted longitudinal strip

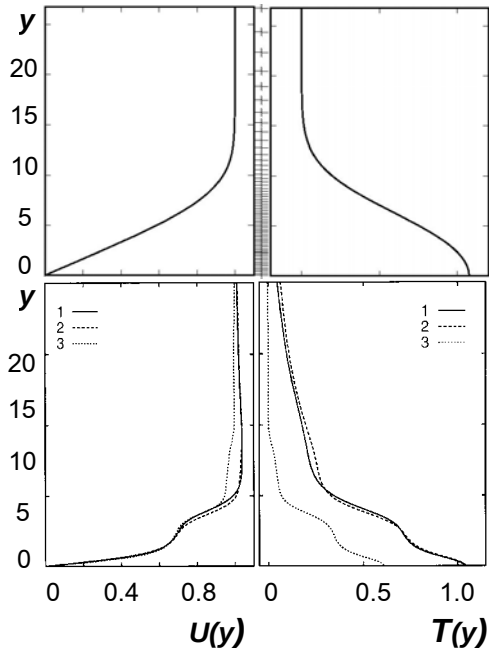

Fig. 7.2.2.

These estimations of skin friction coefficients $C_f(t)$ can be interpreted in terms of the vortical structure of a near-wall flow. The obtained results analyzed together with the earlier obtained data on flow topology and amplitude functions correlated with C_f values depending on time can bring to the following conclusions:

1. There is a certain time interval characterized by an exponential growth of main boundary-layer quantities even under conditions of sufficiently large initial amplitudes;
2. Each mode comes to a saturation level corresponding to the scale of streamwise vortices; further growth and drift of these vortices upward from the surface results in their breakdown;
3. The breakdown of the vortical system is followed by the formation of a secondary structure that can only remind the previous one since the vortices are set in a chess order and their axes are not streamwise oriented. The secondary vortices have a lifetime characterized by a group frequency of about 10 Hz which defines the C_f oscillations.
4. Generation of streamwise vortices corresponding to the second mode (Case 1) displays a time interval where these vortices prevail; accordingly, the skin friction peak appears to be lower and smoothed compared to the reference case, periodicity of the bursting events can be regulated.

Long-term effects (for $t>8000$) of the periodic $\Delta T(z)$ thermal boundary condition were shown (Fig. 7.2.2) for mean velocity and temperature profiles $U(y)$ and $T(y)$ averaged in the spanwise direction.

All three cases of vortical structure formation were considered. Indicative for this late stage is the fact that further changes to the profiles remain small. It is seen that there is a remarkable change in the thermally controlled velocity- and temperature profiles compared to the unforced case. While the overall change in profile shapes must be due to an effect of the mean heat added to the flow, the differences of the mean profiles between cases 1 and 2 still remain characteristic. Besides, the long-term effect of the different regimes of wall heating was observed mainly in an upper region of a boundary layer, e.g. at $3<y<5$ for the velocity profiles.

8. NUMERICAL SIMULATION OF NEAR-WALL FLOWS USING THE DEVELOPED TURBULENCE MODEL TAKING ACCOUNT OF LARGE-SCALE VORTICES INDUCED BY THE THERMAL BOUNDARY CONDITION

8.1. Calculations of characteristics of viscous compressible flows over curved surfaces with the spanwise-regular heating. Feasibility of the turbulent flow-control approach and the developed turbulence model.

Three-dimensional (3D) secondary structures can develop in the near-wall gradient flow initiated both by external disturbances and arising as a result of the nonstationary interaction of inherent disturbances. The eigen-type disturbances may form either organized secondary structures or display themselves as a random turbulent motion. In some cases, random background oscillations of the flow parameters around its averaged values enable to observe deterministic vortical structures with specific time and space scales. Its formation, development and lifetime depend on a number of factors, therefore they are not easily detectable under natural conditions. But introducing though small controlled disturbances into the flow, one can register coherent structures. The thermal control under consideration is just the approach creating such a flow situation.

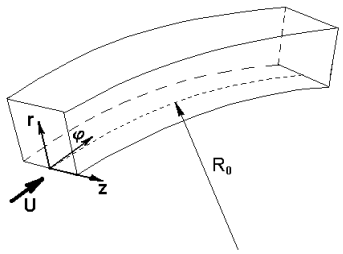

Fig. 8.1.1. Computational flow domain for turbulence modeling

Secondary flows over convex or concave surfaces were investigated numerically for a 3D compressible flow (see flow domain in Fig. 8.1.1) under the spanwise-regular surface heating. The airflow has been analyzed at a free-stream velocity U_0=10m/s over a curved surface of a constant radius (R_0=0.2m and 0.8m), spacing between longitudinal heated elements having been h_i=0.0025m (equivalent to λ_z used in the experimental notation), dynamic viscosity depending on temperature. The computations have been carried out for all considered in experiments types of the flow geometry under the uniform constant temperature T=293 K° of the domain (a reference case), and for the case of a spanwise-regular heated grid (flush-mounted longitudinal heated elements) typically with T=328 K° but actually, looking for an effect in a range of temperature gradients, ΔT=15°-70°.

Basic, although incomplete, variety of flow conditions analyzed in the numerical simulation is shown in the Table below:

S=0.2m	R=0.2m	U=10m/s	convex	laminar	T=const ΔT=15°C, λ_z=0.0025m ΔT=25°C, λ_z=0.0025m ΔT=35°C, λ_z=0.0025m
S=0.2m	R=0.2m	U=10m/s	concave	laminar	T=const ΔT=35°C, λ_z=0.0025m
S=0.2m	R=0.8m	U=10m/s	convex	laminar	T=const ΔT=35°C, λ_z=0.0025m
S=0.2m	R=0.8m	U=10m/s	concave	laminar	T=const ΔT=35°C, λ_z=0.0025m
S=0.2m	R=0.8m	U=20m/s	convex	laminar	T=const ΔT=35°C, λ_z=0.0025m ΔT=35°C, λ_z=0.005m

S=0.2m	R=0.8m	U=20m/s	concave	laminar	T=const $\Delta T=35°C$, $\lambda_z=0.0025m$ $\Delta T=35°C$, $\lambda_z=0.005m$
S=0.2m	R=0.8m	U=20m/s	plane	laminar	T=const $\Delta T=35°C$, $\lambda_z=0.0025m$ $\Delta T=35°C$, $\lambda_z=0.005m$
S=0.2m	R=0.2m	U=20m/s	convex	laminar	T=const $\Delta T=35°C$, $\lambda_z=0.0025m$ $\Delta T=35°C$, $\lambda_z=0.005m$
S=0.2m	R=0.2m	U=20m/s	concave	laminar	T=const $\Delta T=35°C$, $\lambda_z=0.0025m$ $\Delta T=35°C$, $\lambda_z=0.005m$
S=0.2m	R=0.3m	U=20m/s	concave	laminar	T=const
S=0.2m	R=0.2m	U=15m/s	concave	laminar	T=const $\Delta T=35°C$, $\lambda_z=0.0025m$ $\Delta T=35°C$, $\lambda_z=0.005m$
S=0.2m	R=0.2m	U=19.5m/s	concave	laminar	T=const
S=0.2m	R=0.2m	U=20.5m/s	concave	laminar	T=const
S=0.2m	R=0.2m	U=45m/s	concave	laminar	T=const
S=0.2m	R=0.2m	U=45m/s	concave	turbulent	T=const
S=0.2m	R=0.2m	U=20.5m/s	concave	turbulent	T=const $\Delta T=35°C$, $\lambda_z=0.0025m$ $\Delta T=35°C$, $\lambda_z=0.005m$
S=0.3m	R=0.2m	U=15m/s	concave	laminar	T=const
S=0.3m	R=0.2m	U=19.5m/s	concave	laminar	T=const
S=0.3m	R=0.2m	U=20m/s	concave	laminar	T=const
S=0.3m	R=0.2m	U=25m/s	concave	laminar	T=const $\Delta T=35°C$, $\lambda_z=0.0025m$ $\Delta T=35°C$, $\lambda_z=0.005m$
S=0.3m	R=0.2m	U=27m/s	concave	laminar	T=const
S=0.3m	R=0.2m	U=28m/s	concave	laminar	T=const
S=0.3m	R=0.2m	U=29m/s	concave	laminar	T=const
S=0.3m	R=0.2m	U=29.5m/s	concave	laminar	T=const
S=0.3m	R=0.2m	U=20m/s	concave	laminar	T=const
S=0.3m	R=0.2m	U=32m/s	concave	laminar	T=const
S=0.3m	R=0.2m	U=34m/s	concave	laminar	T=const $\Delta T=35°C$, $\lambda_z=0.0025m$ $\Delta T=35°C$, $\lambda_z=0.005m$
S=0.3m	R=0.2m	U=34.1m/s	concave	laminar	T=const
S=0.3m	R=0.2m	U=34.15m/s	concave	laminar	T=const
S=0.3m	R=0.2m	U=34.2m/s	concave	laminar	T=const
S=0.3m	R=0.2m	U=34.25m/s	concave	laminar	T=cons t

S=0.3m	R=0.2m	U=34.5m/s	concave	laminar	T=const
S=0.3m	R=0.2m	U=35m/s	concave	laminar	T=const
S=0.3m	R=0.2m	U=25m/s	concave	turbulent	T=const
S=0.3m	R=0.2m	U=30m/s	concave	turbulent	T=const $\Delta T=50°C$, $\lambda_z=0.005m$ $\Delta T=70°C$, $\lambda_z=0.005m$
S=0.3m	R=0.2m	U=34.2m/s	concave	turbulent	T=const $\Delta T=50°C$, $\lambda_z=0.0025m$ $\Delta T=50°C$, $\lambda_z=0.005m$ $\Delta T=70°C$, $\lambda_z=0.005m$
S=0.3m	R=0.2m	U=34.5m/s	concave	turbulent	T=const
S=0.3m	R=0.2m	U=40m/s	concave	turbulent	T=const

First of all, **reference cases** have been considered of the flows naturally developing along concave and convex surfaces under different basic flow parameters matched with those used in experiments.

It was found that boundary layers both on convex and concave surfaces had no noticeable evidence of three-dimensionality. All parameters of the flow did not depend on the spanwise coordinate *Z*, and no secondary longitudinal vortical structure was observed. Spanwise velocity component V_z was close to zero. Spanwise velocity V_z over a convex surface was also very small, randomly distributed along *Z*.

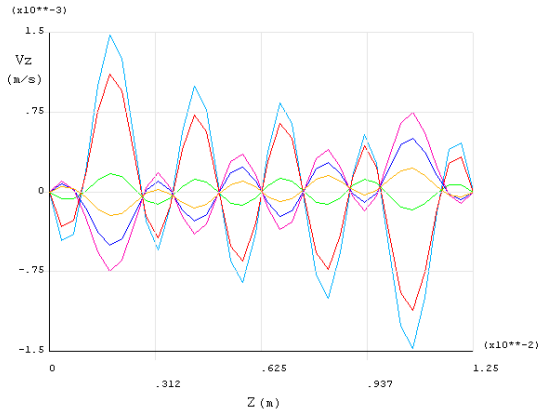

Fig. 8.1.2. Spanwise velocity distributions at a different distance from a surface:
blue – 0.094δ, red – 0.19δ, green –0.28δ, dark blue – 0.38δ, purple – 0.49δ, yellow – δ, where δ is a boundary layer thickness.

However in the controlled case, the periodicity can be seen of the flow parameters along *Z* followed by the spacing between the streamwise heated elements. Figure 8.1.2 shows V_z velocity components (V_{fi} is a longitudinal component, V_r is a normal component) at different distances from the wall.

Similar results have been obtained for other velocity components, temperature and dynamic viscosity over concave and convex surfaces (R_0=0.2 m and 0.8 m). Flow was found to decelerate over the heated elements, velocity V_{fi} having been lower compared to that of the reference case, and higher between elements. Normal component V_r is much lower though not negative above the elements. However subtracting mean normal boundary-layer displacement velocity, negative normal velocities appear in the secondary flow. The component V_z is zero above the elements and in the middle between them, and reaches maximum at a distance of $1/4h_i$ from the elements.

Thus one can conclude that a pair of secondary counter-rotating vortices appears between two adjacent elements, i.e. those with opposite vorticity. In addition, calculations showed increased friction drag over the surface with heated elements.

Flow field patterns over a convex surface were similar (see Fig. 8.1.3), but the intensity of the secondary flow was much lower. Except normal pressure gradient, mean flow was also similar over the both surfaces with opposite curvature signs. Computations revealed another set of vortex pairs

above the near-wall layer of vortices however with their intensity essentially lower and the shape stretched normally to the surface.

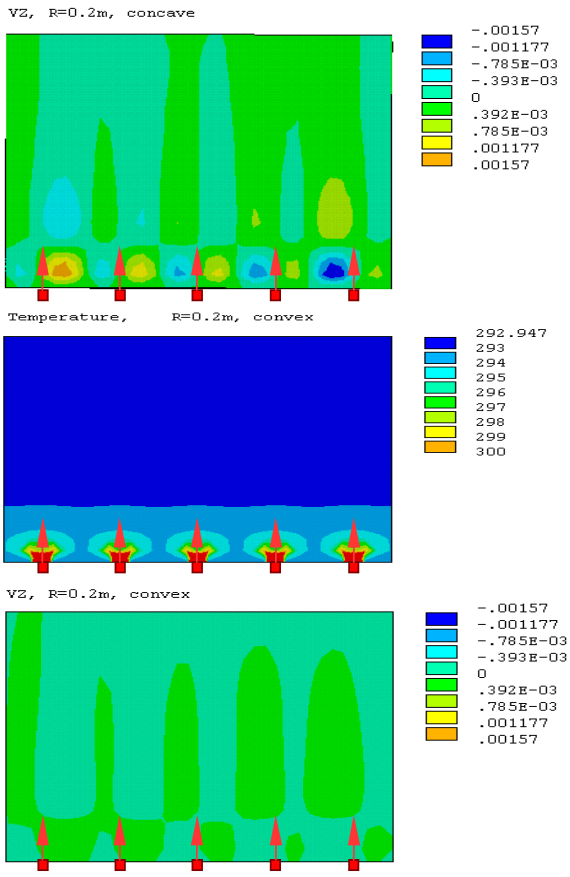

Fig. 8.1.3. Velocity (Vz) and temperature field patterns over the thermally controlled concave and convex surfaces

Thus first numerical data based on the developed turbulence model showed its capacity and prospects to solve the formulated boundary-layer control problem. The obtained results proved the feasibility of the secondary vortical structure generation over surfaces of various curvature using the spanwise-regular wall temperature distribution. Intensity and scales of the vortices depend on temperature and spacing of heated longitudinal elements.

However intensity of these vortices was found to be weak for both convex and concave surfaces. Therefore further computations have been carried out at higher values of a free-stream velocity, U_0=15m/s and 20m/s, and the same values of the surface curvature and the control factor.

For the higher free-stream velocity, a boundary layer over a concave surface with a uniform constant temperature showed the formation of 3D structures with greater intensity. Boundary layer over a convex surface displayed no noticeable vortical structures.

The temperature boundary condition for flow control was realized as heating to T=328 K° of regular longitudinal strips (i.e. 35° above the ambient flow) which resulted in modification of flow patterns both over concave and convex surfaces. Induced regular vortices were registered in both cases, their intensity having been one order higher over a concave surface. The vortices were flattened in a normal to the surface direction over a convex wall, while having stayed slightly elongated over a concave wall.

Figures 8.1.4 – 8.1.7 show effects of different spacing, λ_z=2.5 mm and 5 mm, between heated elements corresponding to the scale of streamwise vortices generated at U_0=15m/s over a concave surface. Vortices of a larger scale are more intense; a narrower spacing, lower intensity of vortices was observed. Amplitudes of all fluctuating velocity components are comparable to their local mean values in a reference case. Color lines correspond to different distances from the surface as follows:

blue – 0.094δ, red – 0.38δ, green – 0.49δ, dark blue – 0.7δ, purple – δ, orange – 1.2δ.

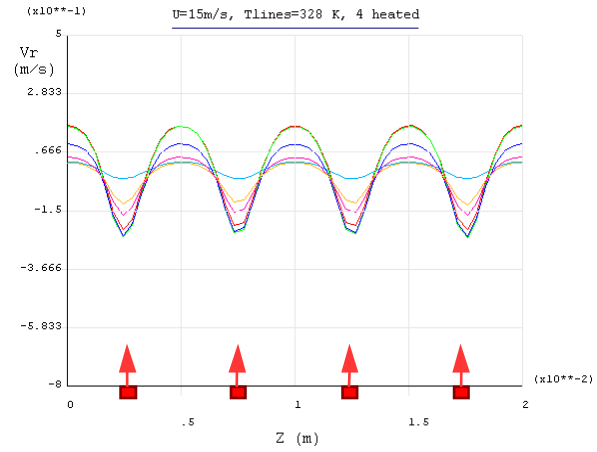

Fig. 8.1.4

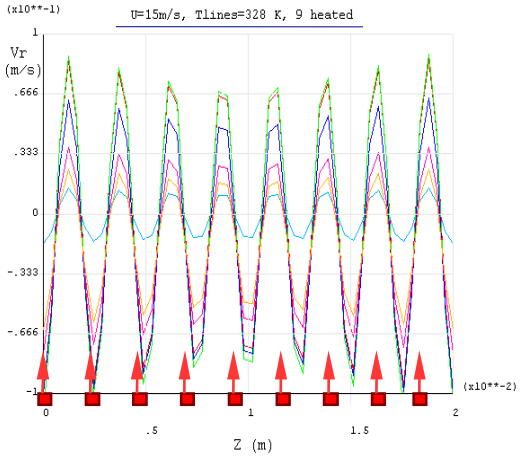

Fig. 8.1.5

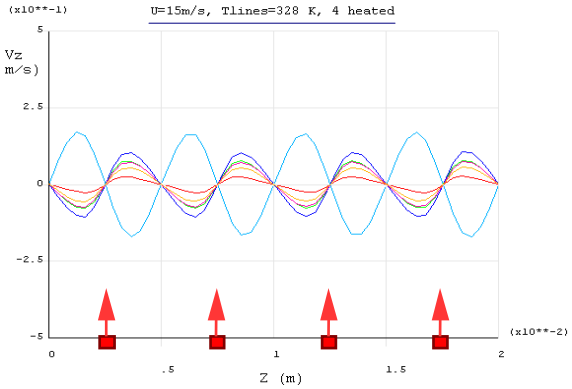

Fig. 8.1.6

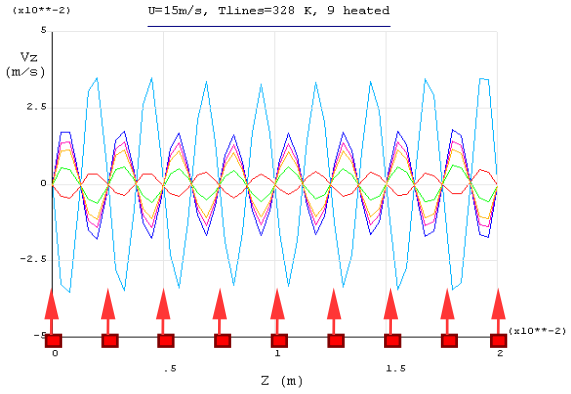

Fig. 8.1.7

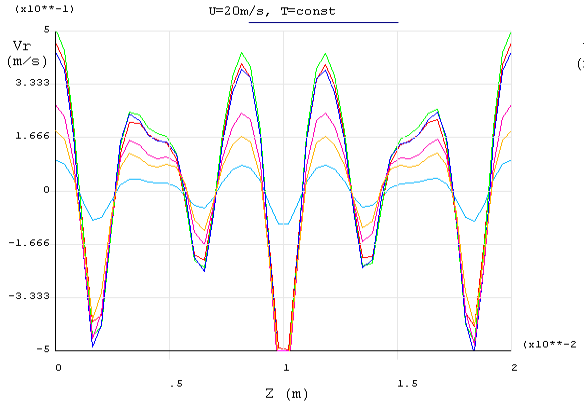

Fig. 8.1.8

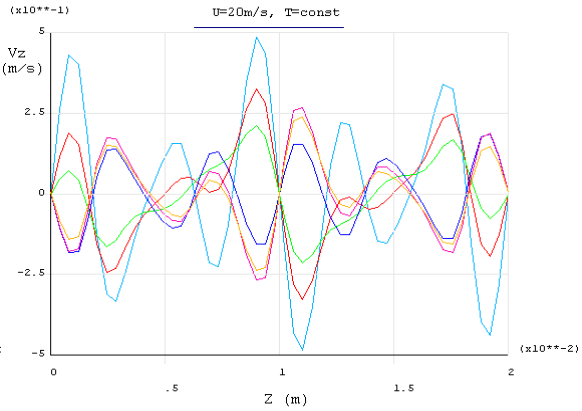

Fig. 8.1.9

At a higher free-stream velocity, U_0=20m/s, naturally developing vortices (reference case) appear to be so strong (Figs. 8.1.8, 8.1.9) that the same control heating to T=328 K° had a much less effect on the flow patterns.

The secondary streamwise vorticity in boundary layers over flat and convex walls was shown to develop only under the imposed ΔT_z boundary condition. Under this condition, intensity of the streamwise vorticity is several times higher over the convex surface compared to the flat one. It can be considered as a possibility to apply the developed boundary-layer control method to surfaces of different curvature, e.g. in cases where flow separation control is necessary.

Besides, the greater were values of the free-stream velocity, surface curvature and a distance between the heated elements (z-scale of generated vortices), the higher was the intensity of streamwise vorticity. However the vorticity intensity decreased downstream and vortex axes moved upward.

Figs. 8.1.10 – 8.1.20 illustrate these conclusions based on the comparative analysis of the vortical structure calculated for different streamwise positions, s=0.13 and 0.19m, for flat, convex and concave surfaces as well as for 2 scales λ_z of thermally generated vortices. Blue and green iso-vorticity lines correspond to its different signs.

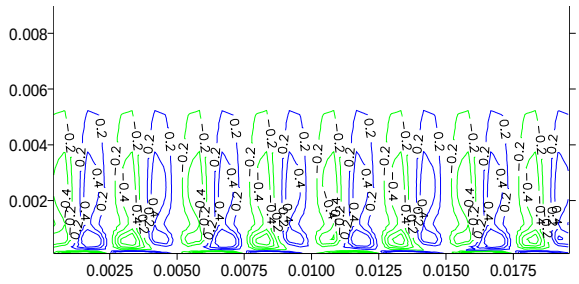

Fig. 8.1.10. λz=0.0025m, s=0.13

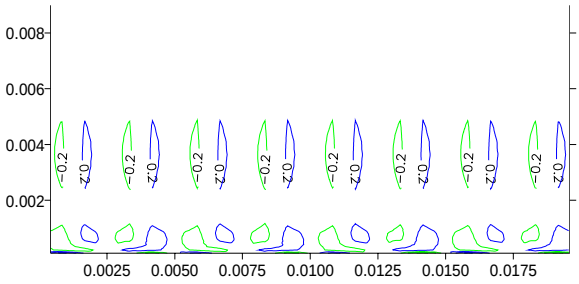

Fig. 8.1.11. λz=0.005m, s=0.19

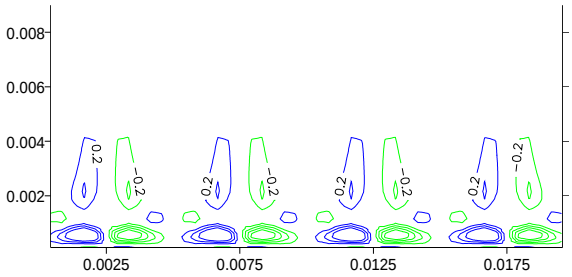

Fig. 8.1.12. λz=0.005m, s=0.13

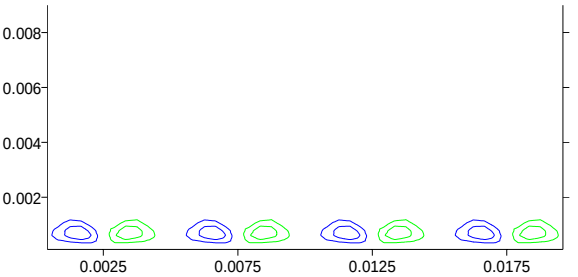

Fig. 8.1.13. λz=0.0025m, s=0.19

Figs. 8.1.10-8.1.13. Development of streamwise vortices over the flat-plate under the thermal control imposed as ΔTz=350C

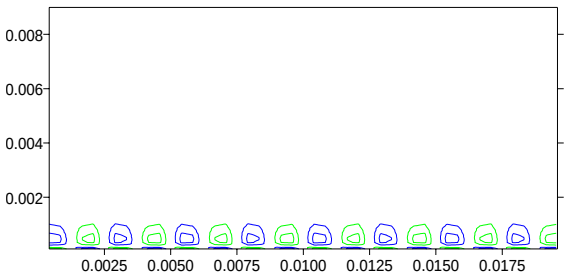

Fig. 8.1.14. ΔTz=350C, λz=0.0025m, s=0.13

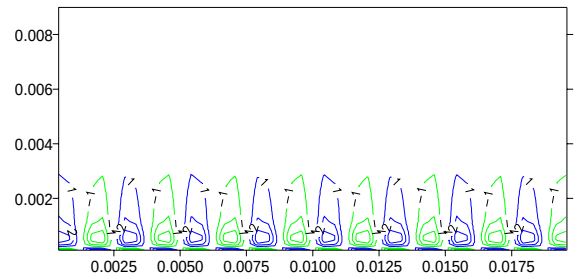

Fig. 8.1.15. ΔTz=350C, λz=0.0025m, s=0.19

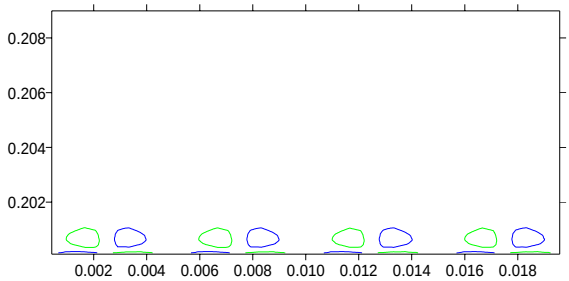

Fig. 8.1.16. $\Delta T_z=35^0C$, λ_z=0.005m, s=0.13

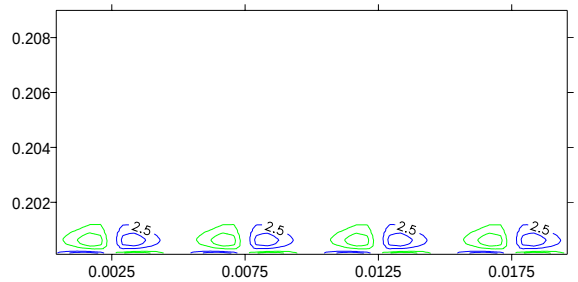

Fig. 8.1.17. $\Delta T_z=35^0C$, λ_z=0.005m, s=0.19

Figs. 8.1.14-8.1.17. Boundary layer over a **convex surface** under the thermal control

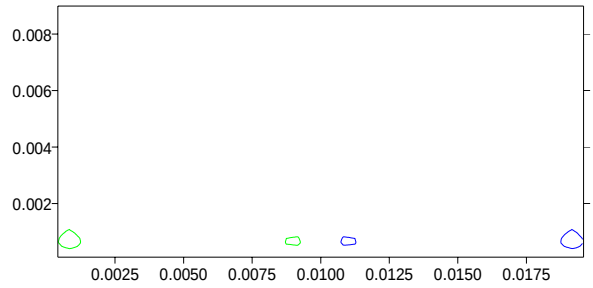

Fig. 8.1.18, a. T=0, s=0.13

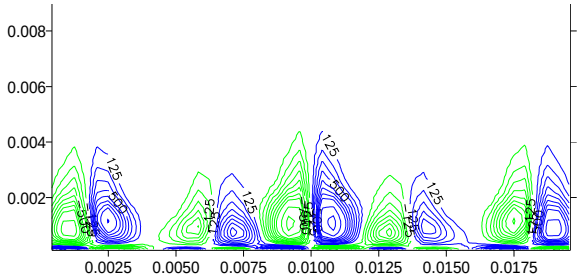

Fig. 8.1.18, b. T=0, s=0.19

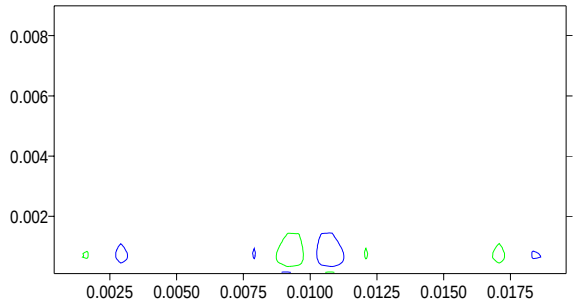

Fig. 8.1.19, a. $\Delta T_z=35^0C$, $\lambda_z=0.0025m$, s=0.13

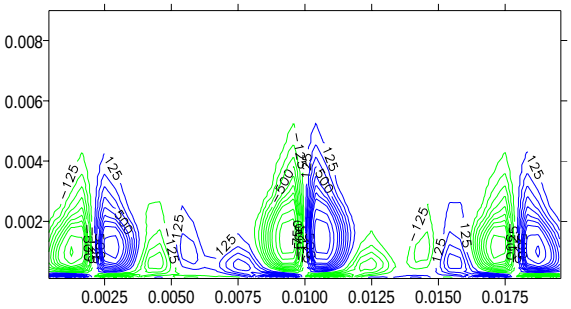

Fig. 8.1.19, b. $\Delta T_z=35^0C$, $\lambda_z=0.0025m$, s=0.19

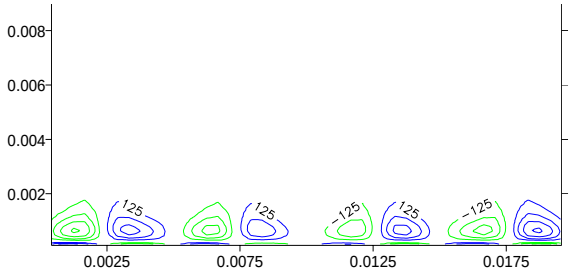

Fig. 8.1.20, a. $\Delta T_z=35^0C$, $\lambda_z=0.005m$, s=0.13

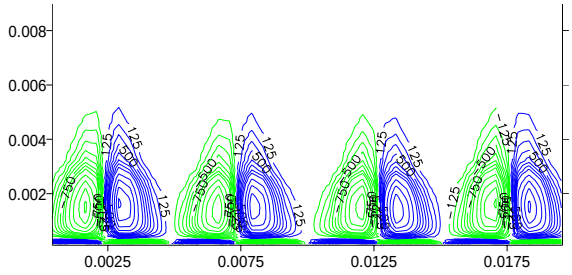

Fig. 8.1.20, b. $\Delta T_z=35^0C$, $\lambda_z=0.005m$, s=0.19

Figs. 8.1.18-8.1.20. Boundary layer over a **concave surface** under the thermal control;

(a), (b) show the downstream development of the generated vortical structure

Thus the results of numerical simulation of the vortical structure given by kinematical flow characteristics proved that the ΔT_z temperature gradient imposed on a concave surface can be used as an effective control factor stimulating the development and maintenance of regular vortex pairs. Changing the vortex z-scale, one can control the intensity of fluid motion and its downstream growth in a boundary layer. Similar local effects under the similar thermal excitation were observed in case of the convex surface but only in the vicinity of the wall.

8.2. Computational consistency

Earlier made computations (1) related to boundary layers controlled with streamwise vortices were based on the DNS code for modeling of the laminar-turbulent transition in compressible subsonic flows over concave walls, i.e. with body force terms included into the Navier-Stokes equations. Present, second stage (2) of numerical simulation is based on the 3D Reynolds stress transport model of a 3D near-wall turbulent flow of nonisothermal viscous compressible fluid. In both cases, streamwise vortices were generated using a constant boundary condition in a form of *z*-periodic wall temperature *T(z)* which can be adequately realized both numerically and experimentally.

Two columns of figures below show that the results obtained in two independent sets of numerical simulation are in a good agreement thus describing the true physical process of the forcedly developing vortical structure in boundary layers.

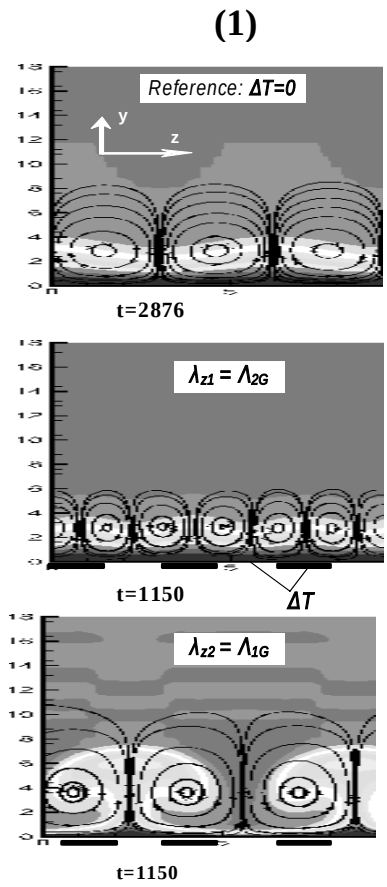

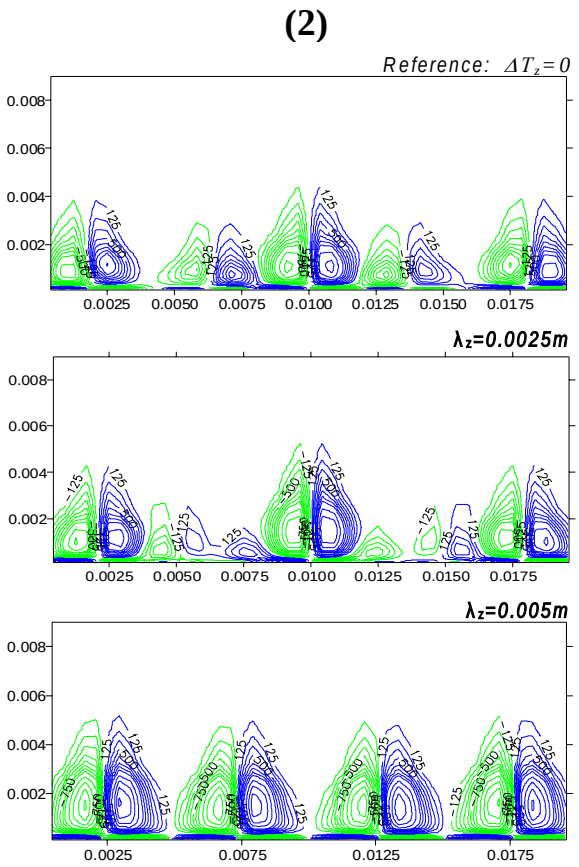

Fig. 8.2.1. G=8; $\Delta T_z=30^0$K, $\lambda_{z2} \approx \lambda_{z1}$

Fig. 8.2.2. Re=$5\cdot10^5$; $\Delta T_z=35^0$C, s=0.19

(1) Figure 8.2.1 refers to the laminar-turbulent transition approach demonstrating natural (top pattern) development of vortices in time as well as in cases of streamwise vortices generated with a spectrum of scales including the λz1 corresponding to the "Goertler fundamental" in the spanwise direction Λ1G=λg3/2U0ν-1R-1/2=236, and with a purely second mode λz2 according to the Goertler diagram. The second mode, Λ2=84, stayed in the domain of amplified wavelengths, while all the other ten numerically considered harmonics were linearly damped.

(2) Figure 8.2.2 gives the results of turbulence modeling: downstream development of streamwise vortices over a concave surface in an uncontrolled case (top) and under the imposed ΔT(z) temperature boundary condition with twice differing spanwise scale of generated vortices like in the (1) set.

Both approaches show that under similar basic flow parameters, the flow displays an evident preference to maintain the larger scale vortices, i.e. those which are naturally dominating in the flow. Generation of half-wavelength vortices results in their transformation into a larger structures in time or in space. It is also illustrated with Figure 8.2.3 of the combined numerical (based on the Goertler theory) and experimental results (the latter obtained for $Re_x=0.6\cdot10^5$, R=12 m, λ_z=1.2 cm; y_{low}=0.1 cm, Δy=0.3 cm): weak influence of the $\Delta T(z)$ control factor maintains a small-scale vortical structure in the vicinity of the surface while being unable to restructure the whole thickness of the boundary layer.

Thus the developed 3D Reynolds stress transport model compared with the well known Goertler instability approach, proved to be well applicable to consider problems of boundary-layer thermal control. In addition to revealing important flow features and physical mechanisms, it enables the analysis of fully turbulent flows. The localized influence of the developed flow control method and the nature of flow development can probably optimize integral characteristics of the flow around an airfoil-type body: decrease drag coefficients owing to the control over shear stress components related

to smaller scale motion near the surface, $-\overline{u'v'}$ and $-\overline{u'w'}$, and simultaneously increase lift coefficients due to large vortices in the outer region intensifying mixing and delaying the flow separation.

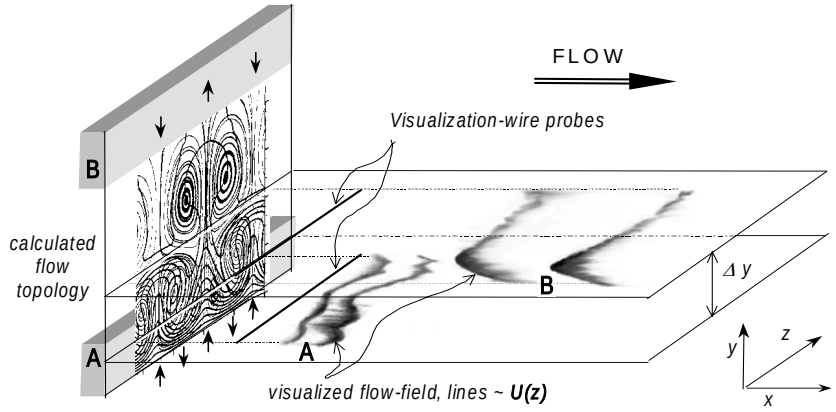

Fig. 8.2.3. Transformation of a small-scale **A** vortical structure near a wall into larger scale **B** vortices in the outer region of a boundary layer: calculations (left) and experiment (right)

8.3. Characteristics of curved laminar and turbulent boundary layers with vortical structures developing under thermal ΔT_z excitation

A particular feature of boundary layers under body forces to support natural development of streamwise vortices was shown to be advantageous for efficient control of transition to turbulence. In addition, it was found that long downstream the transition area, turbulent boundary layers retained scales and frequencies of 3D vortical structures typical for the laminar-turbulent transition. This fact of the flow memory was assumed here as a basis to control turbulent boundary layers using the same approach, i.e. distributed forcing from the wall due to surface temperature regularly varying in a spanwise direction. Such organized forcing created conditions for the turbulent boundary layer relaminarization owing to reduced intensity of stochastic disturbances in the flow.

Thus the present part of the work deals with the analysis and comparison of the laminar and turbulent boundary-layer structure of flows over curved surfaces. It is based on the detailed results of numerical simulation verified with wind-tunnel measurements. The solution of 3D nonstationary Navier-Stokes equations for viscous compressible fluid affected by body forces enabled to determine conditions of the 3D vortical structure (Taylor-Goertler vortices) formation, their scales and intensity, the thermal field having been realized using streamwise heated elements spaced at a certain distance (λ_z, or h_z) in a spanwise direction.

The flow geometry under consideration matched with the experimental conditions given by the airfoil model R200 and R800, i.e. with the curvature radii of 200 and 800 mm. The calculation domain was also in agreement with the experiments: its size was chosen to correlate with the airfoil geometry and size. Finally, computations were carried out for typical values of the free-stream velocity U_0=25m/s and U_0=34m/s or the length-based Reynolds numbers of $Re=5\cdot10^5$ and $Re=6.8\cdot10^5$ which corresponded to laminar and turbulent cases; spanwise scales of generated longitudinal vortices (λ_z = 2.5 and 5.0 mm) were chosen the same as in the experiments.

Computational results presented in figures 8.3.1, 8.3.2, 8.3.4, 8.3.6, 8.3.8 versus 8.3.3, 8.3.15, 8.3.7, 8.3.9 illustrate different reactions of laminar and turbulent boundary layers to thermal excitation with the same scale of λ_z=5mm and under the same basic flow curvature (concave surface with R=200mm).

Within the range of free-stream velocities of U_0=20 m/s - 40m/s, longitudinal vortices in the turbulent flow at a constant surface temperature (uncontrolled case) were found only at a level of numerical accuracy: periodical structures could be distinguished over the background noise of Reynolds stresses only at the end of the spatial domain. Therefore it is not quite evident what is the size of natural Taylor-Goertler vortices in the turbulent case.

However under the imposed spanwise-periodic temperature boundary condition, streamwise vortices develop both in laminar and turbulent boundary layers. It is seen in Figs. 8.3.1-8.3.3 from the flow topology depicted as contours of streamwise vorticity in a normal to the wall cross section at a downstream distance S=0.235m. Streamwise vortices display themselves in the spanwise velocity profiles $U_z(y)$ shown in Figs. 8.3.6, 8.3.7. Besides, there were calculated maximum values of longitudinal vorticity ω_s as a function of a streamwise coordinate S, at a constant surface temperature and two values of the spanwise temperature gradient, $\Delta T = 50^0$ and $\Delta T = 70^0$. Increased temperature difference between the surface and the heated elements resulted in the intensification of streamwise vorticity proportionally to the temperature difference, while this intensity had a background value without the thermal control.

Turbulent streamwise vortices compared to those in a laminar/transitional boundary layer have a number of specific features:

- A shape of streamwise vortices in the turbulent boundary layer only slightly reminds classical Goertler vortices.
- Turbulent longitudinal vortices are flattened (with a correspondingly smaller size normally to the wall) and stay symmetric; it goes together with the fact that maximum spanwise and normal velocities are very close, $(U_z)_{max} \approx (U_n)_{max}$.
- Growth rate of the vorticity maximum, ω_s, was practically invariant in the turbulent case in contrast to the laminar one. But a value of the maximum streamwise vorticity was found to be almost seven times less at the same control temperature parameter ΔT.

One of the most interesting findings is as follows: streamwise vorticity induced with a given scale reaches its maximum and retains in the flow relatively long. It modifies the near-wall turbulence structure due to regular exchange between the near-wall and outer regions of a turbulent boundary layer despite the fact that a local Goertler number based on the momentum thickness strongly exceeds the threshold value of G=9.

LAMINAR CASE

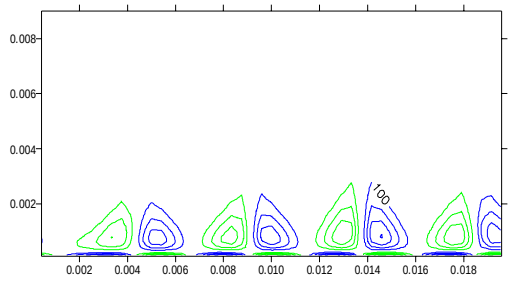

Fig. 8.3.1. T=const; S=0.235m

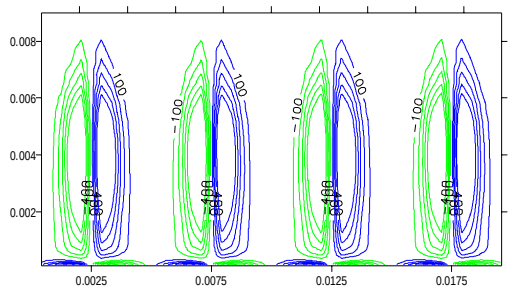

Fig. 8.3.2. T=50°C; λz=5mm; S=0.235m

TURBULENT CASE

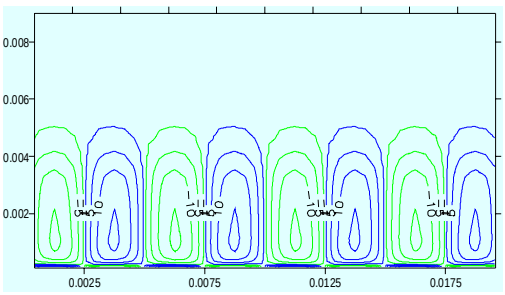

Fig. 8.3.3. T=50°C; λz=5mm; S=0.235m

LAMINAR CASE

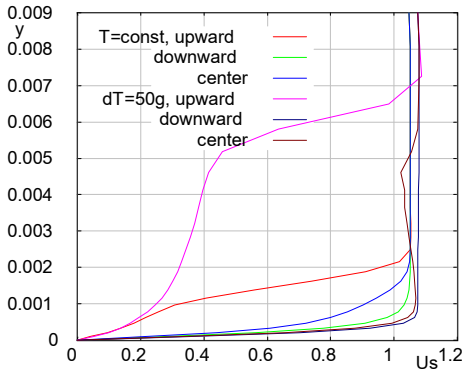

TURBULENT CASE

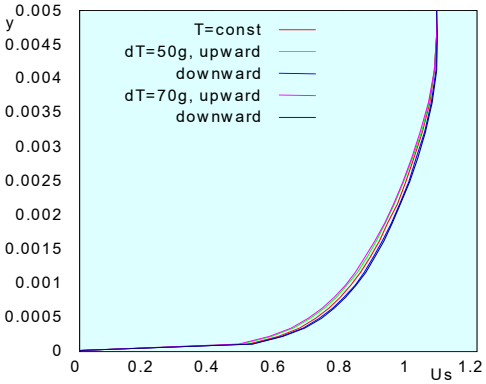

Figs. 8.3.4, 8.3.5. Streamwise velocity profiles at S=0.235m under vortex generation, λ_z=5mm

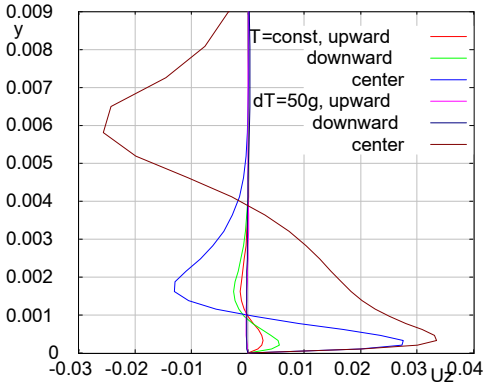

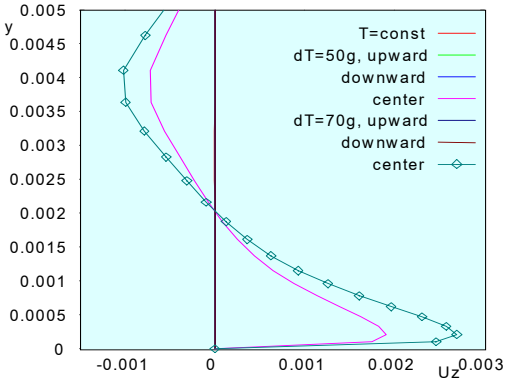

Figs. 8.3.6, 8.3.7. Spanwise velocity profiles at S=0.235m under vortex generation, λ_z=5mm

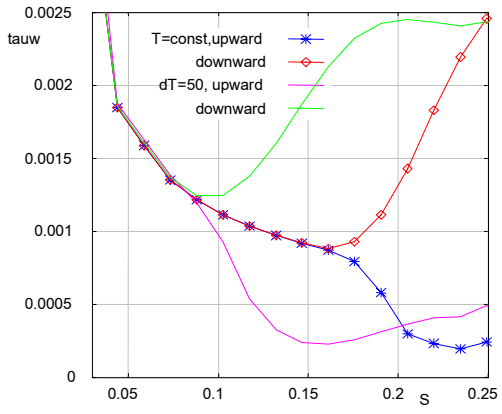

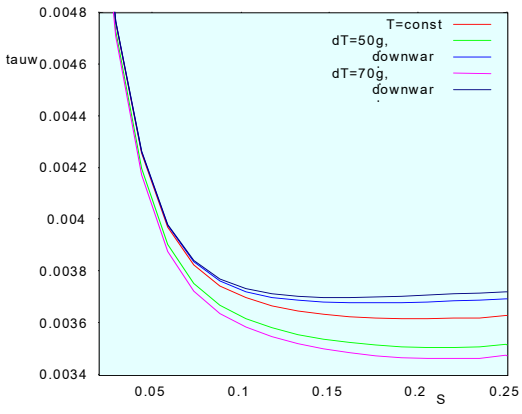

Figs. 8.3.8, 8.3.9. Wall shear stress at S=0.235m under vortex generation, λ_z=5mm.

*Values in Figs. 8.3.4-8.3.9 are calculated for 2 spanwise locations related to the downwash and upwash sections in the vortical system

Calculation results show enhanced convective transport of turbulent energy due to the organized secondary flow. Figs 8.3.8 an 8.3.9 show dimensionless shear stress $\tau_w/(\rho U_o^2)$ distribution over the surface in the downwash and upwash sections of the streamwise vortical system in laminar and turbulent boundary layers. One can conclude that

- around the heated elements in the controlled case, wall shear-stress values are lower than those in the turbulent regime without heating, and higher between the heaters with the downwash secondary flow;
- integral shear stress over the whole surface is slightly lower in the controlled case which can be explained with the flattened shape of vortices; the total energy of turbulence grows in the vicinity of the wall.

Influence of the control temperature gradient ΔT on the wall shear stress along the flow in a turbulent boundary layer is illustrated in Fig. 8.3.10.

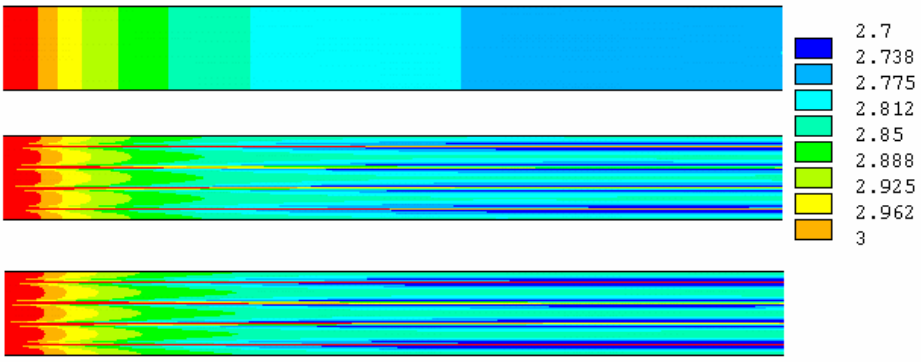

Fig. 8.3.10. Wall shear-stress distribution in a turbulent boundary layer over a concave surface with streamwise heated elements for (a) T=const=293°C, (b) ΔT=50°C, (c) ΔT=70°C.

8.4. Generation of streamwise vortices in turbulent boundary layers. Verification of computations and experiments

Previous experimental and DNS studies dealt with laminar-turbulent transition control proved that self-organized vortical structures are more receptive to the control factor having a commensurable scale. The spanwise scale of surface temperature variation corresponding to the first Goertler mode showed the best effect on flow characteristics. In present investigations with available sets of basic flow parameters, it justified more detailed tests with λ_z = 5 mm scale of induced streamwise vortices.

Estimation of the thermal control efficiency in boundary layers over concave and convex surfaces of airfoil models was made using measurements of lift and drag coefficients. These experiments showed the advantage of an airfoil model R800 compared to the R200 due to its better aerodynamics (later separations and thus longer controlled regions for a certain range of angles of attack). Therefore the concluding stage of investigations was reduced to the more detailed investigation of thermally controlled flows over surfaces with R=800 mm in conjunction with corresponding measurements of lift, drag and momentum of the R800 model, i.e. similar control regimes were analyzed numerically and experimentally under similar basic flow conditions.

Below, numerical results are presented in a form of iso-vorticity lines showing the topology of turbulent boundary layers over a concave (Figs. 8.4.1-8.4.4) and convex (Figs. 8.4.5-8.4.10) surfaces with the curvature radius of R=800 mm for free-stream velocities of U_0 = 25 m/s and U_0 = 15 m/s that exactly corresponded experimental conditions in the Wind Tunnel 2. A spanwise space scale of thermally induced vortices was chosen as λ_z = 5 mm also corresponding to the experimental conditions. On the top of each set, the reference results are shown for conditions of natural development of a vortical structure.

U_0=25 m/s

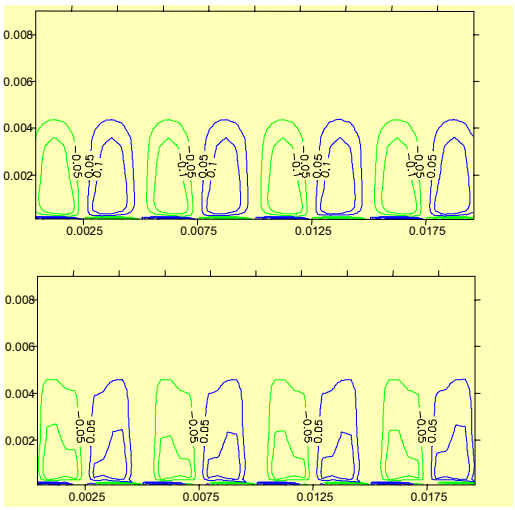

8.4.1 (top): X= 0.21771; 8.4.2 (bottom): X= 0.24881

U_0=15 m/s

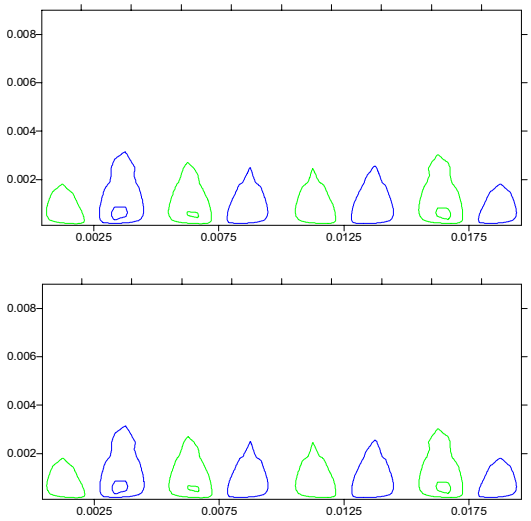

8.4.3 (top): X= 0.21771; 8.4.4 (bottom): X= 0.24881

Figs. 4.1-4.4. Streamwise vortices generated in a boundary layer over a concave surface at different downstream distances X : λz=0.5 cm; ΔTz=350C; U0=25 m/s (left) and 15 m/s (right)

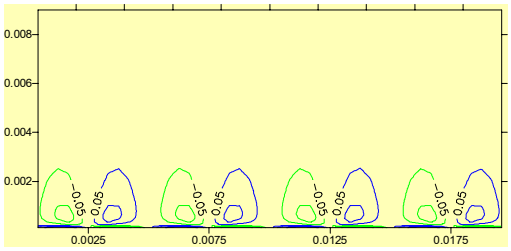

8.4.5: X= 0.21771

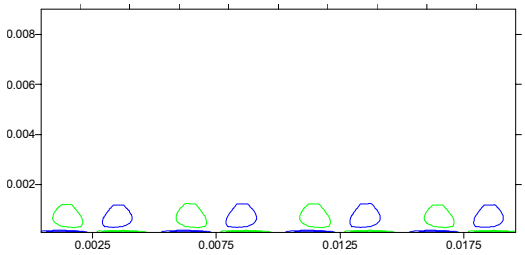

8.4.8: X= 0.21771

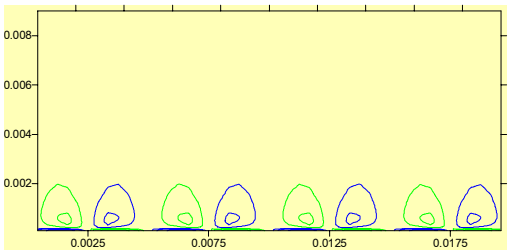

8.4.6: X= 0.24881

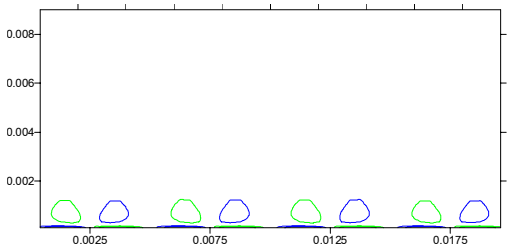

8.4.9: X= 0.24881

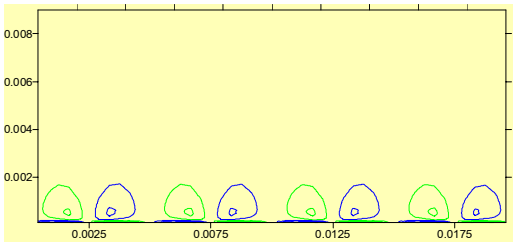

8.4.7: X= 0.27991

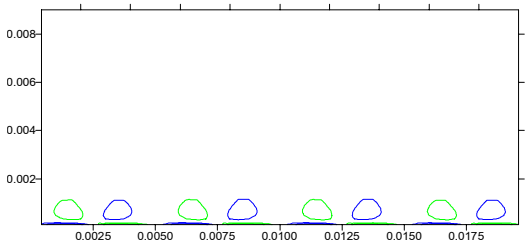

8.4.10: X= 0.27991

Figs. 8.4.1-8.4.10. Streamwise vortices generated in a boundary layer over a **convex** surface at different downstream distances X : λ_z=0.5 cm; ΔT_z=35^{0}C; U_0=25 m/s (left) and 15 m/s (right)

Numerical results obtained for flat and convex surfaces under uniform boundary conditions (a reference case without heating) showed no evidence of coherent vortices. The initial 2D flow always stayed two-dimensional. However nonuniform boundary conditions in a form of the temperature varying regularly in a spanwise direction ΔT_z resulted in the formation of vortex pairs similar to the Goertler vortices. However their intensity (streamwise vorticity) was found to be about one order lower than in case of a flow over a concave surface. In addition, no noticeable shear stress nonuniformity was found in a spanwise direction like in case of the concave wall: local shear stress fluctuations around an averaged value did not exceed 1%.

All the effects were found to be more pronounced over a concave surface. To compare effects over concave and convex surfaces as well as to give a clue to experiments, figures 1-4 show the shear stress distribution (tauw) along curved surfaces. The numerical results were obtained for the curvature radius R=200 mm, free-stream velocity U_∞=20 m/s and for different spanwise locations related to lines between two neighboring vortices with a downward and upward fluid motion, i.e. directions of the circumferential velocity, as well as for different signs of the surface curvature (concave and convex walls). Calculations took into account a downstream distance, s [m], and streamwise velocity profiles at the end of a computational domain, i.e. at s=0.19 m. Figs. 8.4.11 and 8.4.12 correspond to the concave, Figs. 8.4.13 and 8.4.14 describe the vortex dynamics over the convex surface. The reference case is depicted with the uniform temperature over the tested surface T=0, i.e. with the control factor switched off.

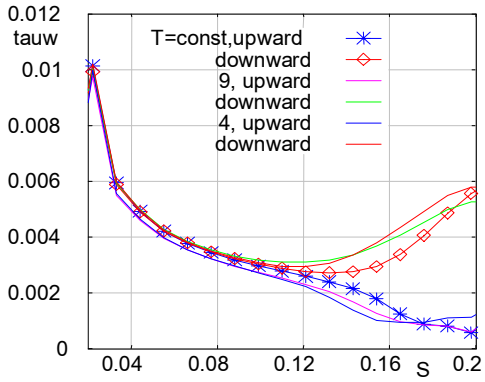

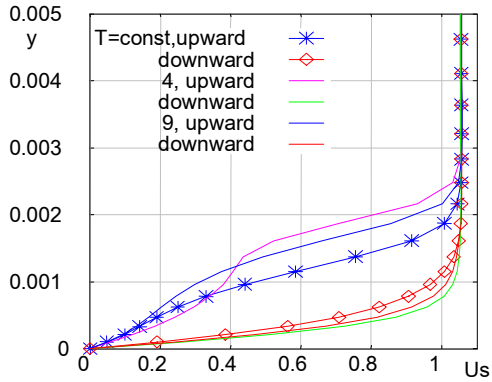

Figs. 8.4.11, 8.4.12. Concave surface, 9 is for the z-scale, λ_z=2.5mm; 4 is for λ_z=5mm

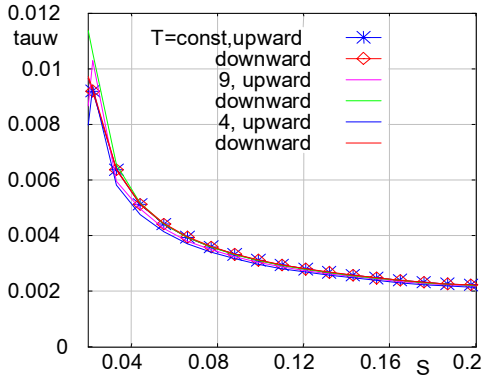

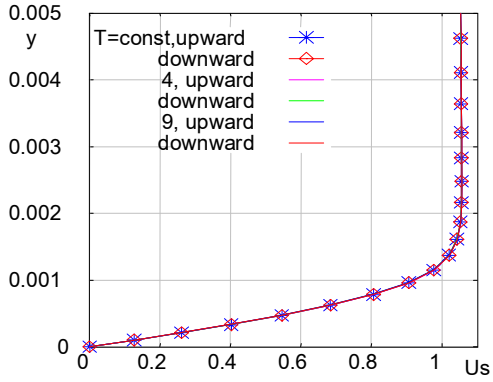

Figs. 8.4.13, 8.4.14. Convex surface, 9 and 4 correspond to vortices generated with λ_z=2.5mm and 5mm

The concave surface represents the most interesting situation from the viewpoint of flow control: vorticity in a boundary-layer grows downstream both in controlled and reference cases. The thermally introduced z-scale corresponding to the first Goertler mode makes the intensity of secondary vorticity almost twice higher than the reference value and more than 3 times higher in the beginning of a test

surface. Even the generated second Goertler mode results in a more than 1.5 higher intensity of vorticity in the beginning of the test plate compared to the natural formation of vortices (a reference case). However observed growth rates are lower in this controlled case and therefore at a certain downstream position, the intensity under natural conditions prevails over that of the controlled case.

As to the scale of thermally stimulated vortical structures, the turbulent bondary layer displayed the same tendency as the laminar-transitional one: effects were larger when the control factor had a commensurable scale with self-organized streamwise vortices in a flow affected by centrifugal forces. The greater were the values of a free-stream velocity, surface curvature and a distance between the heated elements (λ_z), the higher was the intensity of developing streamwise vorticity.

Streamwise vortices were observed to decay downstream together with their elongation normally to the wall. This effect was more pronounced and stable for the larger scale vortices generated, i.e. those corresponding to the 1st Goertler mode.

Conclusions

Potential to control near-wall flows over surfaces with different curvature was analyzed on a basis of 3D Navier-Stokes equations for compressible fluid using thermal generation of streamwise vortices.

Numerical experiments showed that both natural and forced development of the vortical system strongly depends on the flow regime, laminar or turbulent. Geometry and intensity of streamwise vortices was determined depending on values of the surface curvature and free-stream velocity as well as their modification downstream and influence on boundary layer characteristics.

Shortly, basic findings can be listed as follows:

Naturally developing streamwise vortices were not found in turbulent boundary layers even over a “stimulating” concave surface.

Spanwise scale and temperature gradient $\Delta T(z)$ over concave and convex surfaces are determined which result in most intense and long-living streamwise vortices.

For flows over concave surfaces with a fixed curvature, velocity range was found with the maximum vorticity growth. In a determined temperature range, almost linear dependence of vorticity on ΔT was found.

Streamwise vortices can be maintained over a convex surface under conditions of the imposed $\Delta T(z)$ as a boundary condition. Their intensity is lower compared to that over a concave wall. Nevertheless, it can be recommended as a method of separation control over surfaces with unfavorable pressure gradient. Flow characteristics are essentially changing in the vicinity of separation under generated streamwise vortices.

9. EXPERIMENTAL FACILITIES, THEIR PREPARATION TO MEASUREMENTS. CALIBRATIONS, MEASUREMENT OF BASIC FLOW PARAMETERS, ACCURACY OF MEASUREMENTS

Experiments in both experimental facilities of WT1 and WT2 were planned and prepared in parallel. The basic idea was to establish correlation between kinematic features (vortical structure of a boundary layer) and integral flow parameters in a form of drag C_x and lift C_y coefficients characterizing the airfoil efficiency. Since thermal control of the boundary layer is supposed to change the near-wall vortical structure, it should affect measured forces and momentums of airfoil models under generation of streamwise vortices (controlled case) compared to reference cases. Using the same airfoil models, different measurement and data processing systems in wind tunnels with close but not identical parameters, these parallel tests must ensure validity of obtained results.

9.1. Boundary-layer visualization: calculation of a system for a fluorescent aerosol spray technique

Flow visualization is proven to be the most effective way to get an idea about the velocity field. In addition, it can show with good accuracy a position of a separation zone over a model. The second is especially important for the experiments in the Wind Tunnel 2 because of high free-stream turbulence level there which strongly complicates the task to distinguish small-scale vortical structure, its regular character and modifications depending on values of flow and control parameters. Therefore thorough analysis and preliminary tests were carried out to choose acceptable visualization methods.

Choice of flow visualization methods was based on the following criteria:

- temperature field, $\Delta T(z)$, given on the surface should not directly affect the flow-field picture displayed on a model surface;
- substances used for visualization should not influence the vortical structure, be dielectric, have a color well distinguished from that of the model;
- simplicity and safety of application;
- reliable registration and interpretation of results.

As a result, two methods were selected to begin with. First, dispersed fluorescent aerosol was studied in the UV light. Secondly, some kind of surface flow visualization, must be useful e.g. like methods using liquid crystal coating. Quantitative assessments related to the first method were based on the available experience of work in NAU with aerosol dispersions solving practical problems of flights under different meteorological conditions as well as of icing.

It is known that fluorescent dye technique is technologically simple, effective for various flow situations and not costly. If focused basically on quantitative aspects like detection of developing streamwise vortices of a given scale, the method does not require sophisticated registration of data and the results can be easily interpreted. Other requirements related to the considered boundary-layer problem are satisfied too: used substances do not influence the near-wall flow structure and a temperature field over the model surface does not affect directly dye distribution and intensity.
However a number of adjustment tests with available liquid crystals showed ambiguity of result interpretation because of rather narrow temperature ranges of the liquid crystal sensitivity. This difficulty aggravated with inevitable need to work in a wide temperature range since it was a basic control parameter in the problem under consideration. The latter stimulated further search of proper visualization methods.

Taking into account a fine structure of the flow under consideration, detailed estimations have been made of liquid aerosol generation using a pneumatic ejector nozzle as well as of illumination conditions. Calculations

based on the previous experience of icing simulation in wind tunnels were made of a sprayer with the co-axial concurrent flow and further mixing of colored liquid and air.

Necessary water consumption was found from the condition of aerosol quality corresponding to a cumulus cloud, 0.37 g/m^3 and the free-stream velocity in a wind tunnel test section of 28 m/s for a cross-section of 0.04 m^2. At a nozzle diameter for a liquid phase equal to d_0=0.5-1.4 mm, the water flow rate is 0.95-0.12 m/s and the required excessive water pressure at the nozzle entrance is 0.02-0.0006 kg/cm^2. Calculation of a gas phase flowing through the nozzle showed that at the nozzle diameter d_2= 4 mm and excessive entrance pressure of 1 kg/cm^2, the air would flow with the sound velocity. Therefore gas phase calculations related to its consumption, velocities in a jet, jet dimensions were made for the velocity 340 m/s at a nozzle exit with d_2= 4.0 - 3.0 mm. External diameter of a nozzle for the liquid phase was d_1= 0.8 - 2.0 mm.

Table 9.1.1 presents results of calculated diameters d_d of droplets depending on the correlation between the consumption of gas Q_{gp} and liquid phases Q_{lp}= 0.37 g/s as well as d_0 values. It shows a possibility to generate aerosol droplets with the diameter of 2-10 Mcm for the chosen sprayer geometry. Droplets dimensions can be made even less provided that volatile substances are used.

Table 9.1.1

d_2, mm	4.0	3.0	4.0	3.0	4.0
d_1, mm	0.8	0.8	2.0	2.0	1.2
Q_{gp}, g/s	5.02	2.73	3.92	1.635	4.76
d_0, mm	0.5	0.5	1.4	1.,4	0.8
D_d, Mcm	1.88	3.45	4.02	9.64	2.5

Tables 9.1.2 and 9.1.3 show calculated velocities $V_з$ and expansion of the mixing zone d_c along a length x of an axisymmetric turbulent jet. Free-stream velocity at the nozzle location near the wind tunnel confuser is 6 m/s at a distance of 1.5 m from the nozzle exit under the condition of a free-stream velocity equal to 28 m/s in a test section.

Table 9.1.2

x/d_2	50	100	150	200	250	300	350
x, mm	200	400	600	800	10000	1200	1400
$V_з/V_0$	0.138	0.0747	0.0543	0.044	0.038	0.034	0.031
$V_з$, m/s	47	25.4	18.5	15	13	11.6	10.6

Table 9.1.3

$d_ç/d_2$	18	33.5	45	55	64	72.5	79.5	86.5	92	97
$2x/d_2$	100	200	300	400	500	600	700	800	900	1000
x, mm for d_2= 4 mm	200	400	600	800	1000	1200	1400	1600		
$d_ç$, mm for d_2= 4 mm	72	134	180	220	256	290	318	346		
x, mm for d_2= 3 mm	150	300	450	600	750	900	1050	1200	1350	1500
$d_ç$, mm for d_2= 3 mm	54	101	135	165	192	218	239	260	276	291

Based on the above calculations, the sprayer has been fabricated with changeable air nozzles with d_2= 3.0; 3.5; 4.0 mm and liquid nozzles with d_0= 0.5; 0.8; 1.4 mm. Calculation results were verified experimentally.

Fig. 9.1.1. Airfoil model mounted in WT 2 for visualization

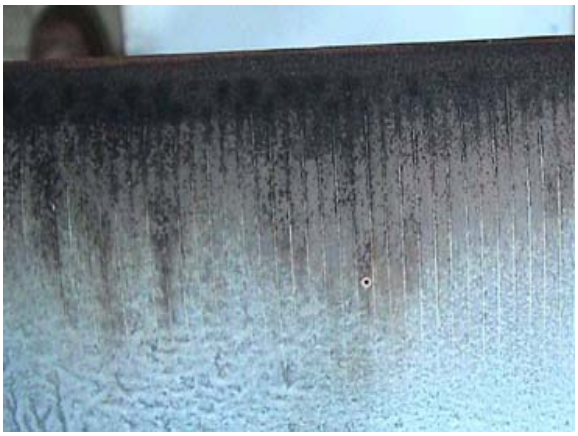

Fig. 9.1.2. Surface visualization of a flow structure in a thermally controlled boundary layer over the R200 airfoil model mounted in WT 2

An illumination system has been assembled on an optical bench and tested using fine talc powder as the visualization agent. There was provided a possibility to apply either a 25 mW laser or a 400 W lamp as a light source as well as to control the light sheet parameters such as its dimensions and location over a model. Flow structure was found to be visible in the whole lightened space, e.g. trailing vortices of a few millimeter size could be registered.

Thus presented above calculations of pneumatic ejector operation provided necessary parameters and values for optimal water discharge and its mixing in the nozzle air stream. It was shown that dimensions of aerosol drops depending on the ejector parameters (nozzle diameter, mixing length and velocities) and the free-stream velocity in a wind tunnel test section can be obtained as little as 2-10 μm.
Visualization was made around the R200 model at 4.5^0 and 16^0 angles of attack, free-stream velocity U_0=10m/s using iodine aerosol interacting with a surface layer of the overcoated starch. Results were registered in a light sheet with the digital SONY camcorder in its infrared mode of operation that provided most contrast pictures. This method together with the fluorescent aerosol and talc spray methods was found to be good to register large-scale trailing vortices with a core size estimated as ~2.5 cm; no difference was noticed for reference and controlled cases. However having been applied to visualize boundary layers, the developed approach appeared to have insufficient resolution to display the fine vortical structure of interest.

In this connection, surface visualization that was initially supposed as an alternative and/or supplementary method in the whole set of measurements, was concluded to be taken as the basic method to observe both the near-surface vortical structure and the separation region.

As a result, surface starch-iodine based visualization (Figs. 9.1.1, 9.1.2) showed a separation line location over a convex surface as a darker area resulted from the intense mixing of chemically reacting substances. In addition, a lighter strip followed by an equidistant dark strip upstream of the separation line evidenced the laminar-turbulent transition area. Although the images were not very contrast, obtained statistics enabled to conclude that *the transition line was located at ~ 27% of a cord in a reference case ("cold" model), and at ~ 40% in a controlled case (streamwise elements heated up to Δt = +40°C)*.

Besides, camcorder resolution made it possible to observe streamwise patterns over a model surface consisting of grains of reacting substances along heated wires (Fig. 9.1.2); farther downstream the colored "tongues" merged having shown a large-scale spanwise-regular structure.

9.2. Setup measurement of integral boundary-layer characteristics in WT 1 and WT 2 under conditions of thermal control

Wind Tunnel WT 1 (low turbulence level)

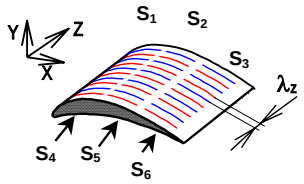

(Fig. 5.3.1)

Experiments were carried out at free-stream velocities $U_I \approx 10$ m/s, $U_{II} \approx 15$ m/s and $U_{III} \approx 20$ m/s and angles of attack of an airfoil model varying within $\alpha = -10° \div 35°$. The model R800 (i.e. one having the basic curvature radius on both sides R=800 mm) was tested: cord and span $b=l=0.2$ m, surface square $S = 0.04$ m^2, relative thickness of the aerodynamic profile $\bar{c} = c/b \approx 12\%$; $\bar{x}_c \approx 20\%$. The spanwise distance between heated wires with the diameter of 0.1 mm was chosen as $\lambda_z = 2.5$ mm. Three electrically independent sections along a cord on both convex (S1, S2, S3) and concave parts (S4, S5, S6) of the airfoil model enabled to analyze various regimes of the thermal control. For explicitness, Fig. 5.3.1 is shown here again. Any section could be heated individually as well as in various combinations (see Table 9.2.1) due to separately applied voltage that regulated the spanwise scale $\lambda_z = 2.5$ mm or 5 mm, downstream location of the controlled section and intensity of the effect.

Table 9.2.1.

No.	Controlled (heated) sections	Spanwise scale λz, mm	Applied electrical power P
1	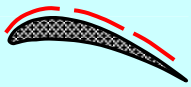	$S_1 = 2.5$ $S_2 = 2.5$ $S_3 = 2.5$	P/4 P P
1a	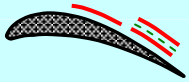	$S_2 = 2.5$ $S_3 = 5.0$	P P/2
1b	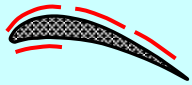	$S_1 = 2.5$ $S_2 = 2.5$ $S_3 = 2.5$ $S_4 = 2.5$	P/4 P P P/4
2	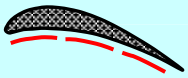	$S_4 = 2.5$ $S_5 = 2.5$ $S_6 = 2.5$	P/4 P P
2a	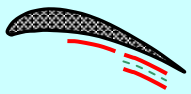	$S_5 = 2.5$ $S_6 = 5.0$	P P/2
3	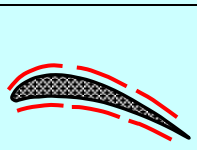	$S_1 = 2.5$ $S_2 = 2.5$ $S_3 = 2.5$ $S_4 = 2.5$ $S_5 = 2.5$ $S_6 = 2.5$	P/4 P P P/4 P P

Practically, the thermal control was realized according to the following scheme. The control factor (voltage) was switched on for a fixed time interval (typically 60 seconds) after the flow was stabilized in a wind tunnel. Each test cycle was carried out for the three mentioned above values of the free-stream velocity. These cycles differed by combinations of heated sections. Main attention was focused on heating of all 6 sections (case 3) or separately 3 sections of a pressure side (case 2) or 3 sections of a suction side (case 1). The basic task was to find most economic combination of heated sections that would result in an expected effect (e.g. the flow separation delay). In other words, a subtle influence on a boundary-layer flow structure (e.g. through heating only leading edge sections) with the minimal energy consumed was an objective of these experiments.

The first analysis of the directly measured aerodynamic force components X and Y changing in time (as oscillograms) showed that the drag was steadily decreasing from the very beginning and during the whole time of heating. After the voltage was switched off, forces came back to their initial values. It was typical for all cases but most visible for the case 3, (S_1 - S_6 sections heated). In addition, recorded signals displayed definite appearance of low frequency components having evidenced the vortex structure reorganization in a controlled boundary-layer flow.

Fig. 9.2.1 shows signals registered during one typical run: zone 1 corresponds to the zero free-stream velocity; 2 is a zone of the flow acceleration; 3-5 – U_0=const; 4 or (H)—test regime: constant free-stream velocity, heat control factor switched on; 5 – heat-control factor switched off; 6 – decelaration; 7—zero velocity, switched off thermal control and registration of the test parameters. The

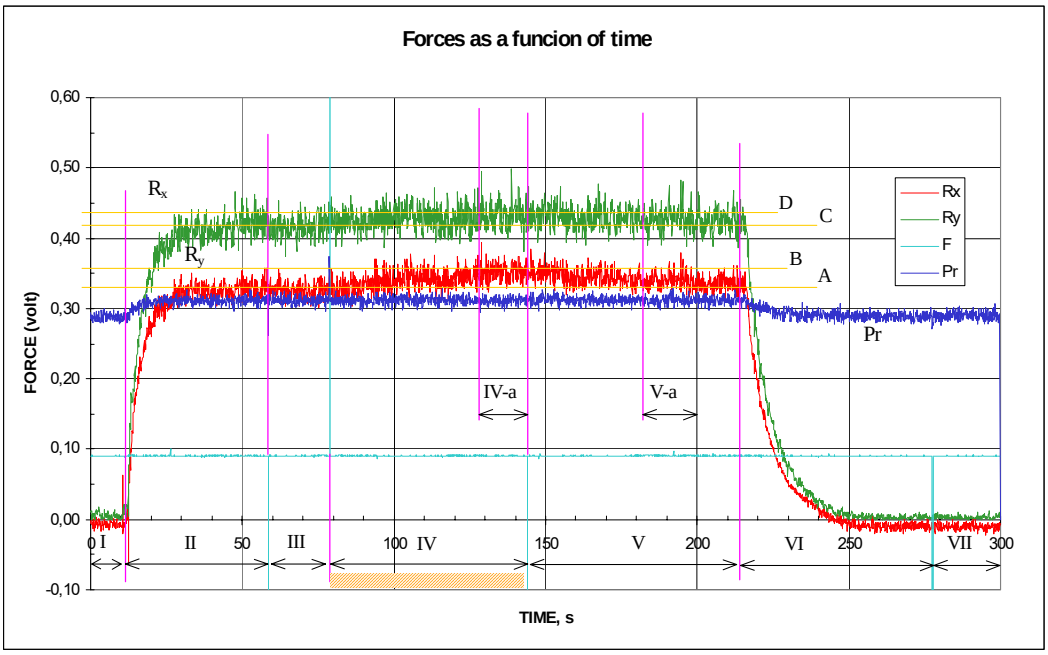

Fig. 9.2.1. Oscilloscope signals obtained for the R800 model in a reference case (blue) and heat-controlled cases (R_x red, R_y green); pink – operation time marks

obtained results give the first evidence of influence of the spanwise-regular heating on the boundary-layer characteristics.

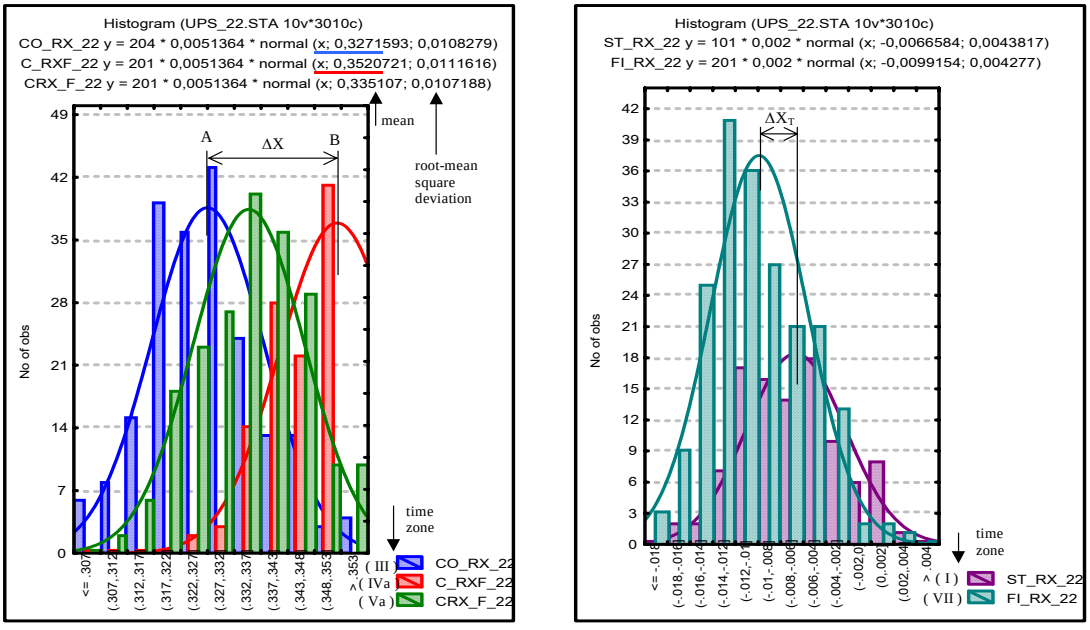

Fig. 9.2.2 (right). Statistical description of the thermal control effect on the lift and drag forces acting on R800 model: blue – reference, red – drag, green – lift;
Fig. 9.2.3 (left). Negligible residual effects of the thermally controlled flow structure after the voltage is off.

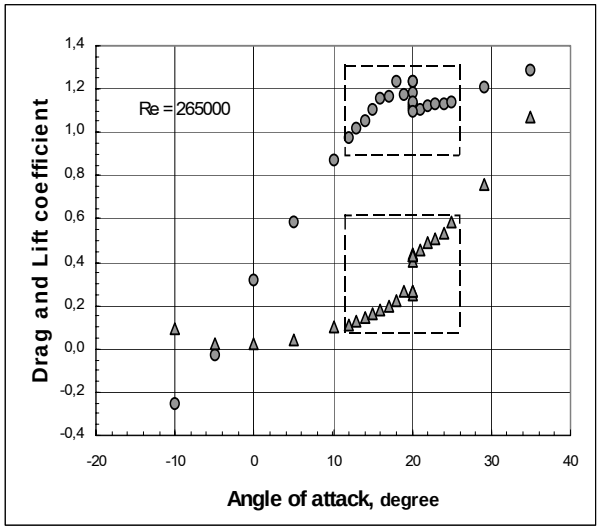

Fig. 9.2.4. Lift (top) and drag (bottom) coefficients in the vicinity of a critical angle of attack, R800

The discussed effects can be better seen from the data processed using the dispersion analysis presented below in a form of histograms (Figs. 9.2.2, 9.2.3). Each statistical ensemble consisted of 100-600 measured values in all zones of interest, i.e. in the zones III, IV-a and V-a shown in Fig. 9.2.2 for the thermal control case where colored lines correspond to those of Fig. 9.2.1. All the realizations were based on a comparison of signal levels at $U_0 = U_5 = 0$ to determine possible signal trend in time and in every channel. Fig. 9.2.3 illustrates the fact of flow conditions practically coming back to the initial state after the control factor is switched off (zones I and VII).

Results of the statistical analysis showed a clear dependence of aerodynamic forces on thermal conditions in a boundary layer, the effect having been estimated to be about 7.6% both for measured normal and streamwise forces while the mean root square error during these measurements having been no more than 0.5%.

To catch the correlation between the boundary-layer structure and integral flow characteristics, the measurements were carried out at supercritical angles of attack when the boundary layer displayed available zones of instability (Fig. 9.2.4). Then even a slight modification of the flow structure could change the separation location and, accordingly, drag and lift coefficients.

For the R 800 airfoil, a critical angle of attack was found to be $\alpha \approx 20^\circ$ for the free-stream velocity of $U_\infty \approx 20$ m/s and $\alpha \approx 17^\circ$ for $U_\infty \approx 10$ and 15 m/s (see Fig. 11). Therefore experiments started from $\alpha \approx 22^\circ$. To reduce a measurement error, parameters were registered and time-averaged within one run. For higher reliability, each run for a chosen set of conditions was repeated several times. An RMS error of measured forces was no more

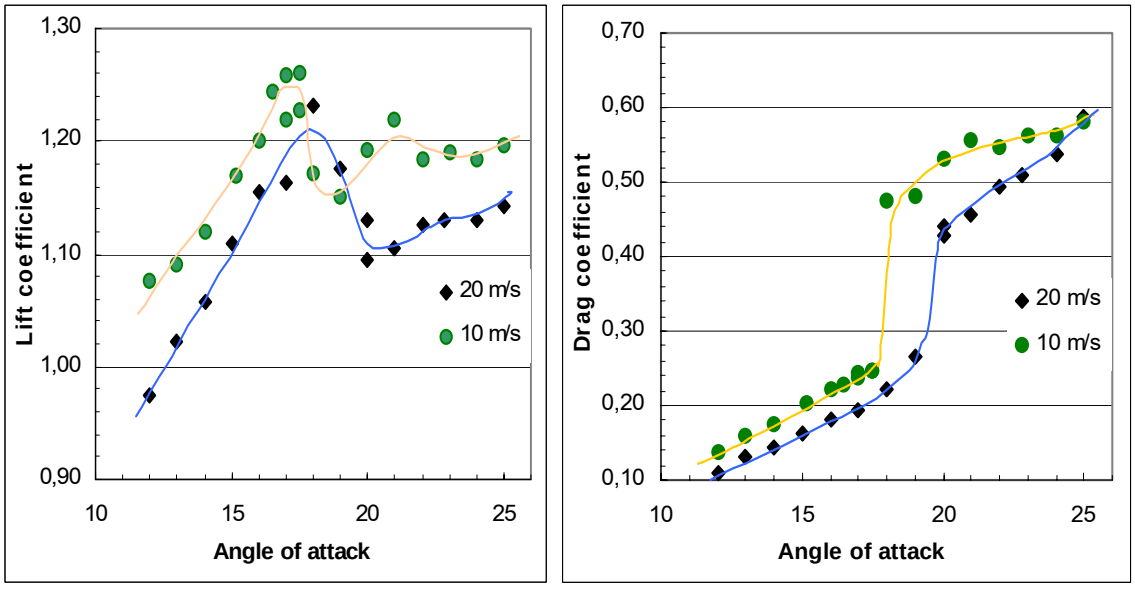

Fig. 9.2.5. Reference measurements of lift and drag coefficients of R800 model *vs* angle of attack for free-stream velocity $U_0 = 10$ m/s and 20 m/s

than 0.7%. It gave somewhat higher errors for lift and drag coefficients because of less accurate velocity measurements. Fig. 9.2.5 shows lift and drag coefficients obtained from the force measurements in reference cases, i.e. without heating, for 2 different values of a free-stream velocity under conditions around flow separation.

Drag and lift coefficients obtained from the force measurements for different schemes of heat control are displayed in Fig. 9.2.6. Blue lines show a reference case without heating. Color points correspond to different control cases numbered in accordance with the Table 6, measurements having been carried out for one near-critical angle of attack.

It should be mentioned that the lift force appeared to be more sensitive to the modification of the flow structure caused by the spanwise periodic surface heating that must have followed from changed streamwise extension of laminar and turbulent zones and a location of separation.

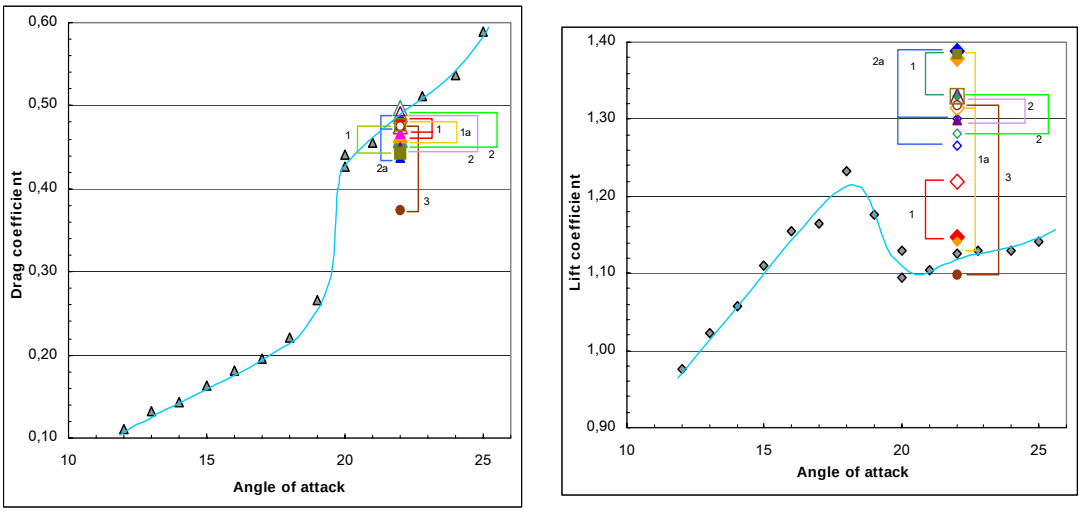

Fig. 9.2.6. Drag and lift coefficient calculated from the measurements of R 800 model (for notation, see Table 9.2.1)

Heating of a convex surface (see Table 9.2.1) resulted in drag reduction as it is seen from Fig. 9.2.6, left, point 1. Taking into account that the measurements were carried out in the unstable mode by the angle of attack, measured values of the lift force were also unstable having shown insignificant growth with a subsequent drop after the voltage was switched off.
Heating of a concave surface didn't show noticeable and stable changes of lift (Fig. 9.2.6, right, point 2).

Optimization of the flow control was tried in terms of "energy consumption – favorable effects". It was implemented in 2 ways: (1) reducing a temperature gradient ΔT in a spanwise direction, i.e. a value of applied voltage, and (2) reducing a number of heated sections to minimum. The first approach was exploited in detail mainly in the wind tunnel WT 2 while the second one was initiated in the WT 1 though with different airfoil models that enabled the parallel work. Lower electrical power consumed for heating of the separate middle S_2 section with a scale of $\lambda_z = 2.5$ mm or/and the trailing-edge section S_3 with a scale of $\lambda_z = 5$ mm (case 1-a, Table 9.2.1) resulted roughly in the same effects as in case 1 under heating of the whole convex surface. Similar results were obtained in cases of the concave surface heating, i.e. cases 2 and 2-a.

On the whole, one can conclude that the applied method of the boundary-layer control around an airfoil enables to influence both its drag and lift, in particular to increase a critical angle of attack using different schemes of the thermal control.

This conclusion is in a good agreement with the measurements in WT 2 of drag, lift and momentum, $c_x, c_y, m_z = f(t, \Delta T)$, as a function of heating time *t* and a spanwise temperature gradient within angles of attack varying in a range of α = -10…+26° at a maximum temperature gradient, ΔT = 40°C. A measurement cycle took 350 sec. at $\alpha = const$ under registration of measured values every 7 sec., the first 50 sec having been recorded for a "cold" model, the next 150 sec for the heated model, and last 150 sec after the voltage switched off. Some results are displayed in Fig. 9.2.7.

9.3. Measurement of integral boundary-layer characteristics in WT 2 under conditions of thermal control. Variety of test conditions, measurement procedure, preliminary results.

Having shared models between two facilities, Experiments in WT2 were initially focused on testing R200 model, total 29 tests runs of the first set and 55 test runs of the second set were performed. Subsequently, 18 and 72 test runs respectively were performed for R800 model. Several tests were performed with reversed position of R800 model (sharp trailing edge directed upstream). This was done to exclude influence of a relatively thick nose section of the model on the boundary layer development and thus to closer match with the computational formulation of the problem. The same variables as in computations were taken into consideration: a number of heated strips, a spanwise distance between them (2.5 and 5 mm), temperature difference between heaters and the free stream (ΔT = 20, 40, and 60°C), and free-stream velocity.

A variety of experimental conditions for tests in WT2 related to combinations of heated sections shown in Fig. 5.3.1 and in Table 9.2.1 is illustrated by Tables 9.3.1 and 9.3.2.

Table 9.3.1. *Thermal control test regimes in WT 2:* **R200** Airfoil model

Measured values	α	Δt	**Heated sections** (Fig. 5.3.1)					
			S_1	**S_2**	**S_3**	**S_4**	**S_5**	**S_6**
$c_x, c_y, m_z = f(\alpha)$		8...12	2,5	2,5	2,5	2,5	2,5	2,5
		20						
		26...30						
$c_x, c_y, m_z = f(t)$	3.2	31						
	5.2	25						
$c_x, c_y, m_z = f(\alpha)$		7…10	5	5	5	5	5	5
		16.5						
$c_x, c_y, m_z = f(t)$	6,8	21.5						
	3,2	17						
	4,2							
	5,2							
$c_x, c_y, m_z = f(t)$	4,2	20	2,5	2,5	2,5	2,5	2,5	2,5
		40						
	4,7	20						
		40						
$c_x, c_y, m_z = f(\alpha)$ (U_0 = 18 m/s)		8,5						
		19,5						
		30,5						
		25						
$c_x, c_y, m_z = f(t)$	2,5	40	2,5	-	-	-	-	-
	-10							
	-4							

$c_x, c_y, m_z = f(t)$	2,5 1,5 -4 -10	22…40	2,5	2,5	-	-	-	-
$c_x, c_y, m_z = f(\alpha)$		40	-	-	-	2,5	-	-
$c_x, c_y, m_z = f(t)$	10 8 2 -10	40						
$c_x, c_y, m_z = f(\alpha)$, ($U_0$ = 24 m/s)		40	-	-	-	2,5	2,5	-
$c_x, c_y, m_z = f(t)$	10 8 4 2 -4 -10							
$c_x, c_y, m_z = f(\alpha)$, ($U_0$ = 24 m/s)		18 22 40	-	-	-	2,5	2,5	2,5
$c_x, c_y, m_z = f(t)$	10 8 4 2	20…40						
$c_x, c_y, m_z = f(\alpha)$, ($U_0$ = 24 m/s)		40	2,5	2,5	2,5	-	-	-
$c_x, c_y, m_z = f(t)$	1,5 4 2 10 12 0 -10							

Table 9.3.2. *Thermal control test regimes in WT 2:* **R800** Airfoil model

Measured values	α	Δt	**Heated sections** (Fig. 5.3.1)					
			S_1	**S_2**	**S_3**	**S_4**	**S_5**	**S_6**
$c_x, c_y, m_z = f(\alpha)$		20 40	2,5	2,5	2,5	2,5	2,5	2,5
$c_x, c_y, m_z = f(t)$, (U_0 = 20, 28 m/s)	16 16 19 7 6,5 6	20 40 20…40						
$c_x, c_y, m_z = f(\alpha)$		40	-	-	-	2,5	2,5	2,5
$c_x, c_y, m_z = f(t)$	-6 +2							

$c_x, c_y, m_z = f(\alpha)$		40	2,5	2,5	2,5			
$c_x, c_y, m_z = f(t)$	1,0	40	2,5	2,5	2,5	-	-	-
$c_x, c_y, m_z = f(\alpha)$, ($U_0$ = 15 m/s)								
$c_x, c_y, m_z = f(\alpha)$, ($U_0$ = 20 m/s)		40	2,5	2,5	2,5	2,5	2,5	2,5
$c_x, c_y, m_z = f(\alpha)$, ($U_0$ = 28 m/s)								

To analyze effects of streamwise vortices generated in boundary layers, aerodynamic coefficients were continuously measured within a period of one experimental run while heated elements were switched on and then off. The procedure consisted of the following stages:

- zero-velocity loadings were measured and approximation coefficients were found;
- given values of a free-stream velocity and an angle-of-attack were set up;
- aerodynamic forces were measured in a reference case of a “cold” model during approximately 50 sec with the sampling taken every 7 sec;

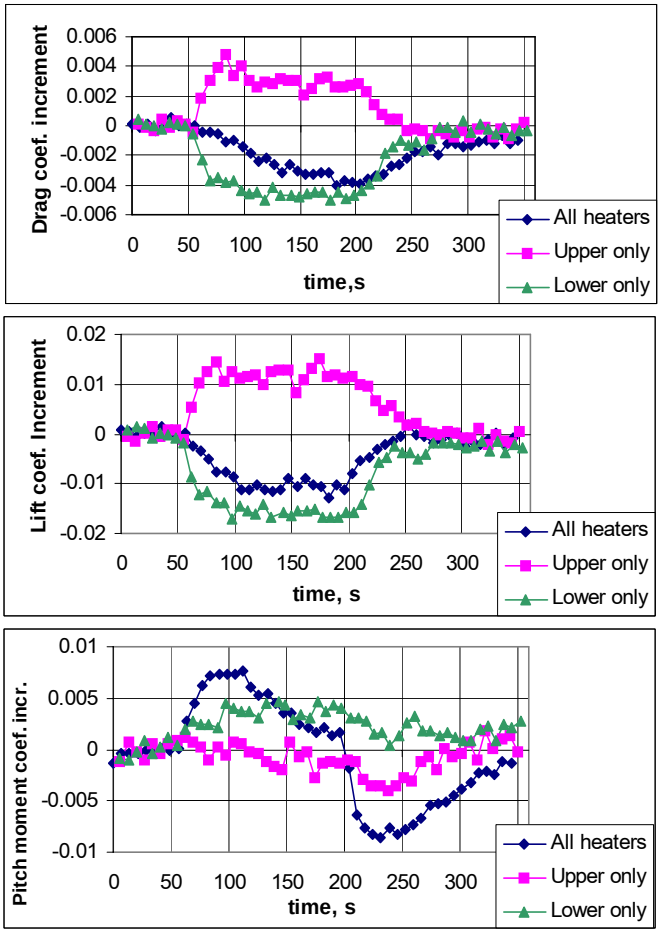

Fig. 9.2.7. Integral flow characteristics of R200 model measured in WT 2: $\alpha \approx 4.5°$; $\Delta T = 40°C$; λ_z=2.5 mm

- measurements were continued under controlled conditions, i.e. with the heaters “on” during 150 sec;
- heaters were switched off and forces were measured for a model in a process of its cooling.

The whole measurement cycle took ~ 350 sec.

The procedure of the data acquisition has been set up as follows. During approximately 2 seconds, a sample of 256 data from each balance component and dynamic pressure transducer was registered and physical loads together with dynamic pressure were calculated. From these, the calculated values of zero-velocity forces and support forces were subtracted. Aerodynamic coefficients were calculated for each of 256 data sets. Obtained values were digitally processed to reduce the noise; after that, mean and standard deviation values were calculated. They represented measurement results "in a point" at a given angle-of-attack and/or at a certain moment of the cycle. Increments of lift, drag and pitch moment coefficients of the model R200 are shown in Fig. 9.2.7 for different arrangement of heated sections, upper (convex) and lower (concave). Taking into account poorer aerodynamic quality of this model and finer than optimal z-spacing of heated strips as it was shown in the numerical modeling, the results display the thermal control method feasibility and flexibility.

9.3. Planning of experiments in WT2: reference measurements, tests under different regimes of flow and thermal control parameters

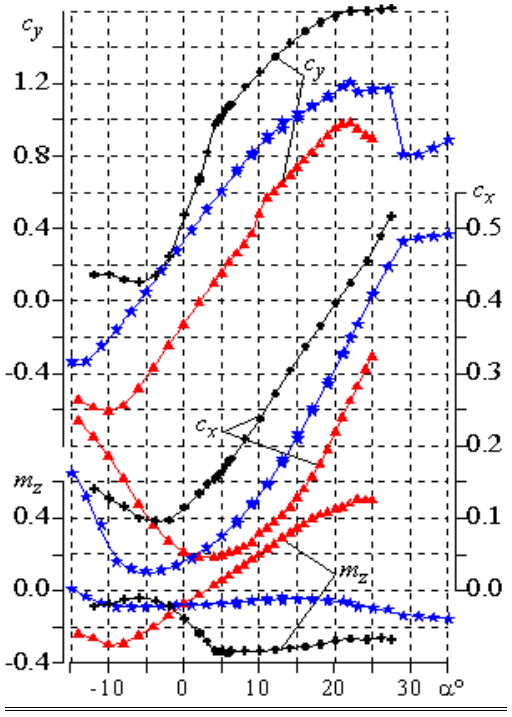

Fig.9.3.3. Lift c_y, drag c_x, and pitch momentum m_z coefficients *vs* angle-of-attack for tested **R200** and **R800** models:

R200, normal, $x_{m_z\,\text{ref.}} = 25\%$;
R800, normal, $x_{m_z\,\text{ref.}} = 25\%$;
R800, reversed, $x_{m_z\,\text{ref.}} = 75\%$

First of all, reference aerodynamic characteristics of the two models were tested, i.e. under conditions without heating; the results are depicted in figure 9.3.1. R200 model shows a quite narrow range of angles-of attack ($-4 < \alpha \le 4°$) where flow separation does not take place. At $\alpha < -4°$ the flow separation is observed on the concave surface downstream the beak-shaped nose section of the model. At $\alpha > 4°$ flow separation begins in the vicinity of the trailing edge and as the angle-of attack increases, the separation point shifts upstream.

R800 model in a "normal position", i.e. with its leading edge facing upstream, exhibits the trailing edge flow separation at larger $\alpha \approx 12\ldots14°$ and substantially shorter range of separation point shift towards the model nose. An almost horizontal part of the lift characteristics at $\alpha = 22...27°$ is followed by an abrupt lift drop.

R800 model in a reversed position (with the trailing edge upstream) demonstrates two rather wide parts of an almost linear $c_y = f(\alpha)$ dependence and a singularity region at $\alpha = 9...11°$.

The reference characteristics of Fig. 9.3.3 were used as a basis for planning test regimes, which may be of a particular interest for boundary layer control investigations. It was found that obtained effects were strongly influenced by the correlation between the surface curvature and the distance between the heated strips. So for R200 model, most interesting results were obtained for 2.5 mm spacing of heaters, while for R800 model the same was true for 5 mm spanwise spacing.

Detailed results obtained on the both models under various test conditions are described below.

1. Temperature of convex sections increasing from 20 to 60°C resulted in an almost proportional change of increments of drag and pitch moment coefficients. At the same time, lift coefficients remain constant (Fig. 9.3.4). Temperature variation within ΔT = 20°C -- 40°C on concave surface had practically no effect on the increments of aerodynamic characteristics (Fig. 9.3.5).

It should be noted that the increments of drag coefficients on convex and concave surfaces had opposite sings. Heating of the convex surface increased drag coefficients, while the concave surface heating decreased them. This difference could be probably explained with different downstream pressure gradients along the surfaces.

At negative angles-of-attack for R800 model in normal position, heating of both convex and concave sections became ineffective.

2. As the free-stream velocity (Reynolds number) grows, the heating was found to become less efficient. It was especially well seen for the pitch moment coefficient (figure 9.3.6). At the same time, the

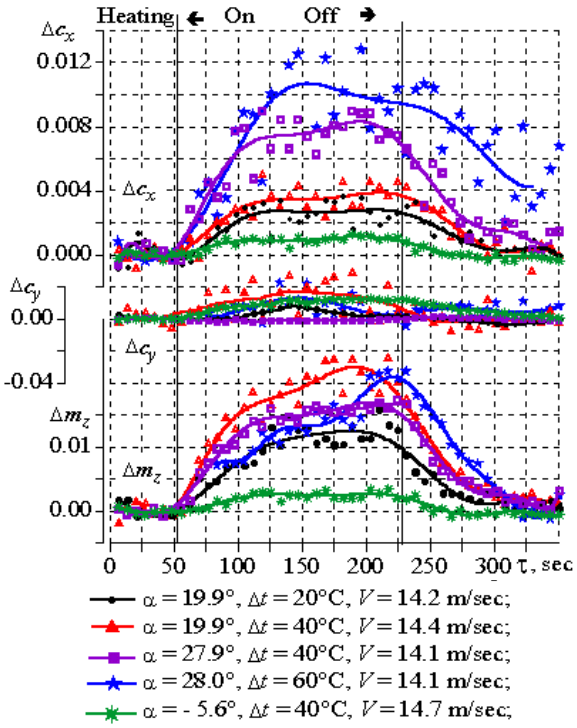

Fig. 9.3.4 (all the sections of the convex surface heated)

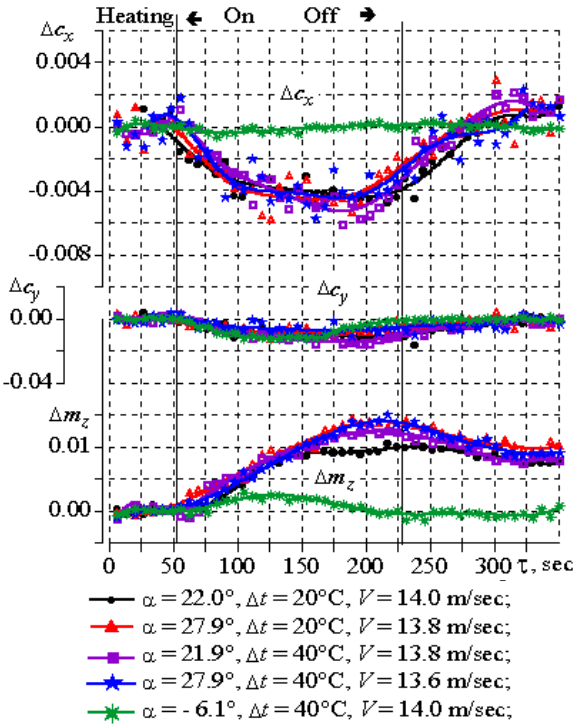

Fig. 9.3.5 (all the sections of the cocave surface heated)

Lift, drag and pitch moment coefficient increments of the **R800** model
depending on the controlling temperature gradient ΔT at its spanwise scaling λ_z=5 mm

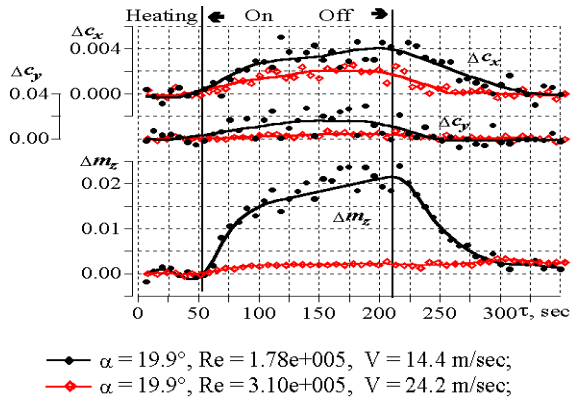

Figs. 9.3.6. Lift, drag and pitch moment coefficient increments of the **R800** model depending on Reynolds number, λ_z=5 mm, ΔT=40°, the whole concave surface is heated

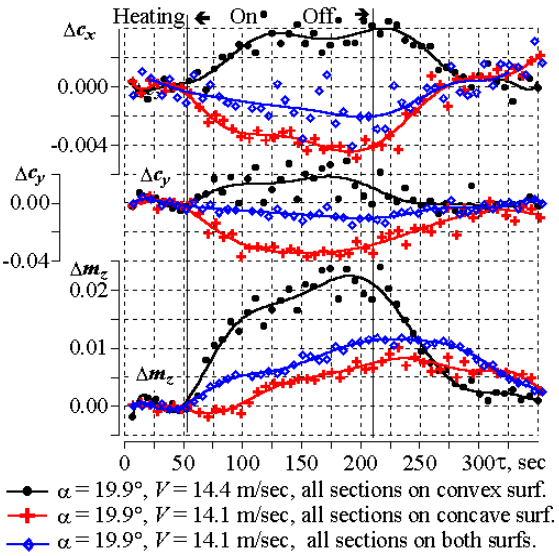

Fig. 9.3.7. Lift, drag and pitch moment coefficient increments of the **R800** model depending on the ditribution of heaters over the model, λ_z=5 mm, ΔT=40°

data scattering increased considerably while the free-stream velocity decreased. It can be explained with an unsteady behavior of vortex structures in streamwise direction and substantially growing relative errors at low loadings.

3. Figure 9.3.7 shows variation of aerodynamic coefficients of R800 model for different heat control schemes (distribution of heated sections over the model). The "nose-up" increment of pitch moment is common for all tested configurations. Lift and drag coefficient increments are positive in case of heaters are switched on over a convex part of the model and they are negative for concave heaters on. When heaters are switched on over both convex and concave surfaces, the effect from concave heaters prevails over that of convex ones.

4. Influence of distribution of heated sections over R200 model is shown in figures 9.3.8 and 9.3.9. It displays results generally similar to those for R800 model. In addition, peak value of a drag coefficient is observed with an only nose heated section over a convex surface (#1 or S1); however this drag drops under the activation of the middle and tail sections. Heating of the convex sections had practically no effect on the lift coefficient. At the same time, there was observed a growth of the pitch moment coefficient $\mathbf{m_z}$. It means that circulation redistribution in a streamwise direction occurs with a positive increment around the nose section of the model and with the negative one around the tail. Here, the maximum $\mathbf{m_z}$ increment is again observed when only the nose section is heated, while the lowest $\mathbf{\Delta m_z}$ was obtained with heated sections #1 and #2; all three sections heated gave an intermediate result. To explain these results, additional experiments are needed which should include pressure distribution measurements.

Thermal control applied to the concave surface affected the drag in an opposite way. The maximum absolute increment (of a negative sign) was obtained with all sections "on" and it decreased with a decreasing number of heated sections. Lift coefficients dropped almost similar to drag coefficients but this drop was relatively small. Pitch moment coefficient behavior also indicated the circulation redistribution but of a more complex nature. Similarly, pressure distribution measurements would also be necessary to get an insight into the physics of fluid motion and its correlation with integral aerodynamic characteristics.

5. R800 model in a reversed position (sharp trailing edge directed upstream) is of a special interest. This experimental arrangement is modeling the flow, which is not distorted by a thick rounded leading edge and thus matches better with the flow over constant curvature surfaces considered in computations. Fig. 9.3.3 shows a singularity for the lift coefficient curve for α = 9…10°, therefore these angles of attack were chosen for detailed investigations. At this α, the flow velocity vector is close to tangent both to concave and convex

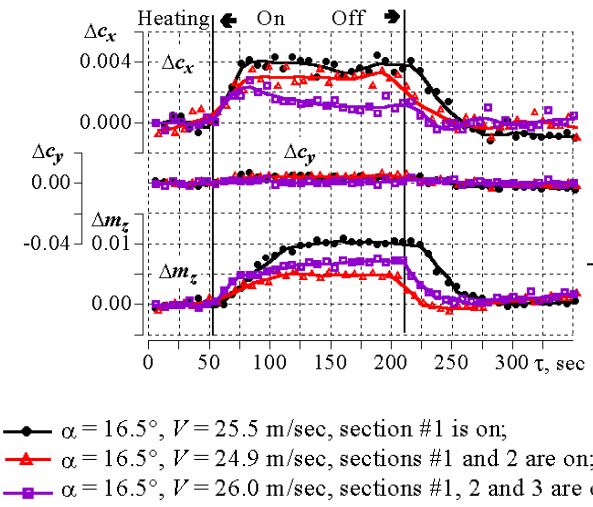

Fig.9.3.8. Lift, drag and pitch moment coefficient increments of the **R200** model depending on a number of heated sections over the convex surface, λ_z=2.5 mm, ΔT=40°

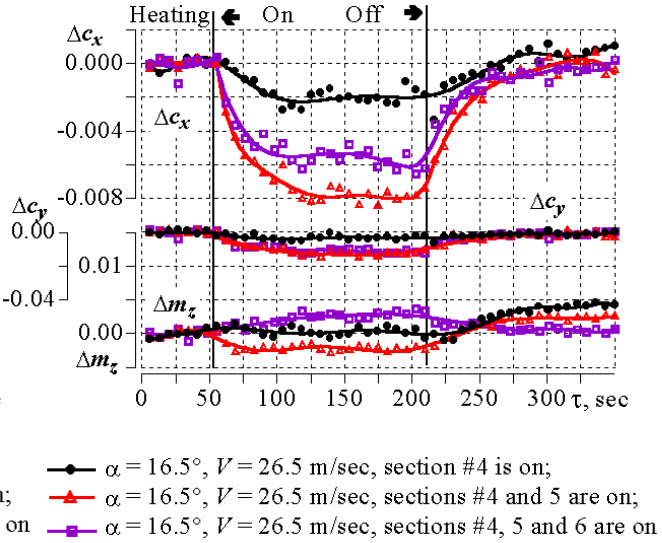

Fig. 9.3.9. Lift, drag and pitch moment coefficient increments of the **R200** model depending on a number of heated sections over the concave surface, λ_z=2.5 mm, ΔT=40°

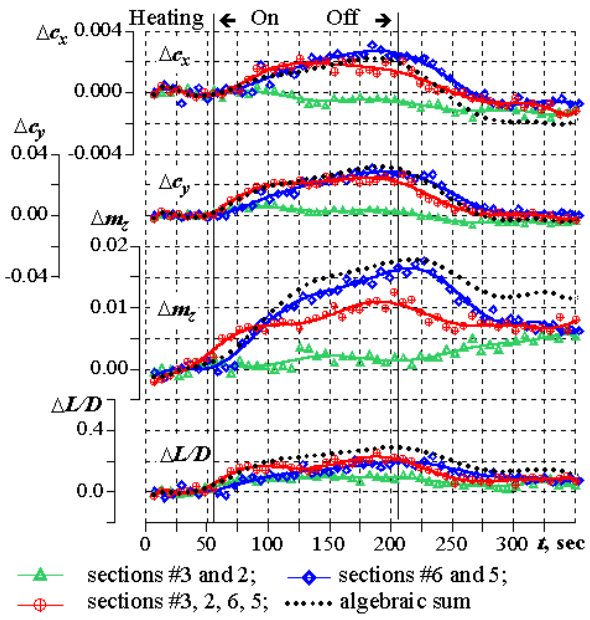

Fig. 9.3.10. Lift, drag, pitch moment and lift-to-drag ratio coefficient increments of the **R800** model in a reversed position: α=9º, U_0=15 m/, λ_z=2.5 mm, ΔT=40º

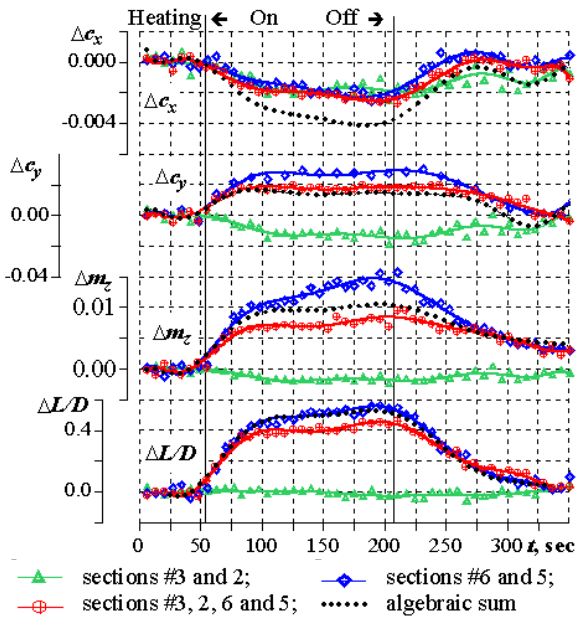

Fig. 9.3.11. Lift, drag, pitch moment and lift-to-drag ratio coefficient increments of the **R800** model in a reversed position: α=10º, U_0=15 m/, λ_z=2.5 mm, ΔT=40º

surfaces in their junction point (trailing edge). Figs. 9.3.10 and 9.3.11 show aerodynamic coefficients and lift-to-drag ratio varying in time at $\alpha = 9°$ and $\alpha = 10°$. It can be seen that drag coefficient increments over a concave surface (heaters #6 & 5) are of opposite signs, while lift and pitch moment coefficient increments are all positive. It means that pressure gradient on the initial section of the concave surface strongly affects the drag behavior. This is not the case of a convex surface heating. At $\alpha = 9°$, heating has practically no effect on the aerodynamic coefficients, while at $\alpha = 10°$ the small drop of all coefficients is observed. For this model position, the increments of pitch moment coefficient are again positive in cases of heaters activated on a concave surface as well as on the both of them, and are close to zero under only the convex surface heated

Taking into account that influence of the thermal control applied to convex and concave surfaces is substantially different and that the effect of the concave surface prevails, the algebraic sum of increments was calculated for separate heating of these surfaces. The result was compared with the directly measured combined effect of both surfaces heated simultaneously. Calculated and measured increments were found to be different, except for the lift coefficient at $\alpha = 10°$. It can be interpreted as follows: the change of the circulation (flow field) in a streamwise direction over the heated surface leads to corresponding redistribution of circulation over the cold surface in order to comply with Zhukovsky-Tchapligin postulate.

Fig. 9.3.12 accumulates measurement results to compare them for different flow parameters of the R800 model tested. It confirms the observations and made conclusions in case of the thermal flow control when all S1-S6 sections were heated. Although this combination of heated sections is far from being optimal, it explicitly shows a possibility to increase aerodynamic quality of the profile for near-critical angles of attack using generated streamwise vortices.

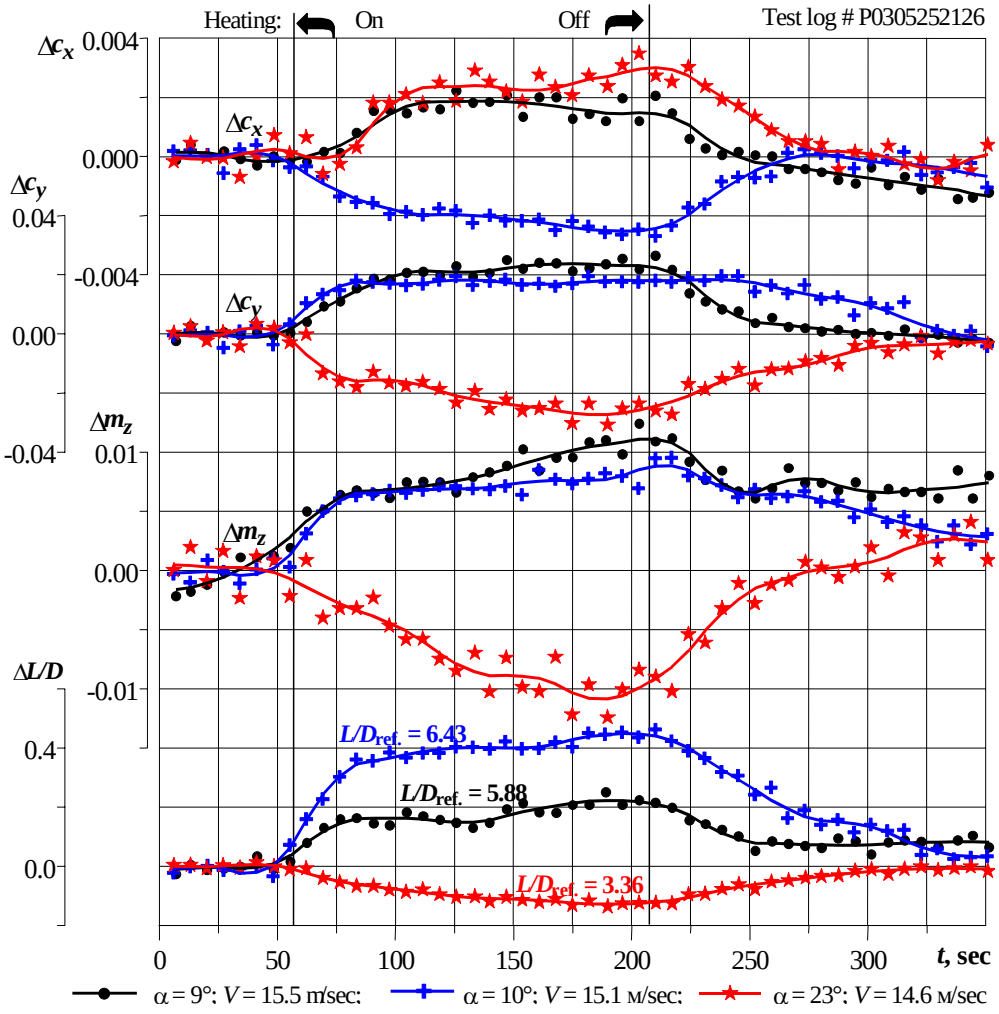

Fig. 9.3.12. Increments of drag Δc_x, lift Δc_y, pitch momentum Δm_z coefficients and lift-to-drag ratio $\Delta L/D$ versus time for near-critical angles of attack $\alpha = 9^\circ$ and 10° and for a supercritical regime $\alpha = 23^\circ$ under conditions of thermal control (both sides of a model were heated with $\lambda_z = 5$ mm, $\Delta T \approx 40^\circ$)

9.4. Conclusions from experiments

Design and fabrication technology for airfoil test models were developed to study thermal flow control. Using a complex of experimental methods, aerodynamic characteristics of the models were investigated under conditions of streamwise vortices generated in a boundary layer. The obtained data proved the method feasibility, efficiency and prospects for the turbulent transport control with minimal external energy supply.

Estimation of thermal control efficiency in boundary layers over concave and convex surfaces of airfoil models was made from the analysis of measured lift and drag coefficients. These experiments showed the advantage of an airfoil model R800 versus the R200 due to its better aerodynamics (later separations and thus longer controlled regions for a certain range of angles of attack). However analysis of experimental results obtained on the both models in conjunction with a corresponding computational part brought to important conclusions.

It was found that the drag coefficient drop can be accompanied with the increased lift coefficient around critical angles of attack ($\alpha = 10°$). It implies the lift-to-drag ratio improvement by a maximum value of 0.55, which is an encouraging result by itself. In addition, it was obtained due to the very small relative energy outlay. The calculations show that under experimental conditions, required 2% of electrical power for the thermal flow control (relative to that required for a flight) improve the profile efficiency (L/D) by more than 8%. Here the required (aerodynamic) power was calculated as $P_a = c_x S\rho V^3/2$ and the required power for heating was $P_e = \sum U_j I_j$.

Prospects

The developed strategy of the flow control using thermally generated streamwise vortices was proven to be effective. The thermal control method is feasible but under certain flow conditions it should be supplemented or enhanced. It can be done due to its combination with other techniques, for instance mechanical surface heterogeneity in a form of specially shaped holes distributed over a surface. The developed turbulence model was tested and shown itself applicable for this kind of investigations.

Future investigations of a particular practical interest should deal with the flow control using streamwise vortices generated in the cascades of profiles to model flows in axial compressors and turbines of aviation and various industrial applications. Purposely varying scales of the vortical motion using the developed method of thermal flow control, it is expected to improve aerodynamic characteristics of the blade cascades. Parallel numerical and experimental parts of the research demonstrate efficiency of such a combined approach.